Division of Biopharmaceutics and Pharmacokinetics
Faculty of Pharmacy
University of Helsinki
Finland

Non-labelled surface sensitive techniques as platforms for pharmaceutical nanotechnology research

Huamin Liang

ACADEMIC DISSERTATION

To be presented, with the permission of the Faculty of Pharmacy of the University of Helsinki, for public examination in Lecture Hall 4 (Sali 4) at Viikki Info Center Korona, Viikinkaari 11, on 14th September 2013, at 12:00 noon.

Helsinki 2013

Supervisors: Professor Marjo Yliperttula
Division of Biopharmaceutics and Pharmacokinetics
Faculty of Pharmacy
University of Helsinki
Finland

Dr. Tapani Viitala
Division of Biopharmaceutics and Pharmacokinetics
Faculty of Pharmacy
University of Helsinki
Finland

Reviewers: Lecturer Elina Vuorimaa
Department of Chemistry and Bioengineering
Tampere University of Technology
Finland

Dr. Lasse Murtomäki
Department of Chemistry
Aalto University
Finland

Opponent: Professor Jouko Peltonen
Laboratory of Physical Chemistry
Department of Physical Chemistry
Åbo Akademi University
Finland

ISBN 978-952-10-9174-2 (paperback)
ISBN 978-952-10-9175-9 (PDF, http://ethesis.helsinki.fi/)

Helsinki University Print
Helsinki, Finland 2013

ABSTRACT

Insufficient delivery of drugs to the target sites like tumors and cells has been a barrier for achieving satisfying therapeutic effects in many diseases. Distribution and exposure of drugs to normal and healthy tissues may enhance the possibility of side effects and toxicity *in vivo*. Nanoparticle (NP) drug delivery systems have been developed to enable targeting of drugs to target sites and at the same time also reduce or even eliminate the distribution and exposure of drugs to non-targeted sites (normal and healthy tissues). The interactions of ligand attached NPs with specific receptors on the cell surface enable intracellular delivery of drugs. Knowledge of the molecular mechanisms (kinetics and affinity) of specific NP surface interactions is vital for designing and optimizing NPs based targeted drug delivery systems. Biophysical non-labelled surface sensitive detection techniques allow the characterization of the specific NP-cell interactions *in vitro* at the molecular levels.

In this work, surface sensitive non-labelled surface plasmon resonance (SPR) and quartz crystal microbalance (QCM) biosensors were optimized, utilized and further developed as platforms for *in vitro* characterization and evaluation of the targeting of NP drug delivery systems. A multi-parameter SPR (MP-SPR) prototype was modified, improved and optimized for characterizing molecular surface interactions and phospholipid based thin film properties. The methodologies to extract simultaneously the thickness and the optical properties of thin films were developed by using the multi-wavelength SPR technique. The methodologies were extended to cover the film thickness from few nanometers to micrometers by combining the SPR wavelength and the waveguide mode analysis. These methods were successfully utilized for analyzing LB mono- and multilayers and further for the polyelectrolyte multilayer films.

In order to enable the combined use of SPR and QCM techniques for drug and NP interaction studies, these two devices were synchronized to achieve consistent hydrodynamic conditions in the flow channels by computational fluid dynamics (CFD) modeling. The flow channels and the device synchronization were verified by the streptavidin-biotin and liposome-surface interactions. The synchronized SPR and QCM devices were further utilized for the examination of the targeting properties via the streptavidin-biotin liposome interactions under different shear flows. The effect of the flow rate and shear stress on the targeted liposome with the target surface was investigated. The results from SPR and QCM measurements were compared, showing that the binding of the targeted liposome was flow rate and shear stress regulated. According to the SPR measurements, high flow rates improved the binding of liposomes to the target surface. However, the results obtained from the QCM measurements were somehow different. They gave additional information about the liposome binding behavior, indicating deformation or rupture of the bound liposomes at high flow rates and shear stresses.

In conclusion, SPR and QCM, the two label free surface sensitive techniques, are excellent platforms for pharmaceutical nanotechnology research. These allow for both the nanoparticle interaction studies and the characterization of nanoscale thin films. Especially, the combined use of the synchronized SPR and QCM techniques forms a

powerful platform for the qualitative and quantitative characterization of NP-surface interactions for obtaining in-depth understanding of the targeting behavior of NP drug delivery systems. The results obtained provides the basis for developing new complementary *in vitro* platforms to traditional cell based *in vitro* assays for optimizing and screening of NP based targeted drug delivery systems.

ACKNOWLEDGEMENTS

This work was carried out at the Division of Biopharmaceutics and Pharmacokinetics, Faculty of Pharmacy, University of Helsinki (10. 2007–09. 2009 and 06. 2010–08. 2013).

In 2007 when I landed in Finland, such a charming Nordic country, for the first time, I knew Prof. Marjo Yliperttula and Dr. Tapani Viitala, my dear supervisors. Prof. Marjo Yliperttula is the very one who always could give me encouragement and confidence whenever I was depressed, who has been holding me with a broad heart during these years and who has made great contribution to this study. The most sincere gratitude and esteem to her. I am also deeply grateful to my second supervisor Dr. Tapani Viitala for generous contribution to this work and positive scientific attitude. His profound knowledge and intelligent mind inspire and benefit me to a large extent.

Lecturer Elina Vuorimaa and Dr. Lasse Murtomäki are sincerely thanked for their wonderful works on my thesis reviewing and the valuable comments. I am honored that Professor Jouko Peltonen has accepted the invitation to be the opponent for the public defense of my Ph.D. thesis.

I wish to express my deepest thanks to all my co-authors, Dr. Alex Bunker, M.Sc. Niko Granqvist, Mayur Gupta, Terhi Laurila, M.Sc. Julia Lehtinen, M.Sc. Heini Miranto, Dr. Janusz Sadowski, M.Sc. Jussi Tuppurainen, Prof. Bochu Wang and Dr. Thomas Zwinger for their contribution. I also thank Dr. Alma Kartal-Hodzic and Dr. Unni Tengvall for their good discussion and valuable information about the procedures related to the thesis printing and the public examination. I would like to express my deepest thanks to all my current and former colleagues at the Division of Biopharmaceutics and Pharmacokinetics and at the Center for Drug Research (especially in DDN group) for comfortable working atmosphere and for their help with discussion or lab work. I would like to thank all my Chinese friends in Finland for their friendship and help during my stay in Finland. Especially, Mr. Gang Zong who was the previous head of the educational section of Chinese Embassy in Finland, helped me so much with my life in Finland. Dr. Li Li, Dr. Anchang Liu, M.Sc. Peng Liu, Dr. Qian Long, Prof. Shubin Si, Prof. Jiewen Wang and Dr. Yaowei Yu etc. are acknowledged for caring and help during their stay in Finland.

I warmly wish to thank my relatives, especially my mother Guimei Dong, my father Xiaoshui Liang, my sister Huaning Liang and my brother Jimin Liang for their selfless love and support these years. Finally, my deepest gratitude is reserved for my wife for her coming to Finland to accompany me by resolutely quitting her job, for her great tolerance, for her generous love, support and encouragement. My warm gratitude is also given my little son Chenxu Liang for his love and joy to our lives. Without their love and support, everything is not possible.

The Academy of Finland, Finnish Funding Agency for Technology and Innovation (TEKES) and China Scholarship Council (CSC) are acknowledged for the financial support for this work. The Graduate School in Pharmaceutical Research is thanked for the travel grant. The KSV and the BioNavis companies are also thanked for support with instruments.

Helsinki, August 2013

Huamin Liang

CONTENTS

LIST OF ORIGINAL PUBLICATIONS

This thesis is based on the following publications:

I Huamin Liang, Heini Miranto, Niko Granqvist, Janusz W. Sadowski, Tapani Viitala, Bochu Wang, Marjo Yliperttula: Surface plasmon resonance instrument as a refractometer for liquids and ultrathin films. Sensors and Actuators B: Chemical 149: 212-220, 2010.

II Niko Granqvist ‡, Huamin Liang ‡, Terhi Laurila, Janusz Sadowski, Marjo Yliperttula, Tapani Viitala: Characterizing ultrathin and thick organic layers by surface plasmon resonance three-wavelength and waveguide mode analysis. Langmuir 29: 8561-8571, 2013.
(‡ Contributed equally to this work)

III Tapani Viitala, Huamin Liang, Mayur Gupta, Thomas Zwinger, Marjo Yliperttula, Alex Bunker: Fluid dynamics modeling for synchronizing surface plasmon resonance and quartz crystal microbalance as tools for biomolecular and targeted drug delivery studies. Journal of Colloid and Interface Science 378: 251-259, 2012.

IV Huamin Liang, Jussi-Pekka Tuppurainen, Julia Lehtinen, Tapani Viitala, and Marjo Yliperttula: Non-labelled monitoring of targeted liposome interactions with a model receptor surface: effect of flow rate and water content. European Journal of Pharmaceutical Sciences, 2013 (In press).

ABBREVIATIONS

AFM	atomic force microscopy
AS	angular scanning mode
BAM	Brewster angle microscopy
BAW	bulk acoustic wave
BLA	biologics license application
BSA	bovine serum albumin
Caco-2	carcinoma colon 2 cell line
CdSA	cadmium stearate
CFD	computational fluid dynamic
CHOL	cholesterol
DSC	differential scanning calorimetry
DSPE-PEG_{2000}	1,2-distearoyl-sn-glycero-3-phosphoethanolamine-N-[methoxy(polyethylene glycol)-2000] (ammonium salt)
DSPE-PEG_{2000}-Biotin	1,2-distearoyl-sn-glycero-3-phosphoethanolamine-N-[biotinyl(polyethylene glycol)-2000] (ammonium salt)
ECM	extracellular matrix
EG	ethylene glycol
EG_3	HS-$(CH_2)_{11}$-$(OCH_2OCH_2)_3$-OH
EG_3-Biotin	HS-$(CH_2)_{11}$-$(OCH_2OCH_2)_3$-biotin
ELISA	enzyme-linked immunosorbent assays
EPR	enhanced permeability and retention
EtOH	ethanol
FA	fixed angle mode
FDA	U.S. Food and Drug Administration
G	gas state
GPCR	G-protein-coupled receptors
HEPES	4-(2-Hydroxyethyl)piperazine-1-ethanesulfonic acid
HF	high-frequency
HSPC	hydrogenated L- a-phosphatidylcholine
HTS	high throughput screening
ITC	isothermal titration calorimetry
K	apparent equilibrium constant
k_a	association rate constant
k_d	dissociation rate constant
K_D	dissociation constant
LB	Langmuir-Blodgett
LC	liquid condensed or crystal state
LE	liquid expanded state
LOD	limit of detection
LOQ	limit of quantitation

MDCK	madin-darby canine kidney cell line
MP-SPR	multi-parameter surface plasmon resonance
NP	nanoparticle
OEG	oligo (ethylene glycol)
PAH	poly(allylamine hydrochloride)
PBS	phosphate buffered saline
PC	phosphatidycholines
PDMS	poly-dimethylsiloxane
PE	phosphatidylethanolamines
PEG	poly (ethylene glycol)
PEI	poly(ethylene imine)
PEM	polyelectrolyte multilayer
PLGA	poly(lactic-co-glycolic acid) copolymer
PLL	poly(L-lysine)
PLLA	poly-L Lactic Acid
PM-IRRAS	polarization-modulated infrared reflection absorption spectroscopy
PSS	poly(styrene sulfonate) sodium salt
QCM	quartz crystal microbalance
QCM-D	quartz crystal microbalance with dissipation monitoring
R	correlation coefficient
RES	reticuloendothelial system
RI	refractive index
RSD	relative standard deviation
S	solid state
SA	stearic acid
SAM	self-assembled monolayer
SAW	surface acoustic wave
SD	standard deviation
SE	spectroscopic ellipsometry
SERS	surface-enhanced Raman spectroscopy
SLB	supported lipid bilayer
SPR	surface plasmon resonance
SPW	surface plasmon wave
SR	shear rate
SS	shear stress
sSLB	solid supported lipid bilayer
SVL	supported vesicle layer
T_{eff}	effective thickness
TIR	total internal reflection
TLB	tethered lipid bilayer
TSM	thickness shear mode

Uac	uranyl acetate

1 INTRODUCTION

With the progress of modern drug discovery and development, more new drugs have been approved by drug regulatory authorities and brought to the market, which is beneficial to disease treatment and human health. However, achieving the approval and marketing of new drugs have experienced increasing difficulties. The number of new molecular entities (NME) approved per year has been declining, whereas the research and development expenditure has been increasing. (Allison, 2012; Kling, 2011; Mullard, 2013) A review published by Scannell *et al* shows that the number of new drugs approved by U.S. food and drug administration (FDA) per billion US dollars has halved about every 9 years since 1950 (from ~50 in 1950 to less than 1 in 2010) (Scannell et al., 2012). On the other hand, the number of biologics license applications (BLAs) approved has been nearly constant (4.7±1.8/year) since 1996, especially 2009-2012 (~6/year) (Mullard, 2013). One of the major challenges in modern drug discovery and development is to efficiently deliver drugs to target sites (Paasonen, 2010). Especially, for emerging biotechnological drugs such as DNA, siRNA, peptides, antibodies and proteins, The efficient delivery of them to the target sites is extremely vital to achieve therapeutic effect because these drugs can not be administered like small molecular drugs due to their large molecular weight, susceptibility to enzymatic degradation and intracellular delivery required in some cases (e.g. siRNA, transcription factors, and DNA) (Yliperttula & Urtti, 2009). In addition, many other issues such as delivery of drugs into difficult sites (e.g. brain, tumors, retina, and intracellular targets), prolongation of drug action (controlled release) and improved drug absorption are also challenging.

Pharmaceutical nanotechnology offers new opportunities to solve these issues. Many of these challenges are foreseen to be overcome with the help of nanoparticle based drug delivery systems. In particular, intracellular delivery of biotechnological drugs (e.g. DNA and siRNA) and targeted delivery of cancer drugs are enabled through nanoparticles (NPs). Nanoparticle-based targeted drug delivery may be achieved by passive or active targeting. Passive targeting is based on the extravasation of nanoparticles from the systemic circulation into the target tissues that is intensified by the enhanced permeability and retention (EPR) effect in tumors. Active targeting relies on the specific ligand-receptor interaction to achieve targeting by receptor-mediated endocytosis. Intracellular delivery of drugs can be achieved by ligand-attached nanoparticles, which are internalized by the receptor-mediated endocytosis. Attached ligands can improve cellular internalization of nanoparticle-loaded drugs by binding to specific target cell receptors. Active targeting is therefore expected to improve the therapeutic availability of drugs to target cells within the pathological sites and to minimize undesired side effects to non-target cells within the pathological tissues. (Metselaar et al., 2002)

A number of nanoparticle drug delivery systems based on liposomes and polymer-drug conjugates have already been approved for clinical use (Farokhzad & Langer, 2009). These therapeutic products improve the efficacy, safety and dosing regimen of clinically approved drugs. For example, liposome based cancer treatment drugs AmBisome®, DaunoXome®, Doxil® and Myocet® have been approved by FDA and they are already on the market (FDA, 2013). However, all these liposome based cancer drugs are based on passive targeting, whereas site-specific active targeted nanoparticles

(immunonanoparticles) are still in the stage of development. Possible issues in immunonanoparticles include penetration into solid tumors, specific uptake to tumor cells, and drug release at the target site etc. The accessibility and binding of targeted liposomes to target cell surfaces, which results in liposome uptake via receptor-mediated endocytosis, are vital for the targeting efficiency and the therapeutic efficacy of actively targeted NPs. The interaction of NPs with the cell surface, an interfacial event, thus becomes a prerequisite for the therapeutic effect of the drug. The NP uptake rate and cell uptake mechanism are dependent on both the cell-type and the physicochemical properties of nanoparticles, such as size, shape, surface ligand density and arrangement, charge, and other surface properties. (Iversen et al., 2011; Verma & Stellacci, 2010) Therefore, an in-depth understanding of the interfacial interactions between NPs and cells is of utmost importance for designing and optimizing NP based formulations.

In vitro cell cultures and *in vivo* animal tests are indispensable methods in cell based targeting studies. The complex environment in cell cultures and animal tests make quantitative understanding of the targeting process of NPs challenging (Doane & Burda, 2012). Furthermore, cell cultures and animal tests are not powerful for quantitatively characterizing a biological process at molecular level. A cell culture in plates at a static state cannot reflect the effect of blood flow *in vivo*. Therefore, biophysical detection techniques are very useful tools for characterizing nanoparticle-cell interactions. Non-labelled surface sensitive techniques, such as surface plasmon resonance (SPR) and quartz crystal microbalance (QCM), allow for studying the interfacial interaction event at the molecular level under simplified environments and well-controlled physicochemical conditions (e.g. such as pH, temperature and flow rate/shear stress). The affinity and kinetics (i.e. how fast, how much, how strong and how specific) behind the specific nanoparticle-cell interaction can be investigated by using a simplified surface model membrane.

In this study, two non-labelled surface sensitive techniques, SPR and QCM, were utilized as platforms to characterize the interaction between NPs and a model receptor membrane under well-controlled shear flow. SPR and QCM were hydrodynamically synchronized in order to achieve consistent conditions for the combined use of SPR and QCM which allows for extraction of in-depth information on the NP interaction. With this method, the interaction between model targeting NPs (i.e. biotin-liposomes) with a model receptor membrane (i.e. self-assembled monolayer (SAM) of PEG-thiol with surface immobilized streptavidin) was characterized. The response of the NP interaction to the flow rate and shear stress was also investigated. In addition, methodologies allowing for simultaneous determination of thickness and refractive index of both thin and relatively thick layers by SPR measurements were constructed. These characterizing methodologies are important tools when optimizing the preparation processes of polymer cushioned lipid bilayers membranes and growing of living cell monolayers as platforms for nanoparticle interaction studies in the future.

2 REVIEW OF THE LITERATURE

2.1 Non-labelled detection techniques

Biomolecular interactions of ligand/drug-receptor, antigen-antibody, virus-cell and protein-DNA binding are biologically and physiologically important, and these are also usually related to physiological, pathological and pharmacological processes (Ozkumur et al., 2008). The maxim: "A drug will not work unless it is bound" by Paul Ehrlich at the beginning of the twentieth century, highlights the importance of the interaction of drug-receptor pairs (Ehrlich, 1913). Thus, a drug is efficacious only on the condition that it is bound to its physiological target(s) (Copeland et al., 2006). The widely established and extensively used solid-phase enzyme-linked immunosorbent assays (ELISA) and western blotting enable the quantitative detection of biological and medical interactions, which allows us to understand the physiological, pathological and pharmacological drug action processes (Blake & Gould, 1984; Ozkumur, et al., 2008). However, these immunoassays are typically based on label assay techniques in which secondary probes are employed for detecting specific binding of the analytes (antigens, Ags). With the help of fluorescent or enzyme-linked reagents, the secondary probes form colored or fluorescent products, which can be detected with a spectrophotometer or other instruments. Small molecules such as drugs have to be coupled to a macromolecular carrier (usually a protein) to become immunogenic. (Gosling, 2000; Van Emon, 2007)

Label-based techniques involve labelling of molecules (e.g. fluorescent dyes, radioisotopes, epitope tags, etc.) which can structurally and functionally interfere with an assay by blocking active sites on the tagged molecule, modifying the molecular conformation or altering its surface (e.g. cellular surface) characteristics. In some cases, the labels can interfere with the molecular interaction by occluding a binding site, which leads to false negatives. The laborious and lengthy labelling procedures including numerous washing, blocking and exposure conditions, increases the assay complexity. (Cooper, 2009; Ozkumur, et al., 2008; Ray et al., 2010; Vollmer & Arnold, 2008; Yu et al., 2006)

In contrast, non-labelled techniques simplify the assays by avoiding the need of secondary reactants, and allow detecting, based on the properties of the analyte itself, the biomolecules in their natural (unlabeled or unmodified) forms in real-time (Fan et al., 2008). Therefore, non-labelled detection is preferred for the biomolecular interaction assays whenever possible.

2.1.1 Rationale for non-labelled techniques

Compared to the many drawbacks of label-based assays, non-labelled (label-free) detection techniques are expected to reduce the assay complexity and cost, while simultaneously providing real-time quantitative information (Cooper, 2009). Non-labelled techniques allow a direct measurement of the molecular interactions and the quantification

of binding affinity and kinetics based on the analyte's own physical properties such as mass, volume, refractive index, dielectric permittivity, viscoelasticity, conductivity etc. (Cunningham et al., 2004). The interaction event is reflected by the changes in these physical properties in the close vicinity of the surface resulting from the binding of an analyte on the surface. A transducer is required for non-labelled detection to transform the changes in the physical properties into a measurable signal (e.g. current or voltage), which can often be recorded in real-time. An optical, a mechanical or an electrical transducer can be employed for non-labelled detection (Hunt & Armani, 2010). For example, surface plasmon resonance (SPR) is an optical label-free biosensor, which is sensitive to the change in refractive index (RI) on the sensor surface. (Homola et al., 1999)

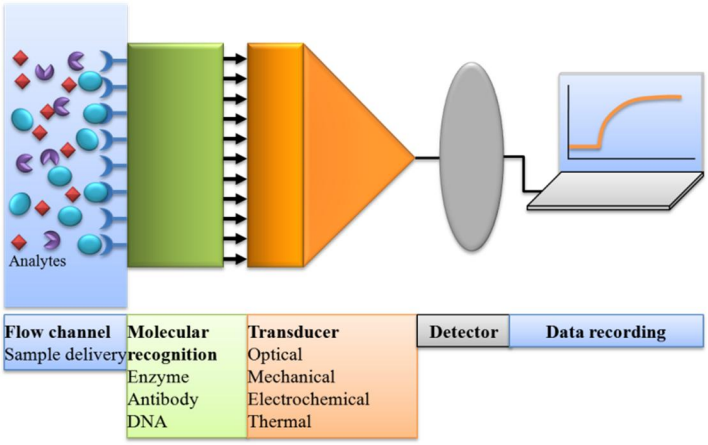

Figure 1. *Schematic illustration of the general operating principle of a non-labelled (bio)sensing system.*

A non-labelled detection system typically consists of a molecular recognition element and a transducer, combined with a detector and a liquid handling system (Figure 1). The molecular recognition element is a surface layer where chemical or biological interaction events take place. It implies that the integration of recognition (e.g. a receptor) with the solid surface of the transducer is extremely important in order to obtain a specific interaction. This can be achieved by the modification and the functionalization of the sensor surfaces through physical adsorption, self-assembled monolayer and covalent coupling techniques. Such sensor surfaces with an integrated surface-sensitive and specific receptor enables to obtain a comprehensive understanding of biological interfacial processes (i.e. how strong, how fast and how specific the interaction is). In some cases, a linker layer is deposited in the recognition element between the recognition molecule and the sensor surface in order to create a biocompatible or a biomimetic environment, e.g. solid supported lipid bilayers with a hydrophilic polymer cushion (cell membrane-mimicking surface). Antibodies, proteins, enzymes, nucleic acids, living cells, microorganisms and even tissues may be used as a recognition element for the non-labelled detection systems (Mohanty & Kougianos, 2006; Vo-Dinh & Cullum, 2000).

2.1.2 Non-labelled biosensing systems

As mentioned above, different physical properties (e.g. mass, refractive index and viscoelasticity) may be utilized as indicators when sensing the presence of an analyte. Most of the non-labelled biosensing systems can be categorized in one of the four main classes based on the employed transduction method: 1) Optical, 2) Mechanical (or mass), 3) Electrochemical and 4) Calorimetric (or thermometric). Each of the classes consists of different subclasses (Mohanty & Kougianos, 2006; Monošík et al., 2012; Vo-Dinh & Cullum, 2000).

The detection for optical biosensors is achieved by exploiting the interaction of the electromagnetic field with its environment. Thus various spectroscopic methods like surface plasmon resonance (SPR), general evanescent field (e.g. optical waveguide), absorption, Raman, surface-enhanced Raman spectroscopy (SERS), interference, refraction and dispersion spectrometry can be utilized to implement an optical transducer. Thus, changes in the amplitude, energy, polarization, or phase induced by molecular interactions can be recorded in real-time. SPR is one of the most widely spread optical label-free techniques and is the most widely developed optical biosensor. Mechanical label-free techniques are based on detecting the change of the mass on the sensor substrate surfaces. (Fang, 2006; Hunt & Armani, 2010; Vo-Dinh & Cullum, 2000) Quartz crystal microbalance (QCM) is a typical mechanical biosensor based on the piezoelectric phenomenon (O'sullivan & Guilbault, 1999). Another frequently used mechanical technique is a microcantilever, where the bending and resonance frequency shifts induced by the adsorption of an analyte is measured (Hansen & Thundat, 2005).

In (bio-)electrochemistry the reactions between a receptor and a ligand often produce or consume ions or electrons. The change in the electrical properties generates a measurable signal in the current (amperometry), potential (potentiometry), charge accumulation (coulometry), or conductive properties of a medium (conductometry/impedancemetry) between the electrodes. (Grieshaber et al., 2008; Thevenot et al., 2001). Calorimetric biosensors are applicable in cases where the reaction enthalpy (exothermal or endothermic) is involved. Calorimetric biosensors are constructed by combining immobilized biomolecules (e.g. enzyme) with temperature sensors. The reactions are monitored by measuring the change in the molar enthalpy, which is proportional to the number of molecules involved in the reaction. (Bohunicky & Mousa, 2011; Darsanaki et al., 2013; Monošík, et al., 2012) Examples of different non-labelled biosensing systems affiliated to the four classes are summarized in Table 1. These non-labelled techniques are not described in more detail here, except for SPR and QCM which have been used as a platform for the studies in this thesis.

Table 1. *Selected examples of non-labelled biosensing systems* [a, b]

Types of sensor	Technology	Instrument	Provider/Website	Formats
Optical	Surface plasmon resonance (SPR)	T200, Biacore 4000	Biocore: www.biacore.com	96- and 384-well microplates
		SPR Navi™ 200, SPR Navi™ 210, SPR Navi™ 220A	BioNavis: www.bionavis.fi	Chip-based flow cells, Multi-parametric SPR (MP-SPR)
	Surface plasmon resonance (SPR) imaging	PlasmonImager ™	Graffinity Pharmaceuticals;	Microarrays, up to 9126 spots
		SPRimager®II	GWC Technologies: www.gwctechnologies.com	Flexible array formats (>24)
	Waveguide-resonant waveguide grating	Epic™	Corning: www.corning.com	Microplate-based (348, 1536)
		EnSpire®	PerkinElmer: www.perkinelmer.com	Microplate-based (96, 348)
	Waveguide-guided mode resonant filter	SRU BIND	SRU Biosystems: www.srubiosystems.com	Microplate-based (16, 96, 348, 1536 well)
	Resonant mirror	Iasys	Thermo: www.thermo.com	
		SC-25, SC-30, SC-40	ELECTRO-OPTICAL: www.eopc.com	
	Biolayer interferometry	Octet® RED	ForteBio: www.fortebio.com	96-well plate, fluidics-free
	Dual polarization interferometry	AnaLight	Farfield (Part of Biolin Scientific: www.biolinscientific.com)	
	Imaging ellipsometry	EP³-SE, EP³-SW	Accurion GmbH: www.accurion.de	
	Diffractive optics technology	DOT™	Axela: www.axelabiosensors.com	
Mechanical/Mass	Quartz crystal microbalance (QCM)	E4, D300	Q-sense: www.q-sense.com (Part of Biolin Scientific)	With dissipation monitoring
		QCM-Z500	KSV Instruments Ltd (Part of Biolin Scientific)	With impedance monitoring
	Microcantilevers	CSR-801, CSR-801G	Concentris GmbH: www.concentris.ch	Chip based flow cell, 8 per chip

Electrochemical	Impedance	CellKey® 384 system	MDS Sciex: www.mdssciex.com	Microplate-based (96, 348 well)
		ECIS™	Applied Biophysics: www.biophysics.com	Microplate-based (8, 16, 96 well)
		iCELLigence	Acea Biosciences: www.aceabio.com	Microplate-based (16, 96, 348 well)
Thermal	Differential scanning calorimetry (DSC),	Nano ITC, Nano DSC	TA Instruments: www.tainstruments.com	1 ml and 190 µl cell; 2 standard plates x 96 wells x 1000 µl / well
	Isothermal titration Calorimetry (ITC)	Auto-iTC200	MicroCal: www.microcalorimetry.com	200 µl sample cell, 4 - 96 well plates

[a] Not all types of non-labelled technologies or instruments of each type by all manufacturer are included in this table.

[b] References (Comley, 2008; Cooper & Whalen, 2005; Esterhouse & Petrinos, 2009; Fang, 2006; Halai & Cooper, 2012; Qavi et al., 2009; Scott & Peters, 2010; Shiau et al., 2008; Xi et al., 2008).

2.1.3 Surface plasmon resonance (SPR)

2.1.3.1 Theory and structure of SPR

Surface plasmon resonance (SPR), an optical non-labelled detection technique, is based on the total internal reflection (TIR), the evanescent electric field (E), and the surface plasmon waves. TIR takes place when a light beam above a critical incident angle is reflected at the interface from an optically denser medium to an optically thinner medium (both media should not absorb light). Under the TIR conditions, all the light is not reflected back from the interface, but a part of it called the evanescent wave (E) penetrates into the optically thinner medium and decays exponentially with increasing distance from the interface. The propagation vector of the evanescent wave (k_e) is equal to the component of incident light parallel to the interface (k_x), which is dependent on the incident angle (θ) and the propagation vector of the incident light $k = \sqrt{\varepsilon_1}\frac{\omega}{c}$.

(1) $$k_e = k_x = \sqrt{\varepsilon_1}\frac{\omega}{c}\sin\theta$$

where ε_1 is the dielectric constant of the prism, ω and c are the angular frequency and the velocity of the light in vacuum, respectively. If the optically denser medium is coated with a thin metal film (e.g. gold), then the p-polarized component of the evanescence field can penetrate into the metal film and interact with free electrons in the metal, thereby exciting an electromagnetic surface plasmon wave (SPW) at the metal-ambient medium (optical

thinner medium) interface. The light energy is transferred to the electrons of the metal by means of an evanescent wave, which induces a decrease in the intensity of the reflected light. This SPW is a surface electromagnetic wave, which propagates along the metal/dielectric interface. (Marks et al., 2007; Ricklin, 2005) The penetration depth of the SPW into the dielectric depends on the type of the coated metal and the wavelength of light (e.g. for wavelengths of 630 and 850 nm with coated gold, the penetration depths of the SPWs are 162 and 400 nm, respectively) (Homola, et al., 1999). The dispersion relation for the SPW on a metal surface is expressed by equation (2):

$$k_{spw} = \frac{\omega}{c}\sqrt{\frac{\varepsilon_m \varepsilon_2}{\varepsilon_m + \varepsilon_2}} \quad (2)$$

where k_{spw} is the SPW propagation constant, ε_2 and ε_m are the adjacent medium and the metal permittivity, respectively. The resonance will occur when k_e equals to the k_{spw}, i.e. when the incident light angle is increased to a value (resonant angle (θ)) at which minimum reflection occurs. The resonance condition for the Kretschmann configuration is expressed by equation (3):

$$\sqrt{\varepsilon_1}\frac{\omega}{c}\sin\theta = \frac{\omega}{c}\sqrt{\frac{\varepsilon_m \varepsilon_2}{\varepsilon_m + \varepsilon_2}} \quad (3)$$

Under the resonance condition, most of the incident light is absorbed in the metal. A sharp maximum absorption and minimum reflection will occur at the resonance angle (θ_{spr}). A valley will be observed in the SPR curve at θ_{spr}. According to equation (3), θ_{spr} is only dependent on the refractive index of the ambient medium in contact with the metal, n_2 ($= \sqrt{\varepsilon_2}$), when the optically denser medium (e.g. glass prism, dielectric constant ε_1), the metal (dielectric constant ε_m) and the wavelength of the incident light are kept unchanged. SPR is thereby sensitive to the changes in the refractive index of the ambient medium in contact with the metal surface.

Configuration of an SPR biosensor. An SPR biosensor consists of the molecular recognition element and the transducer. SPR can be excited by several optical configurations including a prism coupler, a waveguide coupler and a grating coupler. The "Kretschmann ATR configuration" based on attenuated total reflection (ATR) is the most commonly used setup in SPR biosensors (Figure 2a). In the Kretschmann ATR configuration, the bottom surface of the prism is coated by a metal film (gold). A p-polarized monochromatic light (e.g. 670 nm laser) is introduced to the metal surface with an incident angle (>critical angle). A surface plasmon wave is excited and resonance condition is achieved when the resonance angle (θ) is reached. During SPR scanning, the intensity of the reflected light is monitored as a function of the incident angle by a photodetector that is synchronously moving with the incident light source (laser). The wavelength of the laser can be changed if needed in order to achieve a simultaneous measurement with two different wavelengths. A glass slide with a coated gold film (~50 nm) is used as the sensor chip.

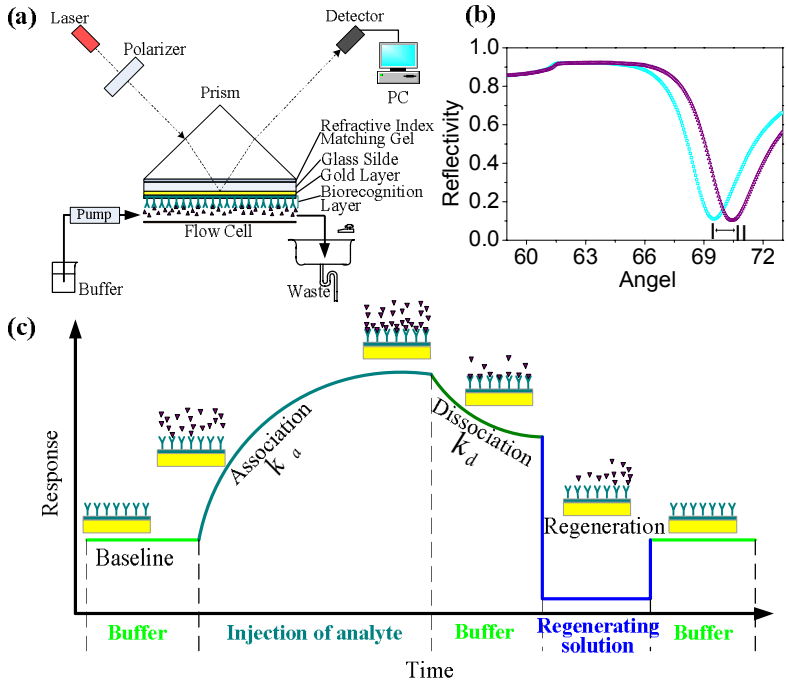

Figure 2. *(a) Schematic illustration of an SPR biosensor based on the Kretschmann ATR configuration (Liang et al., 2010), (b) the resonance angular changes (Liang, 2010), and (c) a typical real-time SPR sensogram for a ligand-receptor interaction (Liang, 2010).*

SPR angular reflectivity curve (SPR curve) and real-time sensogram. An SPR curve will be obtained when the reflectivity is monitored as a function of the incident angle (Figure 2b). The resonance angle is found through the SPR curve scanning. As a sample is allowed to flow over the sensor surface with the immobilized receptor, then a shift of the resonance angle to higher values takes place during the specific interaction and the binding of an analyte to the receptor (from I to II, Figure 2b). The resonance angle monitored as a function of time will form the real-time SPR sensogram (Figure 2c). The measuring mode based on monitoring the resonance angle as a function of time is called the angular scanning mode (AS). In addition to the AS mode, the ligand-receptor interaction can be monitored by the so called fixed angle mode (FA), which detects the intensity of the reflected light at a fixed incident angle within the linear range of the falling slope of an SPR curve (Figure 2b). The association, dissociation and regeneration phases constitute a typical SPR sensogram (Figure 2c). The formation of the ligand-receptor complex produces the association phase, while the ligand removal from the surface forms the dissociation phase. In the case of weak binding, then the sensor surface can be regenerated by using a regeneration solution. A ligand-receptor interaction can quantitatively be characterized by the binding kinetics (rate constants and equilibrium constants). The association and the dissociation rate (k_a and k_d) can be extracted from the association and the dissociation phases in the SPR sensogram, respectively. The binding affinity (i.e. equilibrium constant K_A or K_D) can be calculated from the two rate constants

(i.e. $K_A = k_a/k_d$). In addition, the affinity can be extracted from the equilibrium SPR signals at different concentrations through a Langmuir fit (Frazier et al., 2008).

2.1.3.2 Applications of SPR

Specific interaction analysis. The binding affinity, the binding kinetics and the drug residence time are the key biochemical aspects of the drug-targets (Fang, 2012). SPR allows a direct and a quantitative determination of the specific interactions without the need of the labels. SPR has been playing a role in target characterization, compound screening and lead optimization and early ADMET (Cooper, 2002). In particular, the SPR biosensor array based on SPR imaging technique enables a high throughput (HTS) screening, which allows up to 1000 samples per day (Renaud & Delsuc, 2009). Cell-based SPR biosensors have also been tested for ligand affinity evaluation of a membrane receptor (Mizuguchi et al., 2012). Many of the interactions in the drug discovery process are related to cell surface receptors such as G-protein-coupled receptors (GPCRs) (Cooper, 2002). SPR makes it possible to directly screen the ligand of a membrane-bound receptor by utilizing the surface receptors of the living cells (Canovi et al., 2012; Hong et al., 2007; Kocbek et al., 2007; Patil et al., 2009). In these studies, the specific interactions of targeted nanoparticle drug delivery systems (functionalized liposome nanoparticles, PLGA nanoparticles, dendrimer-based anticancer nanotherapeutics and ligand-functionalized polymeric nanoparticles) with surface immobilized receptors have been analyzed by using SPR biosensors.

Characterization of membrane. Another benefit of SPR in pharmaceutical related research in addition to interaction analysis is the characterization of membranes. Deposition of an organic layer on the metallic/dielectric interface shifts the position of the resonance angle (θ_{SPR}) to higher values. The shift in the resonance angle ($\Delta\theta_{SPR}$) is directly proportional to the optical thickness [i.e. the product of the geometric thickness of the organic layer (d) and the refractive index difference between the real refractive indices of the layer and the medium (Δn)]: $\Delta\theta_{SPR}=k\Delta nd$, where k is a constant reflecting the experimental conditions) (Boncheva & Vogel, 1997; Caide & Sui, 1999). Measuring $\Delta\theta_{SPR}$ allows the determination of the optical thickness of the adsorbed organic layer. Either the refractive index (n) or the geometric thickness (d) of the organic layer has to be known in order to obtain the other. Both refractive index (n) and geometric thickness (d) can be simultaneously extracted if the organic layer is measured by SPR in two different media or in one medium with two different laser wavelengths. The physical parameters of the lipid bilayer have an effect on the transport of a drug through the cellular membrane and on the drug release from liposomes, which are nanoparticles consisting of lipid bilayers. The different states of lipid bilayers (gas phase, liquid phase, solid phase or mixed phase) can be reflected by the change in the refractive index of the lipid bilayers.

2.1.4 Quartz crystal microbalance (QCM)

2.1.4.1 Basics of QCM

Piezoelectric effect. The word "piezoelectric effect" was discovered by the brothers Pierre and Jacques Curie in 1880 (Curie & Curie, 1880) and named by Hankel one year later (Hankel, 1881). The piezoelectric effect reflects the linear electromechanical interaction between the mechanical and the electrical states in special crystalline materials (called piezoelectric materials) without the inversion of the symmetry. In the original state, the gravity centers of the negative and positive charges of each molecule coincide, and the external effects of the negative and positive charges are reciprocally counterbalanced. When pressure is applied on the piezoelectric material it will undergo a deformation which induces the separation of the positive and the negative gravity centers. The piezoelectric material is thereby polarized and an electric potential occurs. (Arnau, 2008) Thus, the mechanical energy load (pressure) is transformed into electrical energy. The piezoelectric effect is a reversible process. When a voltage is exerted between the electrodes deposited on the piezoelectric material, a mechanical strain will likewise be produced in a piezoelectric material (reverse piezoelectric effect).

Thickness-stress mode (TSM) resonator. Bulk acoustic wave (BAW) or surface acoustic wave (SAW) can be utilized in acoustic wave sensors. QCM is based on BAW propagating through the bulk material, which allows operation at high frequencies, even up to GHzs (Corso, 2008). BAWs are generated by applying an electrical high-frequency (HF) signal to the electrodes (Arnau, 2008). Quartz is the most widespread commercially used piezoelectric material because of its unique mechanical, electrical, chemical and thermal properties (Cheng et al., 2012). In addition, quartz is an anisotropic material of which elasticity, piezoelectric property and temperature coefficient etc. are strongly dependent on the direction of the cut of the crystal. The QCM technique often utilizes a quartz crystal wafer cut in the AT form in which the quartz is cut normal to the Y axis, parallel to X-axis and rotated by 35° 15′ from the optical Z-axis (see the Cartesian axes for a quartz crystal in Figure 3b) (Lee & Lee, 1996; Marks, et al., 2007). The AT-cut quartz crystal has nearly zero frequency drift around room temperature. Therefore, the oscillation of AT-cut is rather stable at room temperature in the thickness shear mode (TSM) (Cheng, et al., 2012). Hence the QCM sensors are also called TSM sensors. In the TSM, a generated acoustic wave propagates in a direction perpendicular to the plate surfaces when a voltage is applied between the electrodes. A transverse shear wave in parallel to the electric field propagates through the thickness of the plate. Particle displacements take place in parallel to the surfaces (Figure 3a). The crystal produces an electromechanical standing wave. Under the resonant conditions, a maximum displacement is reached and the crystal surface is quite sensitive to mass change, which is reflected as a change in the resonant frequency of the QCM device. (Janshoff et al., 2000; Marks, et al., 2007; Su et al., 2000; Thompson et al., 1991) The schematic illustration of a QCM biosensor setup, based on TSM sensor, is shown in Figure 3a. The fundamental resonant frequency of the quartz crystal is dependent on and inversely proportional to the crystal thickness. A thin

disc of AT-cut quartz (coated with gold) with a typical fundamental resonance frequency of 5 - 20 MHz is usually used as the TSM resonator (QCM).

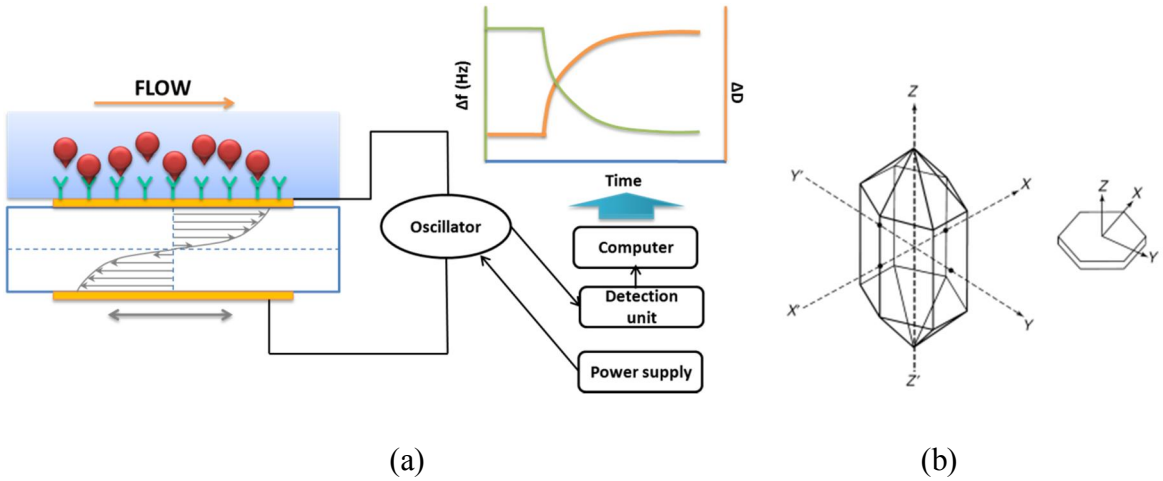

(a) (b)

Figure 3. *a) Schematic illustration of QCM working principle (TSM sensor), and b) Cartesian axes for a quartz crystal (Marks et al, 2007).*

Quantitative aspect of QCM. As described above, the QCM biosensor is based on the TSM resonator with a gold coated AT-cut quartz crystal as the sensor chip. It monitors the changes in resonant frequency resulting from molecular adsorption on the surface of the electrode. In 1959 Sauerbrey presented the first quantitative relation correlating the mass of adsorbed material to the decrease in frequency. The relation is called the Sauerbrey equation (Sauerbrey, 1959):

$$\Delta f = -N \frac{2 f_0^2}{\sqrt{\mu_q \mu_q}} \cdot \frac{\Delta m}{A} = -N \Delta m / C_f \quad (4)$$

where Δf is the measured resonant frequency shift (Hz), Δm is the mass change, f_0 is the intrinsic fundamental frequency of the crystal, μ_q is the shear modulus of the crystal (2.95×10^{11} g cm^{-1} s^{-2}), ρ_q is the density of the crystal (2.65 g/cm^3), A is the area (cm^2) of the quartz plate (between the two electrodes of the opposite faces), N (=1, 3, 5,…) is the overtone number, and C_f is the integrated QCM/mass sensitivity or Sauerbrey constant (C_f =17.7 ng cm^{-2} Hz^{-1} for f = 5 MHz) (Sauerbrey, 1959). The C_f is dependent on f_0 and increases proportionally as the overtone number increases. The Sauerbrey equation is applicable to thin, rigid and homogeneous films. At the same time, the adsorbed mass (Δm) on the surface must be less than 2% of the initial mass of the crystal (Campanella, 2010). The frequency change effectively conforms to the increase in mass as predicted by the Sauerbrey equation when the thickness of hydrated polyelectrolyte films is less than 40 nm. The visco-elasticity of the films is observed for films thicker than 90 nm. (Vogt et al., 2004). It is not physically valid for liquids with different stiffness, viscosity, and density from those of quartz. In 1985, Kanazawa and Gordon proposed a new equation, which

correlates the resonant frequency (Δf) to the density (ρ_{liq}) and viscosity (μ_{liq}) of a liquid. This equation is called the Kanazawa equation (Kanazawa & Gordon, 1985):

$$\Delta f = -f_0^{\frac{3}{2}} \sqrt{\frac{\mu_{liq}\rho_{liq}}{\pi \mu_q \rho_q}} \quad (5)$$

where η_{liq} and ρ_{liq} are the viscosity and the density of the liquid. This equation is valid for viscous liquids (i.e. so called Newtown liquids). Deposition of the adsorbed material on the electrode surface can be characterized by monitoring the frequency change (Δf) as a function of time. The QCM signal can be monitored simultaneously at different overtones ($N = 1, 3, 5 \ldots$) if needed.

QCM with dissipation monitoring (QCM-D). In contrast to the normal QCM, the QCM-D allows simultaneous monitoring of the changes in energy dissipation (ΔD) and in the resonant frequency (Δf). Δf is related to the mass of the adsorbed film, while ΔD reflects the changes in the softness (visco-elasticity) of the adsorbed film. Dissipation (damping) is the sum of all energy losses in the system per an oscillation cycle. A soft film deforming during oscillation gives high dissipation, while a rigid layer displays a low dissipation. QCM signals at several overtones enable the determination of the visco-elastic properties, the film thickness, and the film density of soft layers via a suitable visco-elastic model (Liu, 2009). This allows predicting the adsorbed mass and the structural properties of the soft adsorbed layer. Thus, additional structural information of the adsorbed layer can be obtained by the QCM-D technique, which can not be obtained by optical techniques or QCM techniques that do not monitor frequency and/or dissipation changes at several overtones.

2.1.4.2 Applications of QCM

As described above, QCM is a mechanical sensor which is sensitive to mass and visco-elasticity changes at the surface. Applications of QCM are naturally related to adsorption of materials (specific or non-specific) onto the crystal surface. Applications of the QCM biosensor mainly focuses on biological assays (adsorption of protein, DNA-DNA/DNA-protein interaction, cell adhesion, bacteria, virus particle etc.), formation and structure of functionalized surfaces and thin films (LB films, self-assembled monolayers, polyelectrolyte multilayers, lipid bilayers, artificial cell membranes etc.), and in the field of pharmaceutical research (drug-model surface interactions, drug-cell monolayer interactions, partitioning of drugs, and adsorption and interaction of nanoparticles). In these applications, the adsorption of the different materials can be quantified, and the structural properties of the bound layers are characterized by QCM-D. For example, adsorption and fusion of vesicles into lipid bilayers on a solid surface have been studied by using QCM-D (Dorvel et al., 2007; Keller & Kasemo, 1998; Patel & Frank, 2006; Reimhult et al., 2003). Höpfner *et al* investigated the targeting process and the binding behavior of targeted liposomes. It was found that the bound liposomes deformed, which was detected and monitored by QCM-D. (Hopfner et al., 2008) Viitala *et al* monitored the

formation of anionic phospholipid coatings on silica and quantitatively characterized the different structures of the layers formed on the silica surface (rigid supported lipid bilayer (SLB) and visco-elastic supported vesicle layer (SVL)) (Viitala et al., 2007).

2.1.5 Synchronization of SPR and QCM

Based on the different detection principles of SPR and QCM described above, it is worth noting that both the adsorbed material and the entrapped water in the adsorbed layer contribute to the QCM signal. For SPR, however, only the adsorbed material, which usually have a different refractive index from the bulk (i.e. the buffer), can be sensed. SPR is better for determining the binding affinity and the kinetics as the entrapped water (or buffer) in the adsorbed layer do not influence the SPR signal response. On the other hand, QCM allows the extraction of additional information, such as structural and visco-elastic properties of the adsorbed layer. The combined use of SPR and QCM is expected to enable a full insight of interfacial interaction events. The combined use of SPR and QCM has previously been utilized for investigating biomolecular adsorption or surface interaction events. (Ansorena et al., 2011; Che et al., 2010; Laricchia-Robbio & Revoltella, 2004; Malmström et al., 2007; Morigaki & Tawa, 2006; Plunkett et al., 2003; Reimhult et al., 2004)

It is widely accepted that blood stream hydrodynamics is an important pharmacokinetic factor. However, its study has been limited as a result of the difficulty of both measuring these effects and of developing a comprehensive understanding of the results of these measurements. Flow condition is a factor that should not be neglected. In most cases, the difference in the hydrodynamic flow conditions between SPR and QCM devices has either been dealt with only superficially or not at all (Ansorena, et al., 2011; Che, et al., 2010; Laricchia-Robbio & Revoltella, 2004; Malmström, et al., 2007; Morigaki & Tawa, 2006; Plunkett, et al., 2003; Reimhult, et al., 2004). Kim et al. have attempted to construct a device allowing simultaneous sensing with SPR and QCM with the same sensor and flow channel (Kim et al., 2010). In order to extract complementary information from these two techniques it is of utmost importance to synchronize the flow conditions between SPR and QCM instruments.

The hydrodynamic flow conditions for both devices can be synchronized through hydrodynamic modeling by utilizing computational fluid dynamics (CFD). The shear stress on the surface of the corresponding flow channels as a function of the flow rate and the flow channel height can be modeled. Thus, a scaling expression of the flow rate between the different flow channels of the devices can be obtained. The individual flow rates for SPR and QCM devices corresponding to equal shear stress in the different flow channels can then be calculated by using the scaling expression.

2.2 Model membranes in pharmaceutical research

The greatest challenge in label-free detection is the immobilization of an active receptor or ligand (e.g. proteins) onto the sensor surface without disrupting its activity. The

biological membrane (cellular membrane) is one of the most important and basic constituents in all of the living organisms. It has a lipid bilayer structure, which separates the cell contents from the external environment. In addition to the lipid (amphipathic) bilayer, the functions of the cellular membrane are mainly performed by membrane proteins (peripheral or integral protein), carbohydrates, their complexes and other constituents, such as metallic ions and pigments. (Figure 4) These components regulate the selective transport of molecules into and out of the cell, and mediate all the communications between the intracellular and the extracellular spaces, and thus also the cell-cell communication. (Reimhult, et al., 2003; Tien & Ottova-Leitmannova, 2000) A number of receptors on the cellular membrane surface are potential drug targets. The interaction of the drug-membrane receptor is a prerequisite for drug action. The interaction of the drug or the drug delivery system (e.g. nanoparticle with immobilized ligand) with the cellular membrane enables the intracellular delivery of the drugs. In 1972 Singer and Nicolson proposed a Fluid Mosaic Model of biological membranes, where the biological membrane is deemed to be a two-dimensional fluid (or liquid crystal). Some of the membrane proteins are anchored to a network of the protein filaments within the cytoplasm. Other membrane proteins and integral components such as lipids are free to diffuse laterally, but constrained within the plane of the membrane (Singer & Nicolson, 1972). The interaction of drug candidates with membrane protein receptors like G protein coupled receptor (GPCR) have widely been used for HTS drug screening (Eglen et al., 2008; Fang et al., 2008; Halai & Cooper, 2012; Li et al., 2006; Wang et al., 2012).

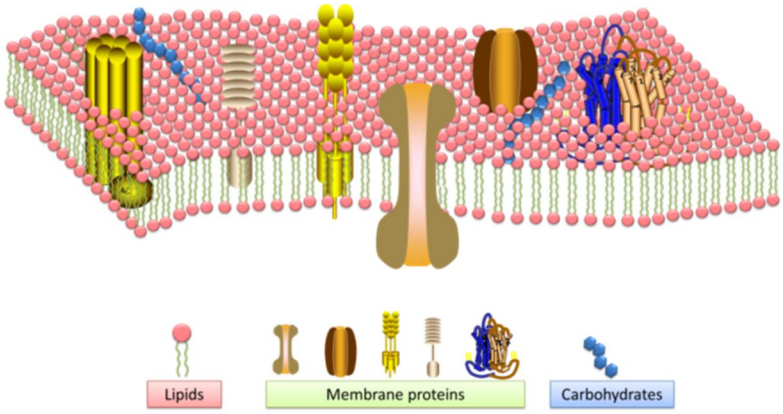

Figure 4. *Simplified structure of the cell membrane and its components.*

It is worth noting that natural biomembranes usually have highly complex structures. The presence and the interplay of the different components in biomembranes maintain the cellular functions. However, the highly complex structure of the biomembranes and the interplay processes hampers membrane related research. Therefore, efficient and cheap biophysical detection is a promising option for studying ligand-membrane receptor interactions. This is achieved by using a simplified model of the lipid bilayer with integrated receptors, which allow the investigation of the binding affinity and kinetics of a biological processes occurring at the cellular level. Through additional information about

the ligand/drug-receptor interactions, drug absorption, viral attack, and cellular signaling events, which are difficult to obtain by traditional cell assays, are enabled by biophysical detection at the molecular level (Castellana & Cremer, 2006). These interactions with membrane receptors are surface-related processes that are difficult to study with bulk techniques (Cooper, 2002). Fabricating simplified membrane models with an incorporated receptor on a non-labelled surface sensitive sensor surface is a very promising platform for performing such ligand-membrane receptor interaction studies.

2.2.1 Model membranes with integrated receptors

The lipid bilayer is one of the most typical simplified model membranes due to its similarity to cell membranes. In addition, a number of films such as self-assembled monolayers (SAMs), polymer membranes and vesicle monolayers can integrate a receptor and function as a model membrane.

2.2.1.1 Self-assembled monolayers (SAM)

The molecular self-assembly of thiol- or disulfide molecules on metal surfaces is one of the most widely used methods to modify a solid surface for receptor immobilization. SAMs can be prepared so that they minimize non-specific adsorption and introduce reactive groups for immobilization of a receptor on a metal surface. At the same time, it is possible to control the orientation of the immobilized receptors. The pioneering work by Nuzzo and Allara reported the spontaneous formation of ordered organic disulfide monolayers on a gold surface in 1983 (Nuzzo & Allara, 1983). Spontaneous self-assembly of alkylthiols on a metallic (gold or silver) surface is driven by the chemisorption of sulfur on the gold surface and the weak interactions between the long alkyl chains. The self-assembly is first initiated by the strong chemical interaction between the sulfur and the gold surface, followed by the reorganization of the adsorbed thiols into a monolayer driven by the weak interactions (e.g. van der Waals) between the alkyl chains. SAMs are easily prepared by simply immersing the gold substrates into the solution containing thiol molecules. The SAMs formed in this way are densely packed and ordered monolayers. Therefore, it is a powerful approach for surface modification of gold coated sensors.

Functionalized self-assembled monolayers. The end group of the alkyl chains of alkanethiols can be modified with a functionalized group (e.g. an amino-, carboxyl-, hydroxyl-, maleimide-, succinimidyl ester- or biotin group etc.). These groups can react with the receptor (e.g. protein) and thus immobilize them onto the SAMs. Biotinylated molecules can be immobilized onto the SAMs containing biotinylated thiols with the help of the strong and specific interaction of biotin with streptavidin. This simple and highly specific immobilization process is called capturing.

Mixed self-assembled monolayers. A mixed SAM can be formed if the mixture of the two different types of thiols is used. For example, the mixture of the functionalized and the non-functionalized thiols can form a SAM with diluted coupling sites, which reduces

the amount of receptors immobilized on the SAM. Thus, the receptor density on the SAM surface is easily controlled. The mixed SAM of a biotinylated thiol and a non-bionylated thiol is a good example, where the biotin density on the surface is controlled by utilizing different ratios of the biotinylated thiol (Nelson et al., 2001).

Blocking non-specific interaction. Bioinert surfaces are required in order to avoid the effect of non-specific binding on biological interaction measurements. Poly- and oligo (ethylene glycol) (PEGs and OEGs) are known to reduce the nonspecific adsorption of proteins and other bioactive molecules (Li et al., 2007; Schreiber, 2004). OEG-terminated thiols form bioinert SAMs, which can block the non-specific interaction to a great extent. However, it is possible that there are some defects in the thiol SAMs, which are also a source of non-specific binding sites. These can be blocked with BSA (Tang et al., 2006).

2.2.1.2 Hydrogel membrane

Hydrogels, which are three-dimensionally cross-linked hydrophilic polymer networks, are able to absorb a large quantity of water or aqueous solutions (up to 99% (w/w) water of their dry weights) and swell, but still remain insoluble (Yang et al., 2004). Their specific properties, such as a high degree of flexibility similar to natural tissue, as well as their softness and stability in an aqueous media endow hydrogels good biocompatibility. Hydrogels are promising materials in biomedical applications, such as in drug delivery, tissue engineering, and biosensors (Hamidi et al., 2008; Kim & Lee, 2006; Mateescu et al., 2012; Schloßmacher et al., 2013; Xu et al., 2006). Thus, for sensing purposes hydrogels provide a biomimetic microenvironment that mimics the extracellular matrix (ECM), which is the key for maintaining cellular functions.

Hydrogels on substrates. Cross-linking is an important step to form a hydrogel. This can be done by two different methods: 1) chemically cross-linked hydrogels and 2) physically cross-linked hydrogels. Chemical hydrogels are cross-linked into networks by covalent bonds, while the network structures of physical hydrogels are maintained by non-covalent interactions, such as hydrophobic and electrostatic interactions or hydrogen bonds (Buenger et al., 2012). Thereby, the physical hydrogels may be reversible in certain conditions. The polymerization of hydrogels can be achieved by *in situ* crosslinking or post-synthetic crosslinking of the polymers. For *in situ* crosslinking, the monomers with multiple polymerizable sites are coated on a substrate followed by polymerization into a hydrogel network. The polymerization may be accelerated by light or heat. In post synthetic crosslinking the substrate is first coated by a soluble precursor polymer and then cross-linked into a hydrogel network onto the substrate. Hydrogels can be attached to the substrate surface by covalent bonds or non-covalent physical adsorption through electrostatic and acid-base interactions. (Datta, 2007; Mateescu, et al., 2012; Vermonden et al., 2012; Wilson, 2009)

Hydrogels on biosensors. The bio-inertness of a surface is crucial for its application in biosensors. Well-designed hydrogels exhibit low non-specific interactions and allow covalent immobilization of a receptor, while simultaneously minimizing the damage of the bio-functionality of the target receptor (Andersson et al., 2008). Hydrogels enables the

formation of a porous 3D membrane with a highly open structure and a large inner surface on a sensor surface. Both the membrane surface and the inner porous space are available for the immobilization of functional molecules (e.g. receptors) (Mateescu, et al., 2012). At the same time, the number of coupling sites is also increased due to additional reactive groups resulting from branched linker molecules (Oh et al., 2006). The binding capacity of the hydrogel membranes is correspondingly increased which enhances the sensing signal intensity. This is especially useful for measuring small molecules, which usually produce small signals. A more natural microenvironment, similar to the ECM, can increase the stability of biomolecules (Orive et al., 2009). In addition, 3D hydrogels provides a relatively free movement of the biomolecule, which is advantageous when measuring e.g. ligand-receptor interactions (Charles et al., 2004). One of the most successful examples for the application of hydrogels in biosensing applications is the dextran-coated sensor chips developed for SPR by Biocore (http://www.biacore.com). The dextran coated SPR sensor chips have widely been applied in biomolecular interaction analysis (Lofas & Johnsson, 1990). Hydrogel layers have also been employed as a support for lipid bilayer membranes (Kibrom et al., 2010; Tanaka & Sackmann, 2005; Wagner & Tamm, 2000). In these, the hydrogel cushion provides a hydrophilic microenvironment, which prevents the denaturation and the deformation of transmembrane proteins (Mc Cabe & Forstner, 2013). Furthermore, 3 D hydrogel membranes have been utilized for cell-based biosensors where the cells are encapsulated in the hydrophilic hydrogel matrix (Koh et al., 2003; Koh & Pishko, 2006; Mao & Kisaalita, 2004; O'Connor et al., 2000). Stimuli responsive hydrogels are sensitive to the changes in the surrounding environment, e.g. pH, temperature, ions, electric field, light and solvent (Marks, et al., 2007).

Hydrogel membranes can be prepared in several ways on a substrate. The spin and dip coating methods are the mostly widely used techniques. In the spin coating method, a polymer solution is dropped on the substrate while simultaneously rotating the substrate (tens of rpm up to thousands of rpm), which causes the polymer to spread over the substrate. The film becomes homogeneous with the help of centrifugal forces. After that, the spin-coated membrane is usually cross-linked. The spin coating technique enables the deposition of thin and uniform polymeric membranes. The thickness of the membrane depends on the rotation speed and the viscosity of the polymer solution. Dip coating relies on the adsorption of the polymer from the solution. The thickness of the membrane can be controlled by the dipping time and the polymer concentration. A good example is polyelectrolyte adsorption on a charged substrate through coulombic interactions. If a polycation and a polyanion are alternately used, a multilayer polyelectrolyte membrane can be formed. (Hall et al., 2004; Mateescu, et al., 2012; Mennicke & Salditt, 2002; Scriven, 1988; Turiel, 2005; Wilson, 2009; Zribi & Fortin, 2009)

2.2.1.3 Langmuir-Blodgett (LB) films

The study of Langmuir films was pioneered by Benjamin Franklin who found in 1774 that oil spread as a monolayer on a water surface (Roberts, 1990). Subsequently the floating monolayer (Langmuir monolayer) was first systemically studied in 1920 by

Irwing Langmuir (Langmuir, 1920) who was awarded the Nobel Prize in 1932, partly due to these studies. Later Katherine Blodgett described the transfer of sequential monolayers onto a solid substrate by vertically moving the solid substrate through a monolayer/air interface (Blodgett, 1934, 1935). Such a deposited monolayer on a solid substrate is called a Langmuir-Blodgett (LB) film. The materials for forming LB films are amphiphilic molecules, which contain a polar hydrophilic head group and a nonpolar hydrophobic tail group. Fatty acids and phospholipids are typical examples of such amphiphilic LB materials. The LB film technique is based on the self-organization of the amphiphilic molecules at an air/subphase (e.g. water) interface. When amphiphilic molecules (e.g. lipids) are spread on the air/water interface, they, in order to diminish the free surface energy, will self-organize into a dispersed monolayer with the polar head groups in the water phase and the nonpolar tail group towards the air (Figure 5b). The dispersed monolayer is then horizontally compressed and subsequently transferred onto a solid substrate by the vertical transfer method (Figure 5d). In addition, it is possible to transfer the monolayer horizontally onto solid substrate (not shown here). In such a case, the deposited monolayer is called a Langmuir-Schaefer film. Langmuir-Schaefer deposition is achieved by moving the solid substrate horizontally through the interface either from the gas phase to the liquid phase, or from the liquid phase to the gas phase (Balasubramanian et al., 1995). Multilayers are obtained by repeating the transfer procedure.

An LB monolayer is usually deposited using an equipment called Langmuir-Blodgett (LB) trough, which consists of a trough made of hydrophobic materials (usually Teflon), two barriers and a balance measuring the surface pressure (Figure 5a). After spreading the molecules on the subphase, a two-dimensional closely packed molecular monolayer is formed by compressing the monolayer with the barriers. The immersed substrate in the subphase is lifted with a slow and constant speed, which enables the deposition of the LB monolayer onto the substrate (Figure 5d). During the deposition, the surface pressure (π) is monitored in real time by a balance based on the Wilhelmy plate (usually made of platinum or filter paper) method. The plate is partially immersed into the subphase and a meniscus forms between the Wilhelmy plate and the liquid surface. The surface pressure (π) can be calculated based on the surface tension, the weight of the plate and the buoyant force of the plate. The area per molecule can be calculated from the number of molecules spread on the subphase and the surface area of the subphase available to the molecules. The plot of the surface pressure (π, mN/m) during barrier compression as a function of the area per molecule forms a surface pressure (π)-area (A) isotherm (Figure 5c). As the monolayer is compressed, it may exhibit different phases, such as the gas state (G), the liquid expanded (LE) state, the liquid condensed or crystal state (LC) and the solid state (S), which are reflected in the π-A isotherm. Additionally mixed phases such as LE/G and LC/LE may also occur (Figure 5c).

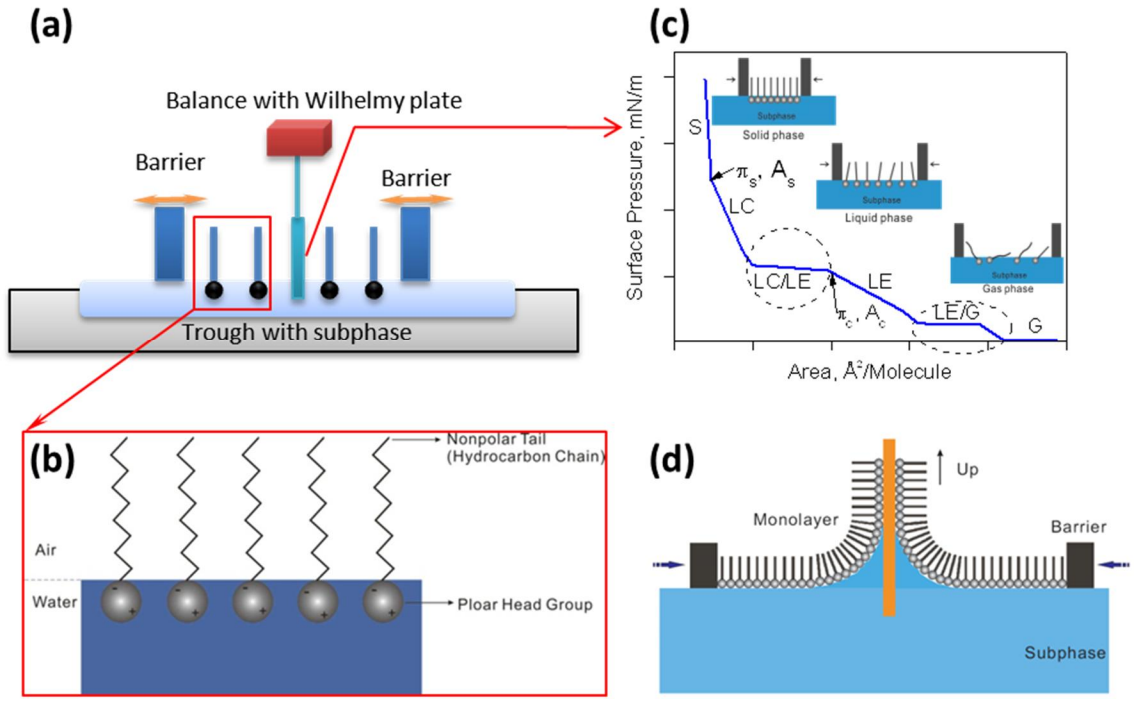

Figure 5. *a) Schematic illustration of a Langmuir-Blodgett (LB) trough, b) Model of a monolayer on the air/water interface (Liang, 2010), c) Monolayer phases along an isotherm. The dashed lines mark coexistence ranges of the LE and gaseous (G) phases and of the LE and LC phases (Mohwald, 1990), and d) Vertical transfer of LB monolayer, (Liang, 2010).*

Mono- or multilayers can easily be deposited by using the LB deposition technique. At the same time, the thickness and the molecular organization of the deposited layers can be accurately controlled. The LB technique enables the deposition of multilayers up to hundreds of layers, thus allowing an accurate control of the film thickness based on the number of layers. The phases reflected in the π-A isotherm provides clues to control the molecular organization of the layer by controlling the surface pressure combined with the composition of the subphase. The structure of the layers can be controlled by varying the layer compositions or in some cases by varying the subphase composition. In addition to the layer materials, biomolecules such as enzymes, proteins or membrane proteins can be incorporated in the deposited layers. This makes the LB technique a useful technique for constructing functional membranes for studying ligand-receptor interactions. The LB technique enables the deposition of homogeneous monolayers over large areas on almost any kind of solid substrate. (Martin, 2007) However, defects may sometimes occur in the deposited layers, especially for multilayers from successive layer transfers (Schwartz, 1997). Therefore, it is important to take precautions for preventing contamination during film preparation (Wilson, 2009). The times between spreading the monolayer, compression of the monolayer, and transfer of the monolayer after the deposition pressure has been reached are vital for controlling possible defects in the deposited layers due to the loss of monolayer integrity and stability (Martin, 2007).

The greatest benefit of the LB technique is the ability to easily create lipid monolayers at the air/water interface or lipid bilayers on a solid substrate. One of the most commonly used applications of the LB technique is to study protein-lipid interaction at the air/water interface. The protein is injected in the subphase and its adsorption to the lipid Langmuir monolayer is monitored as changes in the surface pressure or the molecular area of the lipids (Martin, 2007). The Langmuir monolayer with the adsorbed proteins can further be transferred onto a solid substrate. The protein is thus incorporated in the LB films. Through this procedure, accurately controlled lipid bilayers with incorporated membrane surface receptors are easily constructed. Thus, it is possible to measure drug-receptor interactions or to screen a lead compound by using label-free biosensing techniques. The use of crosslinking agents enables covalent immobilization of a protein or an enzyme onto lipid LB films. However, covalent immobilization of a protein or an enzyme can cause losses in their activity. Another approach available for incorporating the protein is ligand capturing. The streptavidin-biotin pair is a good example of this. Ligand capturing by utilizing the streptavidin-biotin pair can be achieved by spreading biotinylated lipids at the air/water interface followed by injection of streptavidin into the subphase. The strong specific interaction between streptavidin and biotin at the air/water interface promotes the incorporation of streptavidin into the monolayer. The incorporated streptavidin is further deposited onto a solid substrate together with the monolayer. (Ahlers et al., 1989; Tredgold, 1994) Additionally, the LB technique enables the preparation of polymer mono- or multilayers by spreading polymers containing both hydrophilic and hydrophobic side groups, followed by transfer onto a solid substrate (Tredgold, 1994). This is useful for fabricating lipid bilayers on a polymer cushion, which provides a hydrophilic environment for the biomolecules, such as enzymes or proteins.

2.2.2.4 Lipid Bilayer membranes

Lipid bilayers have attracted a great deal of interest since they are the fundamental structures of all biological membranes. Lipid bilayers play a key role in the mass transport in and out of cells, cell structures, protein host matrixes, energy generation and storage etc. (Ries et al., 2004). Lipid bilayer based membrane models with varying compositions, structures, complexity and missions have been developed to elucidate the structural information of the bilayer membrane (Friedrich et al., 2004; Gliozzi et al., 2002), mimic the function of the biological membrane (Giess et al., 2004; Plant, 1999) or clarify the interaction of drug-membrane receptor systems (Boulbitch et al., 2001; Loidl-Stahlhofen et al., 2001; Rossi & Chopineau, 2007). Well-defined lipid bilayer membrane models enables membrane related studies to be performed at a molecular level with only the desired function of the biological membrane taking place. Typical membrane model systems include black lipid bilayers, solid supported lipid bilayers, tethered lipid bilayers and polymer cushioned lipid bilayers.

Black lipid bilayer. A black lipid bilayer membrane is a free-standing planar film which spans the aperture of a hydrophobic film such as Teflon (Figure 6a). The lipid bilayer appears black due to the interference of the reflected lights at the different interfaces

(hydrophilic side and hydrophobic side). The first black lipid bilayer was prepared by Mueller *et al* in 1962 through painting a lipid solution in an organic solvent over an aperture (Mueller et al., 1962). The solvent residue in the black lipid bilayers prepared by this approach is disadvantageous for incorporating membrane protein. The black lipid bilayer can be prepared by the Langmuir film approach, where a lipid bilayer on the aperture is formed by lowering and raising the surface of the subphase on which the Langmuir monolayer is floating (Montal & Mueller, 1972). The physico-chemical properties of the lipid membranes, especially the electrical properties, can be characterized by using black lipid bilayer membranes. Black lipid bilayers are sensitive to change in electrical properties like conductance and dielectric constant of the membrane, and the surface charges (Winterhalter, 2000). For example, proton pumps can be investigated by using the black lipid bilayers (Bamberg et al., 1993).

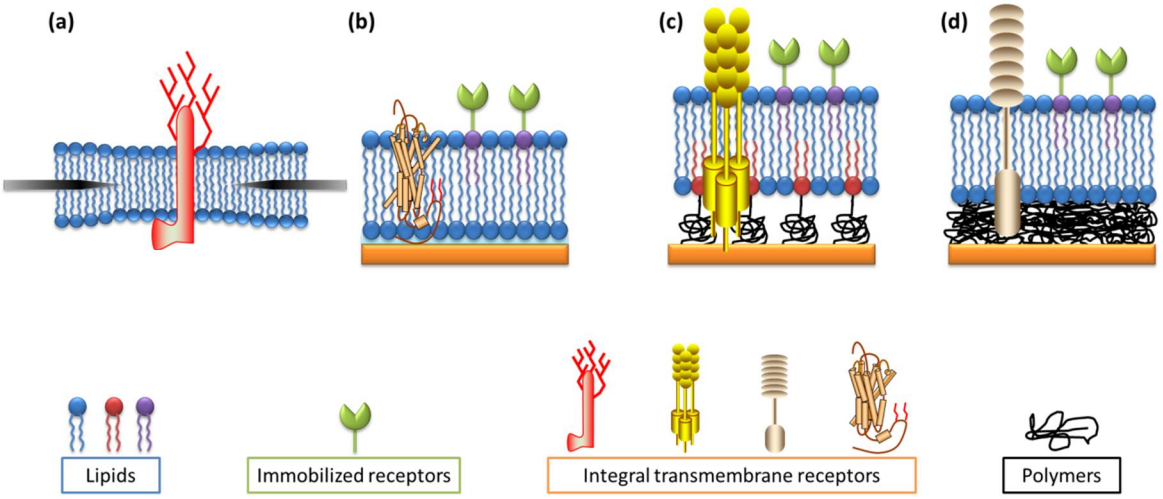

Figure 6. *Different model lipid bilayer membrane systems. a) Black lipid bilayer, b) Solid supported lipid bilayer, c) Polymer tethered lipid bilayer, and d) Polymer cushioned lipid bilayer.*

Solid supported lipid bilayer (sSLB). Solid supported lipid bilayers (sSLBs) are utilized for analytical techniques with non-labelled detection due to their biomimetic properties with structures and functions comparable to cellular membranes. An sSLB is a lipid film deposited on a solid substrate in a direct contact with the solid support (Figure 6b), being more robust and stable than the black lipid bilayers. sSLBs are constructed by fusing vesicles onto a hydrophilic substrate (Castellana & Cremer, 2006; Cohen et al., 1980; Kalb et al., 1992), or transferring a lipid monolayer onto a substrate using Langmuir-Blodgett (LB) or Langmuir–Schaefer techniques (Tamm & Mcconnell, 1985). Additionally, the combined use of vesicle fusion and LB transfer can also be utilized for creating sSLBs (Castellana & Cremer, 2006; Kalb, et al., 1992). Lipid bilayers stable in air are preferred for their applications as biosensors, because the lipid bilayers on the sensor chip needs to be constantly hydrated. When hydrated, solid supported lipid bilayers in direct contact with the substrate can peel away from the substrate surface into vesicles, due to the introduction of an air/water interface from the edge of the substrate. Air-

stability of sSLBs can be improved by fabricating hybrid bilayers, protein stabilized lipid bilayers or polymerized membranes. (Castellana & Cremer, 2006) The direct contact of the lipid bilayer with the substrate can induce problems with sSLBs. When transmembrane proteins are incorporated in the lipid bilayer membranes, then the interactions between the protein and the substrate can affect the structure and activity of the transmembrane proteins and even induce denaturation.

Tethered lipid bilayer (TLB). The disadvantages of sSLBs can be avoided by preparing the lipid bilayers on a spacer (Figure 6c). The tethered layer is usually attached to the supporting surface by covalent coupling. This enhances the stability of the TLB and protects it from dissociating from the supporting surface. Many methods are available for preparing TLBs. One approach is to form a hybrid TLB consisting of a lipid bilayer and a self-assembled monolayer (SAM). A hybrid TLB can be accomplished by first depositing a SAM of alkanethiol-lipids (anchor lipids) on a gold surface followed by the deposition of the lipid bilayer onto the SAM by using the Langmuir-Blodgett (LB) technique or the vesicle fusion (Junghans & Koper, 2010; Knoll et al., 2008). DNA has also been used for creating TLBs. In such a case, a glass surface is modified by self-assembled alkylsilane monolayers, followed by immobilization of single strand DNAs via covalent bonds. Vesicles containing the complementary DNA stand linked to lipids are then fused into a lipid bilayer on the DNA functionalized self-assembled alkylsilane monolayers. Thus, the lipid bilayer is tethered by the interaction between complementary single strands of DNA (Chung et al., 2009). Protein (Giess, et al., 2004; Knoll, et al., 2008) and PEGylated lipid (Junghans & Koper, 2010) tethered lipid bilayers have also been prepared.

Polymer cushioned lipid bilayer. Hydrophilic polymer membranes are always attractive for studying the specific interactions biomolecules, because they resist nonspecific biomolecular binding. Polymer cushioned lipid bilayers also provide a friendly microenvironment to e.g. transmembrane proteins. A well-defined polymer cushion film behaves much like a cytoskeleton, which supports the cellular membrane (Castellana & Cremer, 2006). Several types of polymers such as dextran (Elender et al., 1996; Gyorvary et al., 1999), cellulose (Setaka et al., 1982), chitosan (Baumgart & Offenhausser, 2003; Zhang et al., 2010), polyethylene glycol (PEG) (Watkins et al., 2011), poly-L lactic acid (PLLA) (Duan et al., 2006), agarose (Baumgart & Offenhausser, 2003), polyelectrolytes (Majewski et al., 1998), and lipopolymer (Junghans & Koper, 2010) have been employed as lipid bilayer cushions. A typical polymer cushioned lipid bilayer is shown in Figure 6d. The polymer cushioned lipid bilayer systems can be achieved by two methods: independent polymer cushioning the bilayer and coupled membrane-polymer systems. In the independent polymer cushion method, the lipid bilayers are physically adsorbed on the polymer cushion, while in the latter method hydrophobic chains linked to the polymers are integrated into the lipid bilayer (Mc Cabe & Forstner, 2013). The lipopolymer cushion is widely used and is a typical example for the coupled membrane-polymer systems. The polymer cushion can be deposited by either spin- or dip coating. In addition, Langmuir-Blodgett and Langmuir–Schaefer depositions are also options for depositing polymer cushions. The lipid bilayers are then formed onto the polymer cushion by using vesicle fusion, Langmuir-Schaefer or Langmuir-Blodgett deposition, or a combination of LB

deposition methods. The increased complexity of the fabrication process is the main shortcoming of the polymer cushioned lipid bilayer.

2.2.2 Cell monolayers

The benefit of using cell monolayers in pharmaceutical research relates to *in vitro* prediction of the transport of a drug across membranes, such as the intestinal membrane, into the systemic circulation, which is one of the limiting factors for successful therapeutic application of new oral drugs. Two of the most commonly used cell monolayer model systems for drug absorption tests are the madin-darby canine kidney (MDCK) (Irvine et al., 1999) and the carcinoma colon 2 (Caco-2) cell lines (Shah et al., 2008), which both form a monolayer with tight junctions. The MDCK cell line is frequently used to monitor intestinal drug transport. In addition to the traditional applications of cell lines, cells can also be directly cultured onto a sensor chip surface to form a cell monolayer. Such cell monolayers are called cell on a chip. These systems allow for cell-based label-free biosensing detection. The cells on a chip method combined with well-designed label-free techniques allows noninvasive investigations of biological processes at the cellular level, such as the interaction of ligand-membrane receptor, transport of drug or nanoparticle across membrane, cell adhesion, signaling, infection, migration etc. As discussed above, many cell-based label-free sensing devices such as SRU BIND, iCELLigence and CellKey® have been commercialized for high throughput screening (HTS) of lead compounds. The most common assay of these HTS screening devices is the label-free cell-based assay for GPCR screening, where ligand-induced responses in living cells are monitored by sensitive label-free techniques. Optical, electrical and acoustic transducers may be utilized to transform a specific molecular recognition event or a ligand-induced change in a cell layer into a quantifiable signal. (Fang, et al., 2008) The cell-based label-free detection is a method with high potential for characterizing the interactions between nanoparticles and a target surface, and the internalization of nanoparticles into cells.

2.2.3 Characterization of model membranes

The physical properties of the membranes deposited on a sensor chip are vital for a well-designed or customized surface for biosensing purposes. For example, the thickness of the functionalized membrane for SPR is limited by the penetration depth of the evanescent wave into the ambient medium in contact with the sensor surface (usually about 300 nm, depending on the wavelength of the incident light used) (Homola et al., 1999) The molecular recognition event should take place within the evanescent field in order to be monitored. Alternatively, the molecular recognition event can excite a change in an area within the evanescent field. Additionally, the structure of the membrane, the orientation of the membrane materials and the immobilized receptors also have an effect on successful signal detection. Therefore, the characterization of the physical properties of the functional layers, such as thickness, refractive index, structure and visco-elasticity are

important in developing well-defined functionalized membrane surfaces for non-labelled sensing.

There are several techniques that provide accurate information of organic thin film properties which are commonly used for thin film characterization, e.g. ellipsometry, surface plasmon resonance spectroscopy (SPR), quartz crystal microbalance (QCM) and atomic force microscopy (AFM) etc.

Ellipsometry is an optical technique based on polarized light and allows the determination of thickness (d) and refractive index (n) of thin organic layers. However, ellipsometry requires that either the thickness or the refractive index should be known, approximated or measured by other techniques in order to determine the other. Ellipsometry also faces a challenge to provide accurate values for organic layers with thicknesses below 10 nm (Tonova et al., 1996).

Multi-wavelength- or multiple media SPR methods, or a combination of these, enables to simultaneously determine the thickness and the refractive index of thin films without any assumptions. This is useful for the characterization of membranes when developing the protocols for preparing well-defined or customized model membranes for label-free detection techniques. The values of the thickness or the refractive index taken from the literature are usually not applicable due to different deposition conditions. The possibility to simultaneously determine the thickness and refractive index for various types of membranes is therefore desired.

QCM can be utilized to monitor the deposition of a membrane in real time as changes in frequency and dampening of the oscillation. The thickness, density and visco-elasticity of the deposited membrane can be obtained through theoretical modeling, if the change in the frequency and the dampening of the oscillation are measured at several overtones.

AFM utilizes a sharp cantilever probe tip to approach the membrane surface and to image the topography of surfaces with an atomic or a molecular resolution. Additionally, mechanical property (visco-elasticity) and interactions with the surface can also be measured by AFM. (Binnig et al., 1986)

Polarization modulated infrared reflection absorption spectroscopy (PM-IRRAS) is a reflection based infrared spectroscopy technique in which both p- and s-polarized spectra are simultaneously monitored from a sample deposited on an IR reflecting substrate, such as an air-metal interface. If a conductive substrate (e.g. gold) is used, an amplification of molecular dipoles perpendicular to the surface will occur, while dipoles parallel to the surface are at the same time eliminated. This can be utilized for qualitatively determining the orientation/conformation (e.g. gauche or all-trans) and the packing of molecules on the substrate. The molecular packing density and the orientation changes are reflected by the frequency or the intensity of the bands. (Dluhy et al., 2006; Mendelsohn et al., 2010)

Brewster angle microscopy (BAM) allows to visualizing two-dimensional monolayers (e.g. Langmuir monolayer) at the air/water interface, including morphology, size, shape and heterogeneity of domains in the monolayer. In BAM, a polarized light is introduced at the air/water interface at an incident Brewster angle. The difference in the reflectivity resulting from the different refractive indices for the water and the monolayer produces a contrast, which forms an image. (Dynarowicz-Latka et al., 2001; Sherwin, 2011)

Additionally, the detection of the electrical properties of membranes is also important, because the defects in the deposited membrane lead to a significantly reduced electrical resistance, which can be measured by an impedance spectroscopy (Sinner & Knoll, 2001). The wettability of membranes, reflecting the hydrophobicity of the membrane surface, is usually determined by contact angle measurements (Kwok & Neumann, 1999).

2.3 Nanoparticle-based targeted drug delivery

Some drugs, especially cancer chemotherapeutics (e.g. doxorubicin), have a high cytotoxicity (Takara et al., 2002). However, it is harmful to both tumor cells and normal tissue cells. Side effects are induced by distribution of the drugs into normal tissues. The side effects are a determinant factor that restricts the administered drug dose. Meanwhile, the distribution of a drug into normal tissues causes a low concentration of the drug in the target tissues, which leads to suboptimal therapeutic effects. (Allen & Cullis, 2004) Targeted delivery of the drug into specific tissues or even cells is therefore desired. Nanosized drug delivery systems are able to significantly modify the pharmacokinetics and improve drug delivery efficacy (Yliperttula & Urtti, 2009). Nanoparticles are expected to play an important role in the targeting of drugs to target tissues (e.g. tumors). High drug concentrations at the sites of diseased tissues and low systemic exposure of nanoparticles designed for drug delivery can be achieved by the enhanced permeation and retention (EPR) effect due to their small size (nano level) (Dinarvand et al., 2012). Additionally, the surface modification of nanoparticles by ligand attachment enables ligand-mediated targeted nanoparticles to further improve the specificity/selectivity of drug delivery.

Nanoparticles are particles which have at least one dimension in the nanometer (10^{-9} m) scale. The size of the nanoparticles varies from a few nm to several hundreds of nm depending on the application. Nanoparticle sizes are mainly dependent on two factors for drug delivery applications. Firstly, nanoparticles for tumor targeting should be able to pass through the fenestrations of the leaky cancer endothelium. Secondly, nanoparticles should be able to avoid the clearance by the reticuloendothelial system (RES). (Zhao et al., 2011) Based on these factors, nanoparticles for drug delivery often involves sizes < 200 nm. (Singh & Lillard, 2009) Nanoparticles are divided into two basic types: nanocapsules and nanospheres. Nanocapsules are vesicles where a drug is entrapped in a cavity surrounded by a membrane or incorporated in the membrane. In contrast, nanospheres are matrix systems in which the drug is physically and uniformly dispersed. (Singh & Lillard, 2009) Many materials have been used for constructing nanoparticle drug delivery systems, such as biologic materials (e.g. lipids, peptides, nucleic acids, polysaccharides and viruses), polymeric materials [e.g. poly (lactic acid), PLA and poly (ethylene glycol), PEG) and even inorganic materials (e.g. silicon, carbon, gold and silver) (Hughes, 2005). These different materials can be assembled into the different types of the nanoparticle systems. Up to date, many types of nanoparticle systems have been developed for drug delivery, including liposomes, micelles, polymer nanoparticles (e.g. poly (lactic-co-glycolic acid) copolymer, PLGA nanoparticle), dendrimers, nanocrystals, nucleic acid complexes, nanotubes (e.g. single-walled carbon nanotube), quantum dots etc. (Emerich & Thanos,

2007; Faraji & Wipf, 2009; Haley & Frenkel, 2008; Singh & Lillard, 2009; Yliperttula & Urtti, 2009). Through these nanoparticle drug delivery systems, the drugs (small molecules or macromolecules such as protein and DNA) have been targeted into tumors, cells, ocular tissues and brain (across the blood brain barrier). Among these nanoparticle drug delivery systems, the most popular and exciting is the liposome based drug delivery system (Torchilin, 2007). Several liposome based formulations for cancer treatment such as rubicin, doxorubicin, vincristine, lurtotecan and kanamycin have been approved for clinical applications or are under a clinical evaluation (Eliaz & Szoka, 2001; Lammers et al., 2008; Torchilin, 2007). From this point of view and because liposomes were used for the studies in this thesis, only liposome based drug delivery is discussed in more detail here.

2.3.1 Liposomes in drug delivery

Liposomes are closed spherical vesicles consisting mainly of lipids, which self-assemble into a bilayer encapsulating the aqueous interior core (Figure 7). The liposome size may be formulated from tens of nm to hundreds of nm based on the need. Liposomes have a self-assembled lipid bilayer structure, which resembles cellular membranes. Natural or synthetic lipids, such as phosphatidycholines (PC) and phosphatidylethanolamines (PE), can be used for preparing liposomes. Additionally, other components such as cholesterol are often utilized to stabilize the liposome structure. Unilamellar or multilamellar vesicles may be formed. The most widely used method for liposome preparation is to hydrate dried lipid films with a buffer and extrude the buffer through a polymer membrane with small pores (e.g. 100 nm). Liposomes can load either hydrophilic drugs into the aqueous core or hydrophobic drugs within the lipid bilayers. Liposomes have a relatively good biocompatibility, which is the main reason why they are the most investigated nanoparticle drug delivery system. Several liposome based formulations for cancer have been approved for clinical application, as mentioned above.

With intravenous administration, the liposomes are usually rapidly cleared by the reticuloendothelial system (RES) (e.g. liver and spleen) after opsonization (Haley & Frenkel, 2008). This restricts the therapeutic effect of liposome formulations. The rapid clearance is related to the non-inert surface properties of the liposomes. Surface modification with hydrophilic polymer can inhibit the formation of a protein coating on the liposome surface and thus help to avoid the clearance of the liposomes by the RES. Polyethylene glycol (PEG) is one of the most widely used polymers for modifying the liposome surface giving the liposomes a “stealth” feature. The stealth feature reduces recognition by the RES, and thereby prolongs the circulation time and promotes the accumulation of liposomes into the tumors (Drummond et al., 1999; Lammers, et al., 2008; Torchilin, 2005). A PEGylated liposome based doxorubicin formulation “Doxil” has been approved for clinical use by FDA (Lammers, et al., 2008).

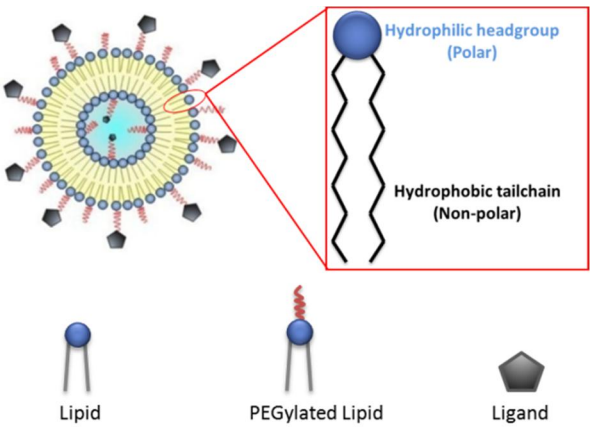

Figure 7. *Schematic illustration of the structure of a phospholipid and a liposome*

The targeting delivery in the approved liposome formulations is based on "passive targeting", where the size of the liposome is utilized to achieve the accumulation of liposomes in the target tissues. For example, the enhanced permeation and retention (EPR) effect in tumors enhances the extravasation of the liposomes from the systemic blood circulation, leading to accumulation of liposomes to the tumor tissues. In addition, ligands can be introduced on the liposome surface. These kinds of immunoliposomes are expected to enhance the targeting effect through the specific/selective interaction of the attached ligands with the cell surface receptors. This is called "active targeting". It is expected that active targeted liposomes that reaches the target tissues interacts specifically with the target cells. The liposomes are thereby bound to the cell surface and consequently internalized via endocytosis. In immunoliposomes, the internalization of the liposomes is achieved by ligand-mediated endocytosis. After that, the loaded drugs are released from the liposomes and a therapeutic action takes place. The drug release is achieved by diffusion through the lipid bilayers or breaking of the liposome structure. Therefore, the structure, stability and phase state of the lipid bilayers in the liposomes have significant effects on the drug release. A liquid crystalline phase in the lipid bilayer of a liposome is more advantageous for drug release compared with a lipid bilayer in a solid phase. The phase states of the lipid bilayers of the liposomes can easily be investigated by constructing planar lipid bilayers and characterizing the thin films by SPR and the Langmuir balance. In addition, macromolecular drugs like proteins or DNA do not easily diffuse across the densely packed lipid bilayers. Some measures should be taken in order to loosen the lipid bilayers or even to destroy the liposome structure to achieve efficient drug release. External stimulus such as pH, temperature, light, magnetic field and ultrasound can be utilized to trigger the drug release from liposomes.

2.3.2 Targeting of nanoparticles and interaction with cells

As described in the liposome part above, nanoparticles undergo transport, vasculature and tissue penetration, and cellular interactions after intravenous administration. During

the transportation, some nanoparticles may be cleared by the RES, whereas other nanoparticles will reach the target tissues (e.g. tumors). The targeting may be achieved by passive or active targeting. Passive targeting is based on the EPR effect, which allows substantial amount of nanoparticles to extravasate from the systemic circulation into the interstitial fluid in the tumor tissues. The specificity/selectivity in passive targeting is based on the size of the nanoparticles and is less efficient than active targeting. In contrast to passive targeting, active targeting relies on specific ligand-receptor interactions. The nanoparticle surface is modified by attaching ligands to form immunonanoparticles. The ligands of these immunonanoparticles act as homing devices which bind specifically to the receptors (over)expressed in the target tissues (e.g. tumors). Cellular internalization of immunonanoparticles is then achieved by receptor-mediated endocytosis.

Endocytosis is a process by which cells uptake nutrients or other molecules (e.g. proteins). Endocytosis is based on the formation of intracellular vesicles following the invagination of the plasma membrane, or the formation of larger vesicles induced by ruffling of the plasma membrane. (Iversen, et al., 2011) When nanoparticles with attached ligands are extracellularly bound to cellular membrane receptors, a signal to the intracellular space is transduced and triggers the cellular pathway of endocytosis.(Faraji & Wipf, 2009) Thus, receptor-mediated endocytosis enables a greater specificity/selectivity in cellular targeting compared to passive targeting.

DNA and RNA drugs must first be delivered into the cell, followed by transfer into the nucleus in order to have an effect. Therefore, the cellular internationalization of nanoparticles for DNA and RNA delivery, enabled by receptor-mediated endocytosis, is vital for the determination of their biological activity. The ligand-mediated targeting to target cells has several advantages, such as minimizing the toxicity and adverse effects, and overcoming multidrug resistance in cancer chemotherapy. Targeting the nanoparticles towards internalizing receptors has been utilized to facilitate efficient internalization in some tumor models (Fahmy et al., 2005; Park et al., 2002). However, cellular specific recognition enables also targeting to non-tumor tissues (Torchilin, 2007; Xu et al., 2013)

Once the nanoparticles reach the dense matrix surrounding the cells they have to first interact with the cell surface in order to initiate cellular internalization (Doane & Burda, 2012). The NP cell uptake rate and mechanism are dependent on both the cell-type and the physicochemical properties of the nanoparticles (size, shape, surface ligand density and arrangement, surface charge, and other surface properties). (Iversen, et al., 2011; Verma & Stellacci, 2010) The internalization of nanoparticles is also size dependent. Nanoparticles with a diameter of around 500 nm are internalized by nonphagocytic cells via an energy-dependent process, whereas smaller nanoparticles with < 200 nm diameter are internalized via clathrin-coated pits.(Fahmy, et al., 2005) In addition, the construction of a liposome with bio-inert surface by using PEG modification is vital for achieving long circulation times. Therefore, it is of utmost importance to pay attention to these factors during the design of nanoparticle drug delivery systems.

2.3.3 Non-labelled surface sensitive techniques with model membrane surfaces for studying interactions of liposomes

The interaction of nanoparticles with cells for optimizing the nanoparticles is usually studied by *in vitro* cell cultures or by *in vivo* animal tests. Both of these tests allow studies in conditions close to the biological environment in the body. Cell culture and animal tests are indispensable for studying nanoparticle drug delivery systems. However, the complex environment in cells and animals make quantitative studies of the targeting process of NP challenging (Doane & Burda, 2012). The interplay between different components and functions hampers to build a better understanding of the mechanism behind one specific biological process of interest. Thus, cell culture and animal tests are less powerful to quantitatively characterize a biological process at the molecular level. Cell culture tests are usually performed in well plates under static conditions, which do not reflect the effect of the blood flow *in vivo*. Animal tests are not suitable for massive screening at a primary stage of drug development due to ethical issues. In addition to cell culture and animal tests, biophysical detection techniques such as imaging and label-free detection techniques are rapidly becoming a necessity for building a thorough understanding of nanoparticle-cell interactions. Imaging is a good tool for visualizing the interaction processes. However, labeling is usually needed in living cell imaging by fluorescence microscopy. In contrast, non-labelled surface sensitive techniques allow for studying interfacial interaction events under simplified environments and well-controlled physicochemical conditions such as pH, temperature and flow rate/shear stress. The affinity and kinetics behind specific nanoparticle-cell interactions can be investigated at the molecular level by utilizing simplified surface model membranes.

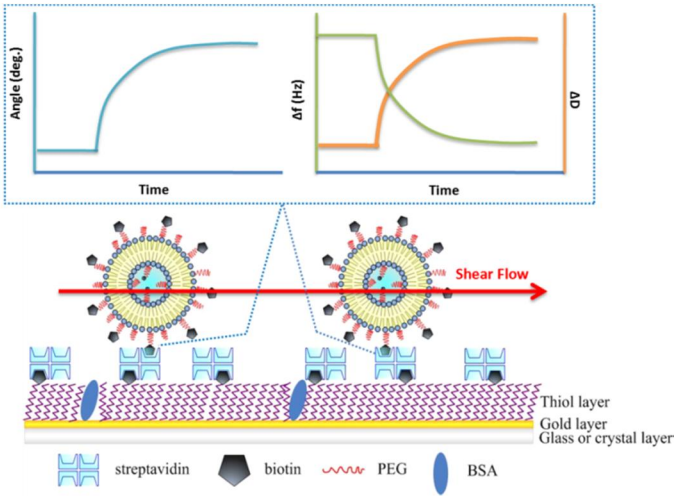

Figure 8. *Schematic illustration of the combined use of two non-labelled surface sensitive techniques (SPR and QCM) for studying the interactions of nanoparticle (liposome)-receptor model membranes (PEGylated thiol SAM).*

As discussed above, SPR and QCM are both surface sensitive techniques measuring the interaction events at the surface or at an interface in real-time without labels. However,

they are based on totally different detection principles. The combined use of SPR and QCM enable an in-depth insight of the interfacial interaction event. The affinity, kinetics and even the structure of the bound nanoparticle layer may be characterized under controlled shear flows by using simplified model membranes and the combined use of SPR and QCM (Figure 8).

References

Ahlers, M., Blankenburg, R., Grainger, D., Meller, P., Ringsdorf, H., & Salesse, C. (1989). Specific recognition and formation of two-dimensional streptavidin domains in monolayers: applications to molecular devices. *Thin Solid Films, 180*(1), 93-99.

Allen, T. M., & Cullis, P. R. (2004). Drug delivery systems: Entering the mainstream. *Science, 303*(5665), 1818-1822.

Allison, M. (2012). Reinventing clinical trials. *Nat Biotechnol, 30*(1), 41-49.

Andersson, O., Larsson, A., Ekblad, T., & Liedberg, B. (2008). Gradient Hydrogel Matrix for Microarray and Biosensor Applications: An Imaging SPR Study. *Biomacromolecules, 10*(1), 142-148.

Ansorena, P., Zuzuarregui, A., Pérez-Lorenzo, E., Mujika, M., & Arana, S. (2011). Comparative analysis of QCM and SPR techniques for the optimization of immobilization sequences. *Sensors and Actuators B: Chemical, 155*(2), 667-672.

Arnau, A. (2008). *Piezoelectric transducers and applications* (2nd ed.). New York: Springer.

Balasubramanian, K. K., Cammarata, V., & Wu, Q. (1995). Langmuir-Schaefer Films: Head Group Influence on Orientation of Substituted Styryl Bipyridines. *Langmuir, 11*(5), 1658-1665.

Bamberg, E., Butt, H.-J., Eisenrauch, A., & Fendler, K. (1993). Charge transport of ion pumps on lipid bilayer membranes. *Quarterly reviews of biophysics, 26*(01), 1-25.

Baumgart, T., & Offenhausser, A. (2003). Polysaccharide-supported planar bilayer lipid model membranes. *Langmuir, 19*(5), 1730-1737.

Binnig, G., Quate, C. F., & Gerber, C. (1986). Atomic Force Microscope. *Physical Review Letters, 56*(9), 930-933.

Blake, C., & Gould, B. J. (1984). Use of enzymes in immunoassay techniques. A review. *Analyst, 109*(5), 533-547.

Blodgett, K. B. (1934). Monomolecular films of fatty acids on glass. *Journal of the American Chemical Society, 56*(2), 495-495.

Blodgett, K. B. (1935). Films built by depositing successive monomolecular layers on a solid surface. *Journal of the American Chemical Society, 57*(6), 1007-1022.

Bohunicky, B., & Mousa, S. A. (2011). Biosensors: the new wave in cancer diagnosis. *Nanotechnology, Science and Applications, 4*, 1-10.

Boncheva, M., & Vogel, H. (1997). Formation of stable polypeptide monolayers at interfaces: Controlling molecular conformation and orientation. *Biophysical Journal, 73*(2), 1056-1072.

Boulbitch, A., Guttenberg, Z., & Sackmann, E. (2001). Kinetics of membrane adhesion mediated by ligand-receptor interaction studied with a biomimetic system. *Biophysical Journal, 81*(5), 2743-2751.

Buenger, D., Topuz, F., & Groll, J. (2012). Hydrogels in sensing applications. *Progress in Polymer Science, 37*(12), 1678-1719.

Caide, X., & Sui, S. F. (1999). Numerical simulations of surface plasmon resonance system for monitoring DNA hybridization and detecting protein lipid film interactions. *European Biophysics Journal With Biophysics Letters, 28*(2), 151-157.

Campanella, H. (2010). *Acoustic wave and electromechanical resonators : concept to key applications*. Norwood, MA.: Artech House.

Canovi, M., Lucchetti, J., Stravalaci, M., Re, F., Moscatelli, D., Bigini, P., et al. (2012). Applications of Surface Plasmon Resonance (SPR) for the Characterization of Nanoparticles Developed for Biomedical Purposes. *Sensors, 12*(12), 16420-16432.

Castellana, E. T., & Cremer, P. S. (2006). Solid supported lipid bilayers: From biophysical studies to sensor design. *Surface Science Reports, 61*(10), 429-444.

Charles, P. T., Taitt, C. R., Goldman, E. R., Rangasammy, J. G., & Stenger, D. A. (2004). Immobilization strategy and characterization of hydrogel-based thin films for interrogation of ligand binding with staphylococcal enterotoxin B (SEB) in a protein microarray format. *Langmuir, 20*(1), 270-272.

Che, A. F., Huang, X. J., & Xu, Z. K. (2010). Protein adsorption on a glycosylated polyacrylonitrile surface: monitoring with QCM and SPR. *Macromolecular bioscience, 10*(8), 955-962.

Cheng, C. I., Chang, Y.-P., & Chu, Y.-H. (2012). Biomolecular interactions and tools for their recognition: focus on the quartz crystal microbalance and its diverse surface chemistries and applications. *Chemical Society Reviews, 41*(5), 1947-1971.

Chung, M., Lowe, R. D., Chan, Y.-H. M., Ganesan, P. V., & Boxer, S. G. (2009). DNA-tethered membranes formed by giant vesicle rupture. *Journal of structural biology, 168*(1), 190-199.

Cohen, F. S., Zimmerberg, J., & Finkelstein, A. (1980). Fusion of phospholipid vesicles with planar phospholipid bilayer membranes. II. Incorporation of a vesicular membrane marker into the planar membrane. *The Journal of general physiology, 75*(3), 251-270.

Comley, J. (2008). Progress in the implementation of label-free detection part 2: binding analysis assays. *Drug Discovery World*(Fall), 28-47.

Cooper, M. (2009). *Label-free biosensors: techniques and applications*: Cambridge University Press.

Cooper, M. A. (2002). Optical biosensors in drug discovery. *Nature Rev. Drug Discov., 1*, 515-528.

Cooper, M. A., & Whalen, C. (2005). Profiling molecular interactions using label-free acoustic screening. *Drug Discovery Today: Technologies, 2*(3), 241-245.

Copeland, R. A., Pompliano, D. L., & Meek, T. D. (2006). Drug–target residence time and its implications for lead optimization. *Nature Reviews Drug Discovery, 5*(9), 730-739.

Corso, C. D. (2008). *Theoretical and experimental development of a ZnO-based laterally excited thickness shear mode acoustic wave immunosensor for cancer biomarker detection.* Georgia Institute of Technology.

Cunningham, B. T., Li, P., Schulz, S., Lin, B., Baird, C., Gerstenmaier, J., et al. (2004). Label-free assays on the BIND system. *Journal of Biomolecular Screening, 9*(6), 481-490.

Curie, J., & Curie, P. (1880). Développement, par pression, de l'électricité polaire dans les cristaux hémièdres à faces inclinées. *Comptes rendus de l'Académie des Sciences, 91*, 294-295.

Darsanaki, R. K., Azizzadeh, A., Nourbakhsh, M., Raeisi, G., & Aliabadi, M. A. (2013). Biosensors: Functions and Applications. *Journal of Biology, 2*(1), 53-61.

Datta, A. (2007). *Characterization of polyethylene glycol hydrogels for biomedical applications.* B.E. University of Pune, India.

Dinarvand, R., Cesar de Morais, P., & D'Emanuele, A. (2012). Nanoparticles for Targeted Delivery of Active Agents against Tumor Cells. *J Drug Deliv, 2012*, 528123.

Dluhy, R., Shanmukh, S., & Morita, S. I. (2006). The application of two-dimensional correlation spectroscopy to surface and interfacial analysis. *Surface and Interface Analysis, 38*(11), 1481-1496.

Doane, T., & Burda, C. (2012). Nanoparticle mediated non-covalent drug delivery. *Adv Drug Deliv Rev*.

Dorvel, B. R., Keizer, H. M., Fine, D., Vuorinen, J., Dodabalapur, A., & Duran, R. S. (2007). Formation of tethered bilayer lipid membranes on gold surfaces: QCM-Z and AFM study. *Langmuir, 23*(13), 7344-7355.

Drummond, D. C., Meyer, O., Hong, K. L., Kirpotin, D. B., & Papahadjopoulos, D. (1999). Optimizing liposomes for delivery of chemotherapeutic agents to solid tumors. *Pharmacological Reviews, 51*(4), 691-743.

Duan, Y. X., Liu, J., Sato, H., Zhang, J. M., Tsuji, H., Ozaki, Y., et al. (2006). Molecular weight dependence of the poly(L-lactide)/poly(D-lactide) stereocomplex at the air-water interface. *Biomacromolecules, 7*(10), 2728-2735.

Dynarowicz-Latka, P., Dhanabalan, A., & Oliveira, O. N., Jr. (2001). Modern physicochemical research on Langmuir monolayers. [Review]. *Adv Colloid Interface Sci, 91*(2), 221-293.

Eglen, R. M., Gilchrist, A., & Reisine, T. (2008). The use of immortalized cell lines in GPCR screening: the good, bad and ugly. *Combinatorial chemistry & high throughput screening, 11*(7), 560-565.

Ehrlich, P. (1913). Chemotherapeutics: scientific principles, methods and results. [10.1016/S0140-6736(01)38705-6]. *Lancet, 182*, 445-451.

Elender, G., Kuhner, M., & Sackmann, E. (1996). Functionalisation of Si/SiO2 and glass surfaces with ultrathin dextran films and deposition of lipid bilayers. *Biosensors & Bioelectronics, 11*(6-7), 565-577.

Eliaz, R., & Szoka, F. (2001). Liposome-encapsulated doxorubicin targeted to CD44: A strategy to kill CD44-overexpressing tumor cells. *Cancer Research*, 2592-2601.

Emerich, D. F., & Thanos, C. G. (2007). Targeted nanoparticle-based drug delivery and diagnosis. *Journal of Drug Targeting, 15*(3), 163-183.

Esterhouse, T. E., & Petrinos, L. B. (2009). *Protein Biosynthesis*: Nova Science.

Fahmy, T. M., Fong, P. M., Goyal, A., & Saltzman, W. M. (2005). Targeted for drug delivery. *Materials Today, 8*(8), 18-26.

Fan, X., White, I. M., Shopova, S. I., Zhu, H., Suter, J. D., & Sun, Y. (2008). Sensitive optical biosensors for unlabeled targets: A review. *Analytica Chimica Acta, 620*(1–2), 8-26.

Fang, Y. (2006). Label-free cell-based assays with optical biosensors in drug discovery. *Assay Drug Dev Technol, 4*(5), 583-595.

Fang, Y. (2012). Ligand-receptor interaction platforms and their applications for drug discovery. *Expert Opin Drug Discov, 7*(10), 969-988.

Fang, Y., Frutos, A. G., & Verklereen, R. (2008). Label-free cell-based assays for GPCR screening. *Combinatorial chemistry & high throughput screening, 11*(5), 357-369.

Faraji, A. H., & Wipf, P. (2009). Nanoparticles in cellular drug delivery. *Bioorganic & Medicinal Chemistry, 17*(8), 2950-2962.

Farokhzad, O. C., & Langer, R. (2009). Impact of nanotechnology on drug delivery. *Acs Nano, 3*(1), 16-20.

FDA. (2013). http://www.fda.gov/ohrms/dockets/ac/01/slides/3763s2_08_martin/tsld005.htm. Retrieved May, 2013

Frazier, R. A., Kooyman, R. P. H., Corn, R. M., Schasfoort, R. B. M., & Tudos, A. J. (2008). *Handbook of Surface Plasmon Resonance*: Royal Society of Chemistry.

Friedrich, M. G., Giess, F., Naumann, R., Knoll, W., Ataka, K., Heberle, J., et al. (2004). Active site structure and redox processes of cytochrome c oxidase immobilised in a novel biomimetic lipid membrane on an electrode. *Chemical Communications*(21), 2376-2377.

Giess, F., Friedrich, M. G., Heberle, J., Naumann, R. L., & Knoll, W. (2004). The Protein-Tethered Lipid Bilayer: A Novel Mimic of the Biological Membrane. *Biophysical Journal, 87*(5), 3213-3220.

Gliozzi, A., Relini, A., & Chong, P. L. G. (2002). Structure and permeability properties of biomimetic membranes of bolaform archaeal tetraether lipids. *Journal of Membrane Science, 206*(1-2), 131-147.

Gosling, J. P. (2000). *Immunoassays : a practical approach*. Oxford ; New York: Oxford University Press.

Grieshaber, D., MacKenzie, R., Voros, J., & Reimhult, E. (2008). Electrochemical biosensors - Sensor principles and architectures. *Sensors, 8*(3), 1400-1458.

Gyorvary, E., Wetzer, B., Sleytr, U. B., Sinner, A., Offenhausser, A., & Knoll, W. (1999). Lateral diffusion of lipids in silane-, dextran-, and S-layer-supported mono- and bilayers. *Langmuir, 15*(4), 1337-1347.

Halai, R., & Cooper, M. A. (2012). Using label-free screening technology to improve efficiency in drug discovery. *Expert Opinion on Drug Discovery, 7*(2), 123-131.

Haley, B., & Frenkel, E. (2008). Nanoparticles for drug delivery in cancer treatment. *Urologic Oncology-Seminars and Original Investigations, 26*(1), 57-64.

Hall, D. B., Underhill, P., & Torkelson, J. M. (2004). Spin coating of thin and ultrathin polymer films. *Polymer Engineering & Science, 38*(12), 2039-2045.

Hamidi, M., Azadi, A., & Rafiei, P. (2008). Hydrogel nanoparticles in drug delivery. *Advanced drug delivery reviews, 60*(15), 1638-1649.

Hankel, W. (1881). Über die Aktino- und piezoelektrischen Eigenschaften des Bergkrystalles und ihre Beziehung zu den thermoelektrischen Abh. *Sächs, 12*, 457–548.

Hansen, K. M., & Thundat, T. (2005). Microcantilever biosensors. *Methods, 37*(1), 57-64.

Homola, J., Yee, S. S., & Gauglitz, G. (1999). Surface plasmon resonance sensors: review. *Sensors and Actuators B: Chemical, 54*(1–2), 3-15.

Hong, S., Leroueil, P. R., Majoros, I. J., Orr, B. G., Baker, J. R., & Holl, M. M. B. (2007). The binding avidity of a nanoparticle-based multivalent targeted drug delivery platform. *Chemistry & Biology, 14*(1), 107-115.

Hopfner, M., Rothe, U., & Bendas, G. (2008). Biosensor-based evaluation of liposomal behavior in the target binding process. *Journal of Liposome Research*, 71-82.

Hughes, G. A. (2005). Nanostructure-mediated drug delivery. *Dm Disease-a-Month, 51*(6), 342-361.

Hunt, H. K., & Armani, A. M. (2010). Label-free biological and chemical sensors. *Nanoscale, 2*(9), 1544-1559.

Irvine, J. D., Takahashi, L., Lockhart, K., Cheong, J., Tolan, J. W., Selick, H. E., et al. (1999). MDCK (Madin-Darby canine kidney) cells: A tool for membrane permeability screening. *Journal of Pharmaceutical Sciences, 88*(1), 28-33.

Iversen, T. G., Skotland, T., & Sandvig, K. (2011). Endocytosis and intracellular transport of nanoparticles: Present knowledge and need for future studies. *Nano Today, 6*(2), 176-185.

Janshoff, A., Galla, H. J., & Steinem, C. (2000). Piezoelectric mass-sensing devices as biosensors - An alternative to optical biosensors? *Angewandte Chemie-International Edition, 39*(22), 4004-4032.

Junghans, A., & Koper, I. (2010). Structural Analysis of Tethered Bilayer Lipid Membranes. *Langmuir, 26*(13), 11035-11040.

Kalb, E., Frey, S., & Tamm, L. K. (1992). Formation of supported planar bilayers by fusion of vesicles to supported phospholipid monolayers. *Biochimica et Biophysica Acta (BBA)-Biomembranes, 1103*(2), 307-316.

Kanazawa, K. K., & Gordon, J. G. (1985). Frequency of a quartz microbalance in contact with liquid. *Analytical Chemistry, 57*(8), 1770-1771.

Keller, C. A., & Kasemo, B. (1998). Surface Specific Kinetics of Lipid Vesicle Adsorption Measured with a Quartz Crystal Microbalance. *Biophysical Journal, 75*(3), 1397-1402.

Kibrom, A., Roskamp, R. F., Jonas, U., Menges, B., Knoll, W., Paulsen, H., et al. (2010). Hydrogel-supported protein-tethered bilayer lipid membranes: a new approach toward polymer-supported lipid membranes. *Soft Matter, 7*(1), 237-246.

Kim, J.-H., & Randall Lee, T. (2006). Discrete thermally responsive hydrogel-coated gold nanoparticles for use as drug-delivery vehicles. *Drug Development Research, 67*(1), 61-69.

Kim, J., Kim, S., Ohashi, T., Muramatsu, H., Chang, S.-M., & Kim, W.-S. (2010). Construction of simultaneous SPR and QCM sensing platform. *Bioprocess and Biosystems Engineering, 33*(1), 39-45.

Kling, J. (2011). Fresh from the biologic pipeline-2010. *Nat Biotechnol, 29*(3), 197-200.

Knoll, W., Köper, I., Naumann, R., & Sinner, E.-K. (2008). Tethered bimolecular lipid membranes—A novel model membrane platform. *Electrochimica Acta, 53*(23), 6680-6689.

Kocbek, P., Obermajer, N., Cegnar, M., Kos, J., & Kristl, J. (2007). Targeting cancer cells using PLGA nanoparticles surface modified with monoclonal antibody. *Journal of Controlled Release, 120*(1-2), 18-26.

Koh, W.-G., Itle, L. J., & Pishko, M. V. (2003). Molding of hydrogel microstructures to create multiphenotype cell microarrays. *Analytical chemistry, 75*(21), 5783-5789.

Koh, W.-G., & Pishko, M. V. (2006). Fabrication of cell-containing hydrogel microstructures inside microfluidic devices that can be used as cell-based biosensors. *Analytical and bioanalytical chemistry, 385*(8), 1389-1397.

Kwok, D. Y., & Neumann, A. W. (1999). Contact angle measurement and contact angle interpretation. *Advances in Colloid and Interface Science, 81*(3), 167-249.

Lammers, T., Hennink, W. E., & Storm, G. (2008). Tumour-targeted nanomedicines: principles and practice. *British Journal of Cancer, 99*(3), 392-397.

Langmuir, I. (1920). The mechanism of the surface phenomena of flotation. *Transactions of the Faraday Society, 15*(June), 62-74.

Laricchia-Robbio, L., & Revoltella, R. P. (2004). Comparison between the surface plasmon resonance (SPR) and the quartz crystal microbalance (QCM) method in a structural analysis of human endothelin-1. *Biosensors and Bioelectronics, 19*(12), 1753-1758.

Lee, D., & Lee, S. (1996). Electric‐field measurement near a ring antenna by a new field sensor using piezoelectric resonance. *Review of scientific instruments, 67*(9), 3320-3324.

Li, G., Ferrie, A. M., & Fang, Y. (2006). Label-free profiling of ligands for endogenous GPCRs using a cell-based high-throughput screening technology. *Journal of the Association for Laboratory Automation, 11*(4), 181-187.

Li, L. Y., Chen, S. F., & Jiang, S. Y. (2007). Protein interactions with oligo(ethylene glycol) (OEG) self-assembled monolayers: OEG stability, surface packing density and protein adsorption. *Journal of Biomaterials Science-Polymer Edition, 18*(11), 1415-1427.

Liang, H. (2010). *SPR and QCM Technology for the Research of Binding Behavior of Targeted Nanoparticulate to Surface.* Chongqing University, Chongqing.

Liang, H., Miranto, H., Granqvist, N., Sadowski, J. W., Viitala, T., Wang, B., et al. (2010). Surface plasmon resonance instrument as a refractometer for liquids and ultrathin films. *Sensors and Actuators B: Chemical, 149*(1), 212-220.

Lofas, S., & Johnsson, B. (1990). A Novel Hydrogel Matrix on Gold Surfaces in Surface-Plasmon Resonance Sensors for Fast and Efficient Covalent Immobilization of Ligands. *Journal of the Chemical Society-Chemical Communications*(21), 1526-1528.

Loidl-Stahlhofen, A., Eckert, A., Hartmann, T., & Schottner, M. (2001). Solid-supported lipid membranes as a tool for determination of membrane affinity: High-throughput screening of a physicochemical parameter. *Journal of Pharmaceutical Sciences, 90*(5), 599-606.

Majewski, J., Wong, J. Y., Park, C. K., Seitz, M., Israelachvili, J. N., & Smith, G. S. (1998). Structural studies of polymer-cushioned lipid bilayers. *Biophysical Journal, 75*(5), 2363-2367.

Malmström, J., Agheli, H., Kingshott, P., & Sutherland, D. S. (2007). Viscoelastic Modeling of Highly Hydrated Laminin Layers at Homogeneous and Nanostructured Surfaces: Quantification of Protein Layer Properties Using QCM-D and SPR. *Langmuir, 23*(19), 9760-9768.

Mao, C., & Kisaalita, W. S. (2004). Characterization of 3-D collagen hydrogels for functional cell-based biosensing. *Biosensors and Bioelectronics, 19*(9), 1075-1088.

Marks, R. S., Cullen, D. C., Karube, I., Lowe, C. R., & Weetall, H. H. (2007). *Handbook of biosensors and biochips* (Vol. 1): John Wiley & Sons.

Martin, D. K. (2007). *Nanobiotechnology of biomimetic membranes*. New York: Springer.

Mateescu, A., Wang, Y., Dostalek, J., & Jonas, U. (2012). Thin Hydrogel Films for Optical Biosensor Applications. *Membranes, 2*(1), 40-69.

Mc Cabe, I. P., & Forstner, M. B. (2013). Polymer Supported Lipid Bialyers.

Mendelsohn, R., Mao, G. R., & Flach, C. R. (2010). Infrared reflection-absorption spectroscopy: Principles and applications to lipid-protein interaction in Langmuir films. *Biochimica Et Biophysica Acta-Biomembranes, 1798*(4), 788-800.

Mennicke, U., & Salditt, T. (2002). Preparation of solid-supported lipid bilayers by spin-coating. *Langmuir, 18*(21), 8172-8177.

Metselaar, J. M., Mastrobattista, E., & Storm, G. (2002). Liposomes for intravenous drug targeting: design and applications. *Mini Reviews in Medicinal Chemistry, 2*(4), 319-329.

Mizuguchi, T., Uchimura, H., Kataoka, H., Akaji, K., Kiso, Y., & Saito, K. (2012). Intact-cell-based surface plasmon resonance measurements for ligand affinity evaluation of a membrane receptor. *Analytical Biochemistry, 420*(2), 185-187.

Mohanty, S. P., & Kougianos, E. (2006). Biosensors: a tutorial review. *Potentials, IEEE, 25*(2), 35-40.

Mohwald, H. (1990). Phospholipid and phospholipid-protein monolayers at the air/water interface. *Annual review of physical chemistry, 41*(1), 441-476.

Monošík, R., Streďanský, M., & Šturdík, E. (2012). Biosensors-classification, characterization and new trends. *Acta Chimica Slovaca, 5*(1), 109-120.

Montal, M., & Mueller, P. (1972). Formation of bimolecular membranes from lipid monolayers and a study of their electrical properties. *Proceedings of the National Academy of Sciences, 69*(12), 3561-3566.

Morigaki, K., & Tawa, K. (2006). Vesicle Fusion Studied by Surface Plasmon Resonance and Surface Plasmon Fluorescence Spectroscopy. *Biophysical Journal, 91*(4), 1380-1387.

Mueller, P., Rudin, D. O., Ti Tien, H., & Wescott, W. C. (1962). Reconstitution of cell membrane structure in vitro and its transformation into an excitable system. *Nature, 194*, 979-980.

Mullard, A. (2013). 2012 FDA drug approvals. *Nat Rev Drug Discov, 12*(2), 87-90.

Nelson, K. E., Gamble, L., Jung, L. S., Boeckl, M. S., Naeemi, E., Golledge, S. L., et al. (2001). Surface characterization of mixed self-assembled monolayers designed for streptavidin immobilization. *Langmuir, 17*(9), 2807-2816.

Nuzzo, R. G., & Allara, D. L. (1983). Adsorption of bifunctional organic disulfides on gold surfaces. *Journal of the American Chemical Society, 105*(13), 4481-4483.

O'Connor, S. M., Andreadis, J. D., Shaffer, K. M., Ma, W., Pancrazio, J. J., & Stenger, D. A. (2000). Immobilization of neural cells in three-dimensional matrices for biosensor applications. *Biosensors and Bioelectronics, 14*(10), 871-881.

O'sullivan, C., & Guilbault, G. (1999). Commercial quartz crystal microbalances–theory and applications. *Biosensors and Bioelectronics, 14*(8), 663-670.

Oh, S. J., Hong, B. J., Choi, K. Y., & Park, J. W. (2006). Surface modification for DNA and protein microarrays. *Omics-a Journal of Integrative Biology, 10*(3), 327-343.

Orive, G., De Castro, M., Kong, H. J., Hernandez, R., Ponce, S., Mooney, D. J., et al. (2009). Bioactive cell-hydrogel microcapsules for cell-based drug delivery. *Journal of Controlled Release, 135*(3), 203-210.

Ozkumur, E., Needham, J. W., Bergstein, D. A., Gonzalez, R., Cabodi, M., Gershoni, J. M., et al. (2008). Label-free and dynamic detection of biomolecular interactions for high-throughput microarray applications. *Proceedings of the National Academy of Sciences of the United States of America, 105*(23), 7988-7992.

Paasonen, L. (2010). *External signal-activated liposomal drug delivery systems.* University of Helsinki, Helsinki.

Park, J. W., Hong, K., Kirpotin, D. B., Colbern, G., Shalaby, R., Baselga, J., et al. (2002). Anti-HER2 immunoliposomes: enhanced efficacy attributable to targeted delivery. *Clin Cancer Res, 8*(4), 1172-1181.

Patel, A. R., & Frank, C. W. (2006). Quantitative analysis of tethered vesicle assemblies by quartz crystal microbalance with dissipation monitoring: binding dynamics and bound water content. *Langmuir, 22*(18), 7587-7599.

Patil, Y. B., Toti, U. S., Khdair, A., Ma, L., & Panyam, J. (2009). Single-step surface functionalization of polymeric nanoparticles for targeted drug delivery. *Biomaterials, 30*(5), 859-866.

Plant, A. L. (1999). Supported hybrid bilayer membranes as rugged cell membrane mimics. *Langmuir, 15*(15), 5128-5135.

Plunkett, M. A., Wang, Z., Rutland, M. W., & Johannsmann, D. (2003). Adsorption of pNIPAM Layers on Hydrophobic Gold Surfaces, Measured in Situ by QCM and SPR. *Langmuir, 19*(17), 6837-6844.

Qavi, A. J., Washburn, A. L., Byeon, J. Y., & Bailey, R. C. (2009). Label-free technologies for quantitative multiparameter biological analysis. *Analytical and Bioanalytical Chemistry, 394*(1), 121-135.

Ray, S., Mehta, G., & Srivastava, S. (2010). Label-free detection techniques for protein microarrays: Prospects, merits and challenges. *Proteomics, 10*(4), 731-748.

Reimhult, E., Höök, F., & Kasemo, B. (2003). Intact vesicle adsorption and supported biomembrane formation from vesicles in solution: influence of surface chemistry, vesicle size, temperature, and osmotic pressure. *Langmuir, 19*(5), 1681-1691.

Reimhult, E., Larsson, C., Kasemo, B., & Höök, F. (2004). Simultaneous Surface Plasmon Resonance and Quartz Crystal Microbalance with Dissipation Monitoring Measurements of Biomolecular Adsorption Events Involving Structural Transformations and Variations in Coupled Water. *Analytical Chemistry, 76*(24), 7211-7220.

Renaud, J. P., & Delsuc, M. A. (2009). Biophysical techniques for ligand screening and drug design. *Current Opinion in Pharmacology, 9*(5), 622-628.

Ricklin, D. (2005). *Surface Plasmon Resonance Applications in Drug Discovery: With an Emphasis on Small Molecule and Low Affinity Systems.* Unpublished PhD Thesis, University of Basel.

Ries, R. S., Choi, H., Blunck, R., Bezanilla, F., & Heath, J. R. (2004). Black lipid membranes: visualizing the structure, dynamics, and substrate dependence of membranes. *The Journal of Physical Chemistry B, 108*(41), 16040-16049.

Roberts, G. G. (1990). *Langmuir-Blodgett films*. New York Plenum Press.

Rossi, C., & Chopineau, J. (2007). Biomimetic tethered lipid membranes designed for membrane-protein interaction studies. *European Biophysics Journal With Biophysics Letters, 36*(8), 955-965.

Sauerbrey, G. (1959). Verwendung von schwingquarzen zur wägung dünner schichten und zur mikrowägung. *Z. Phys., 155*, 206-222.

Scannell, J. W., Blanckley, A., Boldon, H., & Warrington, B. (2012). Diagnosing the decline in pharmaceutical R&D efficiency. *Nat Rev Drug Discov, 11*(3), 191-200.

Schloßmacher, U., Schröder, H. C., Wang, X., Feng, Q., Diehl-Seifert, B., Neumann, S., et al. (2013). Alginate/silica composite hydrogel as a potential morphogenetically active scaffold for three-dimensional tissue engineering. *RSC Adv.*

Schreiber, F. (2004). Self-assembled monolayers: from simple model systems to biofunctionalized interfaces. *Journal of Physics: Condensed Matter, 16*(28), R881-R900.

Schwartz, D. K. (1997). Langmuir-Blodgett film structure. *Surface Science Reports, 27*(7–8), 245-334.

Scott, C. W., & Peters, M. F. (2010). Label-free whole-cell assays: expanding the scope of GPCR screening. *Drug Discovery Today, 15*(17-18), 704-716.

Scriven, L. (1988). *Physics and applications of dip coating and spin coating*. Paper presented at the MRS Proceedings.

Sean X. Liu, J.-T. K. (2009). Application of Kevin—Voigt Model in Quantifying Whey Protein Adsorption on Polyethersulfone Using QCM-D. *Journal of Laboratory Automation, 14*(4), 213-220.

Setaka, M., Yamamoto, T., Sato, N., Yano, M., & Kwan, T. (1982). A Stable Planar Bilayer-Membrane of Phospholipid Supported by Cellulose Sheets. *Journal of Biochemistry, 91*(1), 79-85.

Shah, P., Jogani, V., Bagchi, T., & Misra, A. (2008). Role of Caco-2 Cell Monolayers in Prediction of Intestinal Drug Absorption. *Biotechnology progress, 22*(1), 186-198.

Sherwin, J. A. (2011). *Langmuir monolayers in thin film technology*. New York: Nova Science Publishers.

Shiau, A. K., Massari, M. E., & Ozbal, C. C. (2008). Back to basics: Label-free technologies for small molecule screening. *Combinatorial Chemistry & High Throughput Screening, 11*(3), 231-237.

Singer, S., & Nicolson, G. (1972). The fluid mosaic model of the structure of cell membranes. *Science, 175*(4023), 720.

Singh, R., & Lillard, J. W. (2009). Nanoparticle-based targeted drug delivery. *Experimental and Molecular Pathology, 86*(3), 215-223.

Sinner, E.-K., & Knoll, W. (2001). Functional tethered membranes. *Current opinion in chemical biology, 5*(6), 705-711.

Su, X., Chew, F. T., & Li, S. F. Y. (2000). Design and application of piezoelectric quartz crystal-based immunoassay. *Analytical Sciences, 16*(2), 107-114.

Takara, K., Sakaeda, T., Yagami, T., Kobayashi, H., Ohmoto, N., Horinouchi, M., et al. (2002). Cytotoxic effects of 27 anticancer drugs in HeLa and MDR1-overexpressing derivative cell lines. *Biological & Pharmaceutical Bulletin, 25*(6), 771-778.

Tamm, L. K., & Mcconnell, H. M. (1985). Supported Phospholipid-Bilayers. *Biophysical Journal, 47*(1), 105-113.

Tanaka, M., & Sackmann, E. (2005). Polymer-supported membranes as models of the cell surface. *Nature, 437*(7059), 656-663.

Tang, Y., Mernaugh, R., & Zeng, X. (2006). Nonregeneration Protocol for Surface Plasmon Resonance: Study of High-Affinity Interaction with High-Density Biosensors. *Analytical Chemistry, 78*(6), 1841-1848.

Thevenot, D. R., Toth, K., Durst, R. A., & Wilson, G. S. (2001). Electrochemical biosensors: recommended definitions and classification. *Biosensors & Bioelectronics, 16*(1-2), 121-131.

Thompson, M., Kipling, A. L., Duncanhewitt, W. C., Rajakovic, L. V., & Cavicvlasak, B. A. (1991). Thickness-Shear-Mode Acoustic-Wave Sensors in the Liquid-Phase - a Review. *Analyst, 116*(9), 881-890.

Tien, H., & Ottova-Leitmannova, A. (2000). *Membrane Biophysics as viewed from Experiemental Bilayer Lipid Membraness*: Amsterdam, New York: Elsevier.

Tonova, D., Depas, M., & Vanhellemont, J. (1996). Interpretation of spectroscopic ellipsometry measurements of ultrathin dielectric layers on silicon: Impact of accuracy of the silicon optical constants. *Thin Solid Films, 288*(1-2), 64-68.

Torchilin, V. P. (2005). Recent advances with liposomes as pharmaceutical carriers. *Nature Reviews Drug Discovery, 4*(2), 145-160.
Torchilin, V. P. (2007). Targeted pharmaceutical nanocarriers for cancer therapy and Imaging. *Aaps Journal, 9*(2), E128-E147.
Tredgold, R. H. (1994). *Order in thin organic films*. Cambridge England ; New York: Cambridge University Press.
Turiel, J. G. (2005). *Polymer thin films : transport phenomena and surface forces.* Universiteit van Amsterdam
Van Emon, J. M. (2007). *Immunoassay and other bioanalytical techniques*. Boca Raton: CRC Press/Taylor & Francis.
Verma, A., & Stellacci, F. (2010). Effect of surface properties on nanoparticle-cell interactions. *Small, 6*(1), 12-21.
Vermonden, T., Censi, R., & Hennink, W. E. (2012). Hydrogels for Protein Delivery. *Chemical Reviews, 112*(5), 2853-2888.
Viitala, T., Hautala, J. T., Vuorinen, J., & Wiedmer, S. K. (2007). Structure of anionic phospholipid coatings on silica by dissipative quartz crystal microbalance. *Langmuir, 23*(2), 609-618.
Vo-Dinh, T., & Cullum, B. (2000). Biosensors and biochips: advances in biological and medical diagnostics. *Fresenius Journal of Analytical Chemistry, 366*(6-7), 540-551.
Vogt, B. D., Lin, E. K., Wu, W. L., & White, C. C. (2004). Effect of film thickness on the validity of the Sauerbrey equation for hydrated polyelectrolyte films. *Journal of Physical Chemistry B, 108*(34), 12685-12690.
Vollmer, F., & Arnold, S. (2008). Whispering-gallery-mode biosensing: label-free detection down to single molecules. *Nature Methods, 5*(7), 591-596.
Wagner, M. L., & Tamm, L. K. (2000). Tethered polymer-supported planar lipid bilayers for reconstitution of integral membrane proteins: silane-polyethyleneglycol-lipid as a cushion and covalent linker. *Biophysical Journal, 79*(3), 1400-1414.
Wang, D., Li, Y., Zhang, Y., Liu, Y., & Shi, G. (2012). High Throughput Screening (HTS) in Identification New Ligands and Drugable Targets of G Protein-Coupled Receptors (GPCRs). *Combinatorial Chemistry & High Throughput Screening, 15*(3), 232-241.
Watkins, E. B., El-Khouri, R. J., Miller, C. E., Seaby, B. G., Majewski, J., Marques, C. M., et al. (2011). Structure and Thermodynamics of Lipid Bilayers on Polyethylene Glycol Cushions: Fact and Fiction of PEG Cushioned Membranes. *Langmuir, 27*(22), 13618-13628.
Wilson, A. (2009). Handbook of Chemical and Biological Sensors. *Physiological Measurement, 17*(4), 319.
Winterhalter, M. (2000). Black lipid membranes. *Current Opinion in Colloid & Interface Science, 5*(3-4), 250-255.
Xi, B., Yu, N., Wang, X., Xu, X., & Abassi, Y. (2008). The application of cell-based label-free technology in drug discovery. *Biotechnology journal, 3*(4), 484-495.
Xu, F., Persson, B., Löfås, S., & Knoll, W. (2006). Surface plasmon optical studies of carboxymethyl dextran brushes versus networks. *Langmuir, 22*(7), 3352-3357.
Xu, S., Olenyuk, B. Z., Okamoto, C. T., & Hamm-Alvarez, S. F. (2013). Targeting receptor-mediated endocytotic pathways with nanoparticles: Rationale and advances. *Adv Drug Deliv Rev, 65*(1), 121-138.

Yang, Z., Gu, H., Fu, D., Gao, P., Lam, J. K., & Xu, B. (2004). Enzymatic formation of supramolecular hydrogels. *Advanced Materials, 16*(16), 1440-1444.

Yliperttula, M., & Urtti, A. (2009). Nanotechnology for Improved Drug Bioavailability. *Drug Bioavailability: Estimation of Solubility, Permeability, Absorption and Bioavailability, Volume 40, Second Edition*, 597-611.

Yu, X. B., Xu, D. K., & Cheng, Q. (2006). Label-free detection methods for protein microarrays. *Proteomics, 6*(20), 5493-5503.

Zhang, Y., Chen, Y., Ding, Z., Wang, C., Huang, H., & Jin, G. (2010). *Chitosan cushioned air stable single PEGylated phospholipid bilayers*. Paper presented at the World Congress on Medical Physics and Biomedical Engineering, September 7-12, 2009, Munich, Germany.

Zhao, L., Ye, Y., Li, J., & Wei, Y. (2011). Preparation and the in-vivo evaluation of paclitaxel liposomes for lung targeting delivery in dogs. *Journal of Pharmacy and Pharmacology*, 80-86.

Zribi, A., & Fortin, J. B. (2009). *Functional Thin Films and Nanostructures for Sensors: Synthesis, Physics and Applications*: Springer London, Limited.

3 AIMS OF THE STUDY

The general objective of this thesis was to develop non-labelled surface sensitive techniques (SPR and QCM) as platforms for pharmaceutical nanotechnology research. The emphasis was on developing and optimizing and further utilizing SPR and QCM based platforms for quantitatively characterizing the interaction of targeted nanoparticles with a target receptor surface. The methodologies for simultaneously characterizing multiple parameters of thin and thick films (sub-nm to hundreds of nm) with multi-parametric SPR (MP-SPR) were also developed.

The specific aims were:

1. To improve, optimize and evaluate a Kretschmann configuration MP-SPR prototype. To develop the approaches for simultaneous and unambiguous determination of both the refractive index and the thickness of thin films utilizing two-wavelength SPR. (I)
2. To develop methodologies for characterizing ultrathin and thick organic layers (sub-nm to hundreds of nm) by surface plasmon resonance multi-wavelength and waveguide mode analysis. (II)
3. To optimize and synchronize the hydrodynamics conditions in the flow channels of SPR and QCM devices through computational fluid dynamic (CFD) modeling for surface interaction studies. (III)
4. To develop a methodology for quantitatively characterizing targeted nanoparticle interactions with receptor model surfaces by using the synchronized SPR and QCM devices. (IV)

4 SURFACE PLASMON RESONANCE INSTRUMENT AS A REFRACTOMETER FOR LIQUIDS AND ULTRATHIN FILMS*

Abstract:

A surface plasmon resonance (SPR) setup in Kretschmann configuration is being utilized as a refractometer for both liquids as well as ultrathin films. The setup is based on a goniometer approach providing a wide angular scan range which facilitates highly accurate liquid and gas phase measurements. Attention was paid to improve sample handling and preparation. In order to avoid cross-contamination between measurements, an easily removable and exchangeable molded PDMS flow cell was used during the measurements. By careful choice of components for liquid handling the dead volume of the system could be reduced down to some microliters.

The angular change and thus the refractive index for sucrose, ethylene glycol (EG) and ethanol solutions with different concentrations, the thickness and refractive index of deposited Langmuir-Blodgett (LB) films, and the interaction kinetics between a biotin containing self-assembled monolayer (SAM) and streptavidin were determined. The measured refractive indices of sucrose, EG and ethanol solutions corresponded well with literature values. LB films were characterized by measuring the complete SPR curve in an angular scan range from 40 to 78°. A two-color SPR approach combined with two-medium measurements was successfully employed for simultaneous and unambiguous determination of both refractive index and thickness of stearic acid LB monolayers. The thickness obtained for the stearic acid monolayer was 2.66 nm, and the refractive indices at 635 and 670 nm were 1.5800 and 1.4138, respectively. The developed sensor-plate holder enabled functionalization of the SPR gold chip outside the instrument, therefore making the sample handling more flexible. The affinity constant obtained for the streptavidin-biotin interaction was 1.01×10^8 M^{-1}. The total angle SPR method used in this study clearly shows its potential to be used as a refractometer for both liquids and ultrathin films, as well as for traditional liquid phase biomolecular kinetic studies.

*Adapted from (Reprinted with permission from Elsevier): Huamin Liang, Heini Miranto, Niko Granqvist, Janusz W. Sadowski, Tapani Viitala, Bochu Wang, Marjo Yliperttula: Surface plasmon resonance instrument as a refractometer for liquids and ultrathin films. Sensors and Actuators B: Chemical 149: 212-220, 2010.

4.1 Introduction

Surface plasmon resonance (SPR) is a charge-density oscillation that may occur at the interface of two media with dielectric constants of opposite signs such as a metal (typically gold and silver with negative dielectric constants) and a dielectric medium (e.g. air and water with positive dielectric constants) (Homola et al., 1999). The analytical technique based on SPR is a powerful method used to detect changes in the refractive index of the adjacent medium next to a metal (Shumaker-Parry & Campbell, 2004). Due to its many advantages, for example high sensitivity, real-time monitoring, label-free detection etc., SPR has merely established itself as a powerful technique for a variety of liquid phase chemical and biological sensor applications such as bimolecular interactions (Critchley et al., 2004; Ito et al., 2007; Lin et al., 2007; Malmsten, 1999), quantitative measurements (Masson et al., 2007; Taylor et al., 2008), and membrane studies (Boncheva & Vogel, 1997; Du & Wang, 2007; Fitrilawati et al., 2005; Hanken et al., 1997).

Liquid phase SPR applications often rely on measuring relative changes in angular position or reflection intensities. In most cases found in the literature, the sensitivity of the surface plasmon resonance signal is measured as the interaction kinetics, either as a binding (association) or a dissociation between the molecules and the proteins on the surface, with an angular range limited to a few degrees only. Although the SPR phenomenon provides the means for real-time interaction studies, it also allows a more thorough optical characterization of liquids and (ultra)thin films provided that the SPR device and the SPR measurements are properly designed. A complete SPR curve holds all the necessary information to extract the refractive index and the thickness of adsorbed layers on a metal surface (gold being the most used due to its inertness). However, as the SPR curve is a product of thickness d and the real and the imaginary part of the refractive index $\tilde{n}$ ($d*\tilde{n}$), it is often necessary to assume or know either of them in order to extract the other. By simultaneously measuring surface plasmon resonance curves in different media with known properties it is possible to gain additional information for solving this problem. For plain liquids the situation is simpler as a liquid is infinitely thick and, therefore, it is possible to fit the refractive index of the solutions by using known concentrations of the solution.

The optical characterization of ultrathin films (e.g. phospholipid Langmuir-Blodgett mono- and multilayers) by SPR is not very common due to a lack of commercial instruments capable of measuring full SPR curves in a wide angular range. Although ellipsometers are widely used and have established themselves as techniques for thin film thickness and optical constants determinations they suffer from time consuming measurements, which often leads to examination of steady-state systems (Striebel et al., 1994). SPR allows time-resolved monitoring of dynamic processes and is therefore also an attractive alternative method for ultrathin film characterization, especially if it provides absolute angular information, a wide angular scan range and the use of different media or two laser wavelengths enabling unambiguous determination of layer thickness and refractive index. Another difficulty in SPR measurements has been the sample preparation, more specifically how to actually prepare the sample surface coatings of interest. Often, the substrate sample coatings are fixed and provided by a supplier or supposed to be

prepared inside the instrument. This is not so flexible that user specific surfaces could be functionalized and prepared outside the instrument. Moreover, the possibility to functionalize user specific surfaces outside the instrument allows a step by step characterization of each functionalization step from a clean surface to a completely functionalized surface.

Here we utilize an SPR instrument with goniometer based detection for a thorough optical characterization of liquids as well as ultrathin films. In the goniometer based SPR both the laser and photodetector are moved and linked together enabling a wide angular scan range covering both air and liquid phase ranges in the same mechanical setup. A custom modification of the goniometer based SPR detection technology to include two lasers with two different wavelengths provided us with a solution for unambiguous determination of both refractive index and thickness of ultrathin layers.

In order to simplify sample preparation for SPR measurements and make it more flexible, traceable chips and chip holders were developed and utilized to coat the substrates both inside and outside the instrument. Wide angular scan ranges and user specific sample coatings prepared outside the instrument are not yet so commonly used when it comes to SPR measurements. Therefore, our aim is to demonstrate the feasibility of the present and custom modified goniometer based SPR detection, and improved sample handling with a number of measurement examples including the following: (1) sucrose solutions with concentrations ranging from 5 to 300 mM, (2) a series of ethylene glycol (EG) solutions with concentrations up to 2 wt%, (3) a series of ethanol solutions with concentrations up to 5 wt%, (4) stearic acid mono- and multilayered Langmuir–Blodgett (LB) films, (5) nonspecific interaction of 0.5 mg/ml BSA with SAM and (6) biotin containing SAM interacting with an increasing concentration of streptavidin (1.25–20 nM). All the measurements were performed utilizing a dual channel flow cell with one laser wavelength enabling background noise subtraction, except in the case of the two-wavelength approach for LB film characterization where each channel was equipped with different wavelength lasers.

4.2 Experimental

4.2.1 Instrumentation

Principle of the signal detection: We used a standard and custom modified BioNavis SPR Navi^{TM} 200 instrument (www.bionavis.com) for signal detection. The equipment includes the light source, prism, detector and signal analysis software as well as the pump for liquid handling and the flow cell with the Kretschmann prism configuration (Fig. 1).

A glass slide with a sputtered gold layer (50 nm of Au on 2 nm of Cr) on one side together with the flow cell is pressed against the prism coated with an index matching elastomer in order to ensure continuous proceeding of the light. The laser beam is p-polarized by a polarizer before entering the prism, i.e. its electric field vector is parallel to

the plane of incidence, defined by the incident beam and a vector perpendicular the reflecting surface. After propagating into the prism, the light is reflected at the interface of glass and gold (more precisely at the glass/dielectric media interface covered by a thin gold film), due to a higher incident angle than the critical angle of the total internal reflection. The intensity changes of the reflected beam can be monitored as a function of the angle of incidence with the detector and analyzed by the signal analyzing software. During the measurements buffer is pumped through the flow cell with a peristaltic pump. Liquid flowing in the channel is in direct contact with the gold surface of the SPR slide. The sample that includes biomolecules, for instance, is injected by an injector valve into the buffer flow and flows over the gold surface of the SPR slide. When molecules are attached to the gold surface, the refractive index (RI) of the medium changes from that of a pure buffer (background RI) and is observed as the SPR signal change.

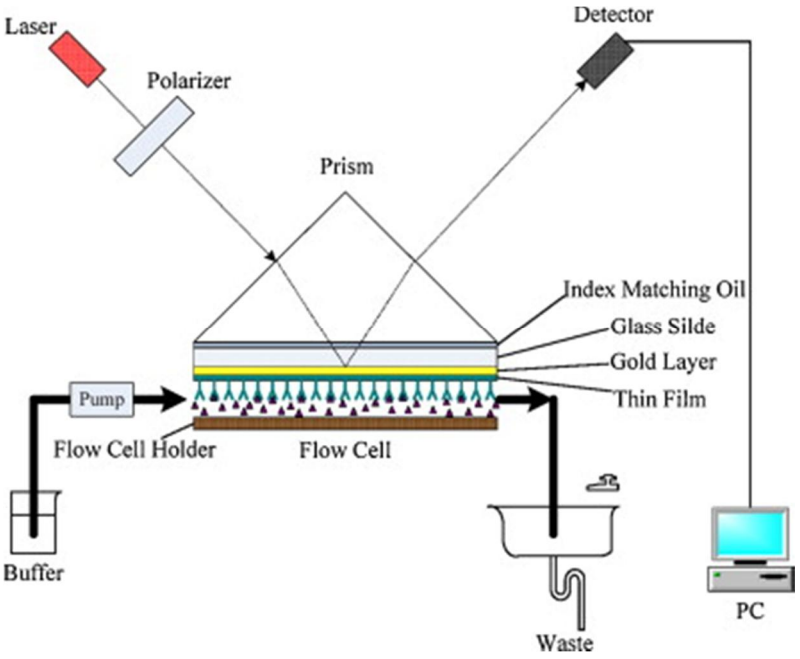

Fig. 1. *The Kretschmann type configuration for surface plasmon signal detection.*

Optical system: The Kretschmann ATR configuration comprises a triangle prism made of BK7 optical glass, and a removable sensor slide which can easily be inserted into the instrument without affecting the optical geometry of the system. The light source of the system is composed of a laser diode with an emission wavelength of 670 nm. For two-wavelength SPR measurements of cadmium stearate (CdSA) two laser diodes with emission wavelengths of 635 and 670 nm were used for the two channels, respectively. The laser and detector are fixed at the end of two bars of the angle scanning system driven by a stepper motor in order to assure collection of light for all angles of incidence. It should be noted that the reflected light spot does not drift during the full wide angular range scan.

Flow system: The used configuration is a two-channel system device, which means that the two optical measuring spots and the two separate fluidic channels are operated by the

same peristaltic pump with flow rates from 5 to 200 µl/min. Fluid channels are connected to a 6-port injector valve commonly used for flow injection. The instrument is equipped with one 12-port valve working as two 6-port systems connected to the same switch, thus giving simultaneous injections for both channels. The sample is loaded into a loop determining the sample volume.

The buffer container is connected through tubing to the integrated peristaltic pump. The sample is injected manually with a syringe to the corresponding sample loop through the two injection ports for the both channels. The sample injected into the loop is loaded into the main stream of buffer flow by the handle switch of the injector.

The flow cell is molded from poly-dimethyl siloxane (PDMS) rubber. PDMS is used because it is easy to prepare flow cells of different height and volume. Moreover, the material is relatively inert and the PDMS flow cell also acts as an insulator. The height of the flow cell used was about 80 µm, to enable the minimizing of the sample size and obtaining correct reaction-limited kinetic values (Gervais et al., 2005). The tubing used was 125 µm PEEK, and the dead volume of the system was about 10 µl (the volume from the output of the 12-port valve to the inlet of the flow chamber).

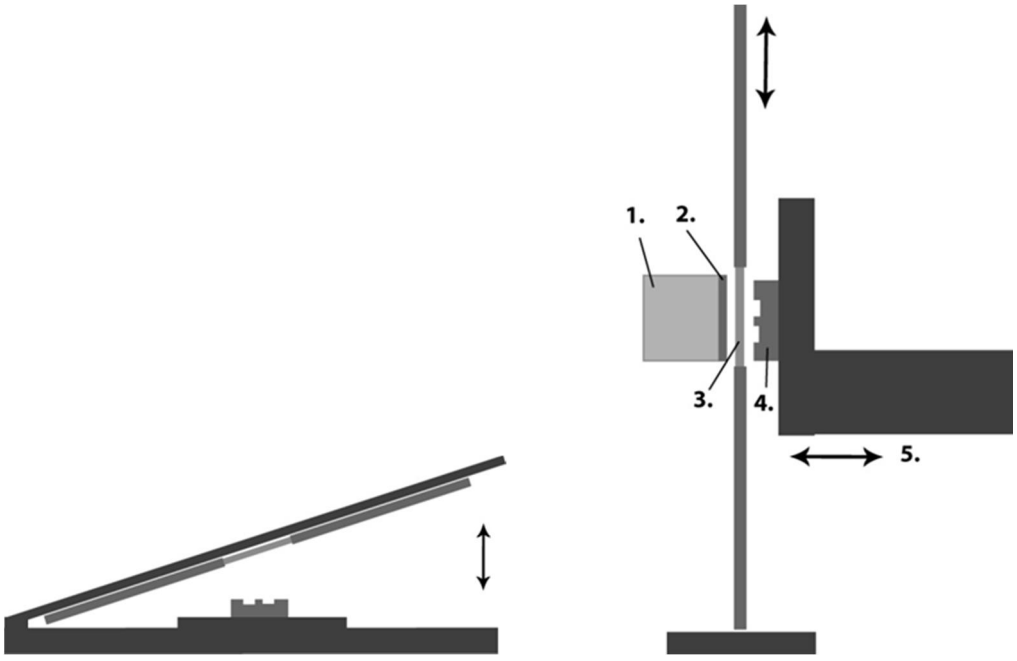

(a) **(b)**

Fig. 2. *Schematic pictures of (a) the immobilizer accessory and (b) the SPR sample insertion mechanism. The numbered parts are: (1) prism, (2) index matching elastomer, (3) SPR sensor slide, (4) PDMS flow cell and (5) closing mechanism.*

Gold sensor chips and chip holder: The removable chip holder was utilized while changing the slides into the flow cell. The flow cell, chip holder and prism are separated from each other automatically and the chip holder can be pulled out. A new chip can be

then replaced into the holder and the "Dock closing" can be executed in the software to drive the pieces together again. Thus the chip is applied into the holder either before or after coating the gold substrate. A schematic picture of the chip holder is presented in Fig. 2b. The glass slide (Schott D 263, 20 mm × 12 mm × 0.5 mm) with 50 nm gold layer sputtered on 2 nm of Cr was used as the sensor chip. The gold slide can easily be replaced into the holder, making it possible to prepare the substrate coating both inside and outside the equipment.

Immobilizer: An equipment called "immobilizer" (Fig. 2a), compatible with sensor slides and slide holder of the instrument was used for in situ coating or functionalization of the sensor plates outside the instrument. In this way possible contamination can be avoided and the two channels can be individually coated or functionalized with different molecules, if needed.

4.2.2 Data handling

Data acquisition: The instrument is controlled by user interface software. A standard configuration which consists of two 670 nm lasers (one laser per channel) was used for all measurements, except for the two-wavelength approach where one of the lasers was exchanged for a 635 nm laser. The response signal can be sampled with user-defined time pattern. Our measurements were carried out with a standard 1 Hz sample rate. If high speed sampling is needed, the sampling can be set to a 200 Hz sample rate. If extremely low baseline noise is important, the integration time of the signal up to 1 min or more can be utilized.

The user interface has two main modes of measurement, the angular scanning (AS) mode and the reflected light in fixed angle (FA) mode. In the FA mode the laser angle is set to a falling slope at a fixed angle and changes on the surface are seen as reflectance changes. The AS mode measures reflectance versus angle with a user-defined angular range and resolution and the minimum reflection position can be monitored on-line in the sensogram view of the user interface. This mode and post-processing of the curves by fitting Fresnel equations allows calculation of the surface RI or the layer thickness as a function of time.

Signal fitting with Fresnel equations: In order to obtain refractive index or thickness of LB films, the experimental SA curves were fitted with the Winspall 3.01 computer program, which is based on the Fresnel equations and the recursion formalism, freely available from the Max-Planck Institute for Polymer Research (MPIP-Mainz, Germany, www.mpip-mainz.mpg.de/knoll/soft/index.html). The AS curve for pure gold was simulated first in order to obtain the effective parameters of the thickness and dielectric constant of pure gold before fitting the LB films AS curves. The curves for sucrose solution were performed using the same simulation with Winspall 3.01 to obtain the refractive index of sucrose solution.

In addition, the change in SPR angle minimum or the change in reflection intensity at constant angle for EG and ethanol solutions were used for calibration curve purposes. The calibration curve data were fitted in Origin 7.0 software with the least square regression.

The calibration curve was evaluated based on the correlation coefficient (R) and standard deviation (SD). The repeatability was tested by five injections of a sample close to the limit of quantitation (LOQ) in order to estimate the maximum error for repeatability from the SD of the injections. Error for the experiments was estimated by root mean square (RMS) error equation (1) averaging the SDs of the linear fit and repeatability experiment. Limit of detection (LOD) was defined as three times and LOQ as five times the SD of baseline during the experiments performed:

$$RMS\ error\ (\%) = \sqrt{\left(\frac{SD_{slope}}{Slope}\right)^2 + \left(\frac{SD_{Repeat}}{AVG_{Repeat}}\right)^2} \times 100 \quad (1)$$

Reference data for refractive index (RI) concentration dependency was taken from CRC (Lide, 2007), and it is assumed that the *dn/dc* of the analyte is linear below 5 wt%. Differences in temperature and wavelength between reference and experimental conditions are neglected in the analysis as we measure changes in RI.

4.2.3 Sample preparation and measurements

Chemicals: Stearic acid (SA, Catalog No. 85680), sucrose (Catalog No. 84099), $CdCl_2$ (Catalog No. 20912), ethylene glycol (EG) and bovine serum albumin (BSA) (Catalog No. A4503) were purchased from Sigma, Inc. Streptavidin (Catalog No. 21125) was purchased from Pierce. HS-$(CH_2)_{11}$-$(OCH_2OCH_2)_3$-OH (EG_3) (Catalog No. TH002-02) and HS-$(CH_2)_{11}$-$(OCH_2OCH_2)_3$-biotin (EG_3-biotin) (Catalog No. TH012-02) were purchased from ProChimia Surfaces Sp. z.o.o. Ethanol (grade A) was purchased from Altia group.

Gold substrate cleaning: The gold substrates were cleaned with ammonia/hydrogen peroxide solution. The solution consists of 30% ammonia (NH_4OH), 30% hydrogen peroxide (H_2O_2) and Milli-Q water (1:1:5, v/v). The gold slides were cleaned by boiling them in the cleaning solution for 10 min. The slides were removed and rinsed with Milli-Q water, and then dried with nitrogen gas.

Sucrose, EG and ethanol solutions: The sucrose solutions of 5, 10, 25, 50 and 300 mM in water were measured with SPR in the angular scan mode. A series of aqueous ethylene glycol (EG) solutions were diluted from 2 wt% solution; ethanol solutions were diluted from 5 wt% solution. EG experiments were done in angular scan mode and ethanol experiments were done in both angular and fixed angle scan modes. The measurements were used for creating calibration curves, testing for repeatability of injections and for measuring the limit of detection (LOD) and quantitation (LOQ). The measurements were done in ambient conditions.

Stearic acid (SA) LB films: A KSV Minitrough (KSV Instruments Ltd, Helsinki, Finland) was used for the deposition of stearic acid layers on the cleaned gold slides for SPR measurements. The depositions were carried out at 23 °C using a thermostated Teflon trough (330 mm × 75 mm). The compression of the monolayer was started 10 min after spreading the monolayer substance on the subphase. A constant barrier speed of 10

mm/min was used for compressing the monolayer to the pre-determined surface pressure. After reaching the pre-determined surface pressure, the monolayer was left for stabilizing at least for 10 min before starting the deposition procedure. The speed for the deposition of mono- and multilayers of stearic acid was 5 mm/min. In the case of multilayer depositions for SA, the deposited layers were allowed to dry in air for 15 min before the subsequent layers were deposited.

Monolayers and multilayers of SA were deposited at the constant surface pressure of 30 mN/m from a subphase (10^{-4} M $CdCl_2$ in water) at pH 6. The SA mono- and multilayers were characterized by SPR measurement in air. The obtained SPR curves were fitted with Winspall 3.01 to obtain the thickness of the layers.

BSA and streptavidin with thiol self-assembled monolayers (SAM): SAM preparation on SPR gold substrates (Jung et al., 1999). Thiol SAMs were prepared with an immobilizer outside the SPR equipment to enable two channels to be coated individually (channel 1, EG_3 and channel 2, EG_3-biotin). After the cleaned gold substrates were mounted in the immobilizer, EG_3 of 0.2 mM or the mixture of EG_3 and EG_3-biotin (EG_3/EG_3-biotin, 4:1) of total concentration 0.2 mM were introduced to two different channels for self-assembly overnight. The gold substrates were then removed from the thiol solution, and the gold substrates were sonicated for 5 s and rinsed with ethanol three times to remove excess and weakly bound thiols and dried under a stream of nitrogen gas. Then EG_3 SAM and EG_3/EG_3-biotin SAM were used for SPR measurements. Nonspecific interaction between BSA and SAM was measured through injecting 0.5 mg/ml BSA in PBS (pH 7.4). After this streptavidin solution of 30 μg/ml in PBS (pH 7.4) was injected to detect the interaction between streptavidin and biotin-SAM. Measurements were performed at the flow rate of 10 μl/min with PBS (pH 7.4) as buffer.

Streptavidin–biotin kinetics: The SAM was first prepared on gold substrates (Jung, et al., 1999) by starting with the thiol solutions in pure ethanol. The cleaned gold substrates were immersed in the mixture of EG_3 and EG_3-biotin (EG_3/EG_3-biotin, 5:1) of total concentration of 0.24 mM in pure ethanol flushed with N_2 and sealed with parafilm, for self-assembling overnight. The gold substrates were then removed from the thiol solution, sonicated for 5 s and rinsed with ethanol three times to remove excess and weakly bound thiols, and finally dried under a stream of nitrogen. The prepared EG_3/EG_3-biotin SAMs were used for the measurements. After BSA solution of 0.5 mg/ml in 20 mM HEPES/150 mM NaCl (pH 7.4) was injected to prevent nonspecific interaction (Tang et al., 2006), streptavidin solution of 1.25, 2.5, 10 and 20 nM was injected to measure the specific interaction between streptavidin and biotin-SAM. The measurements were performed at the flow rate of 10 μl/min. The buffer used was 20 mM HEPES/150 mM NaCl, pH 7. The specific interaction kinetic between streptavidin and biotin was calculated with the software of Scrubber-2 package written by Myszka and collaborators (www.cores.utah.edu/interaction/index.php) (Nguyen et al., 2007).

4.3 Results and discussion

4.3.1 Angular scan of pure gold slides in air and in water

The pure gold slide was measured in both air and water and the SPR curves are shown in Fig. 3. The clear separation of the resonance angles between the SPR signals in air and in water implies the capacity of the detection. Due to the wide angular scan range (40–78°) of the instrument it was possible to measure SPR curves in air and water simultaneously, without taking the slide out of the instrument. The parameters of pure gold were fitted with Winspall. Actually, gold in our case means an effective layer with the Cr adhesion under the gold layer. The parameters, thickness, refractive index (n) and absorption coefficient (κ), obtained from fitting of pure gold in air are 53.21 nm, 0.2034 and 3.8152, respectively. The parameters in water are 54.37 nm, 0.1972 and 3.8107. The results obtained in air and in water are quite close each other and the small difference can be explained by an intermediate layer of Au/air and Au/water, in a similar way as described by Sadowski *et al*. (Sadowski et al., 1995).

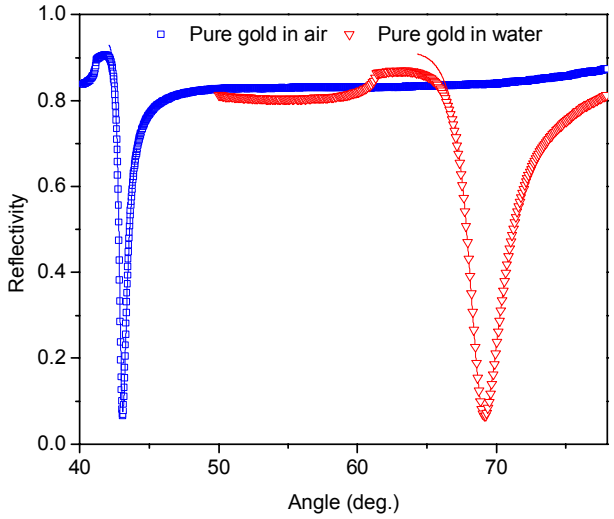

Fig. 3. *Experimental (dots) and fitted (solid) SPR curves of pure gold substrate in air and in water.*

4.3.2 Stearic acid (SA) mono- and multilayer LB films with total angle scan, two-medium and two-wavelength SPR approach

Monolayers and multilayers of SA were measured in air with angular scan mode. The obtained curves are shown in Fig. 4. The dots signify the measured, and the lines the fitted curves. The obvious shifts between the pure gold and the films with different number of layers are observed, which imply the different properties of the three LB films, e.g.

different thickness or refractive index. The angular shifts of SA layers with respect to pure gold as a function of number of layers are shown in the lower line of Fig. 5 where a good linear relation is clearly observed. In the presence of an organic layer at metal/dielectric interface, the position of the resonance angle (θ_{spr}) shifts to higher values. There is a relationship between θ_{spr}, Δn and d: $\theta_{spr} = k\,\Delta nd$, where k is a constant reflecting the experimental conditions, d is the geometrical thickness of organic layer, and Δn is the difference between the real refractive indices of the layer and the medium (Boncheva & Vogel, 1997). The SA layers are deposited in the same conditions. Therefore, k and Δn should be constant. The θ_{spr} just depends on the layer thickness d. Hence the linear relation between angular shifts and the number of layers is reasonably based on $\theta_{spr} = k\,\Delta nd$. The measured curves were fitted to the theoretical model (solid curves in Fig. 4) with Winspall 3.01. The fit is acceptable if the fitted are slightly deeper than the experimentally measured signals, as observed in Fig. 4.

The SA LB layers are deposited at pH 6 by using cadmium stearate and transferred onto gold surface under the surface pressure of 30 mN/m. The fitting was performed assuming the refractive index of SA 1.45 (Ren et al., 2004). The thicknesses from fitting as a function of number of layers presented in Fig. 5 indicate a linear relation, as expected. The thickness increment in the plot is 2.68 nm/layer, which is in close agreement with the value of ca. 2.5 nm presented in literature (Roberts, 1984).

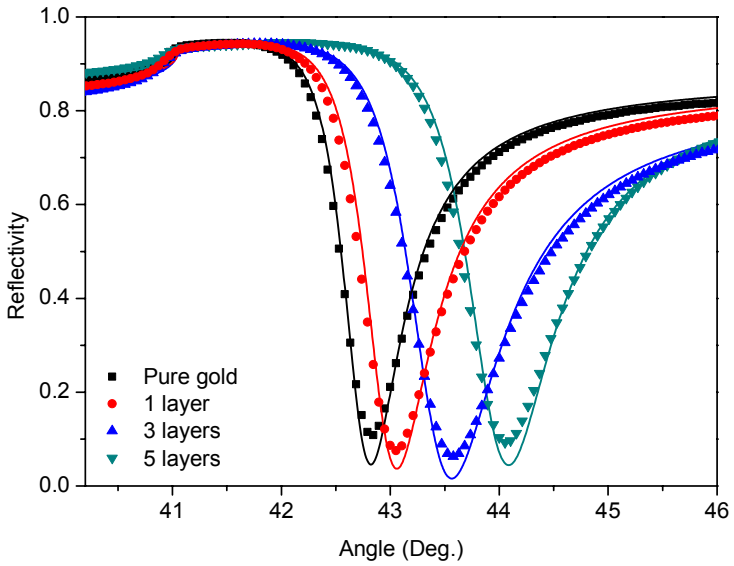

Fig. 4. *Experimental (dots) and fitted (solid) SPR curves for pure gold, 1, 3, and 5 SA LB layers.*

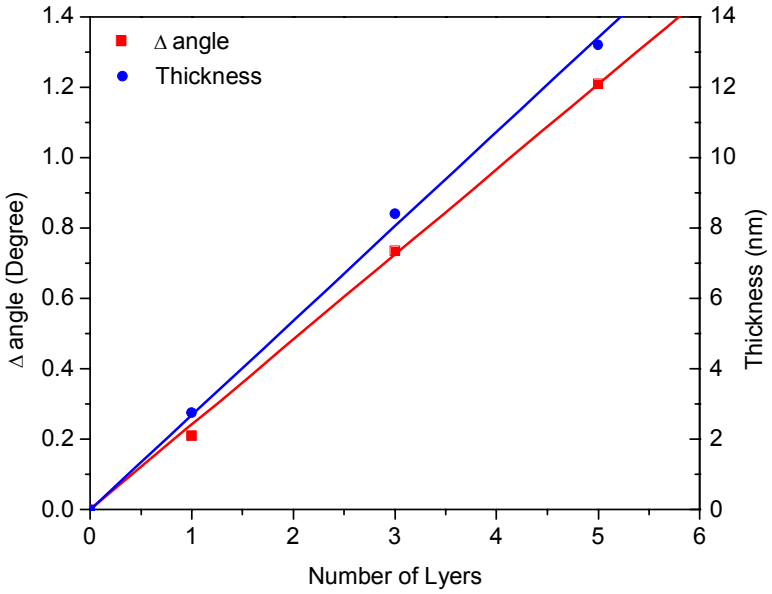

Fig. 5. *The angle and thickness as a function of the number of layers. The solid lines illustrate a linear regression fit to the data. (R^2 for angle and thickness, respectively 0.9991 and 0.9927). The slope for thickness is 2.685 nm/layer.*

The approach above for determining thin film thicknesses (*d*) can only be used if the refractive index (*n*) is known or assumed, and vice versa because it is not possible to obtain both of them from a single SPR experiment (Peterlinz & Georgiadis, 1996). This is an obvious limitation for standard SPR instrumentation when there is a need for characterizing properties of thin films, especially when it comes to monolayers with a thickness of just a few nanometers. However, by modifying and improving the SPR instrumentation to hold two different laser light sources with two different wavelengths it is greatly possible to overcome this limitation, thus allowing unambiguous determination of the refractive index and thickness for ultrathin films like LB layers (Boncheva & Vogel, 1997). Using two different wavelengths creates two sets of different refractive indices which eventually can be used to extract a unique refractive index for the used wavelength and thickness of the thin layer (Peterlinz & Georgiadis, 1996; Peterlinz et al., 1997). However, also the two-wavelength method has a limitation. In order to obtain the actual n and d, we need to know the dispersion relation of the material between the two different wavelengths. Often this dispersion relation cannot be found in literature and has to be determined by other methods. Here, we briefly present an easy and powerful approach for obtaining simultaneously the dispersion relation of layers, refractive index and thickness. The stearic acid monolayer was measured in two different media (both in air and water) with the two-wavelength SPR approach (channel 1: 635 nm; channel 2: 670 nm), see Fig. 6. The unique refractive index (using two different wavelengths) and thickness were obtained from this two-medium measurement. This also enabled extraction of dispersion relation between the two wavelengths, which could then be used for the two-wavelength SPR approach for the stearic acid monolayer.

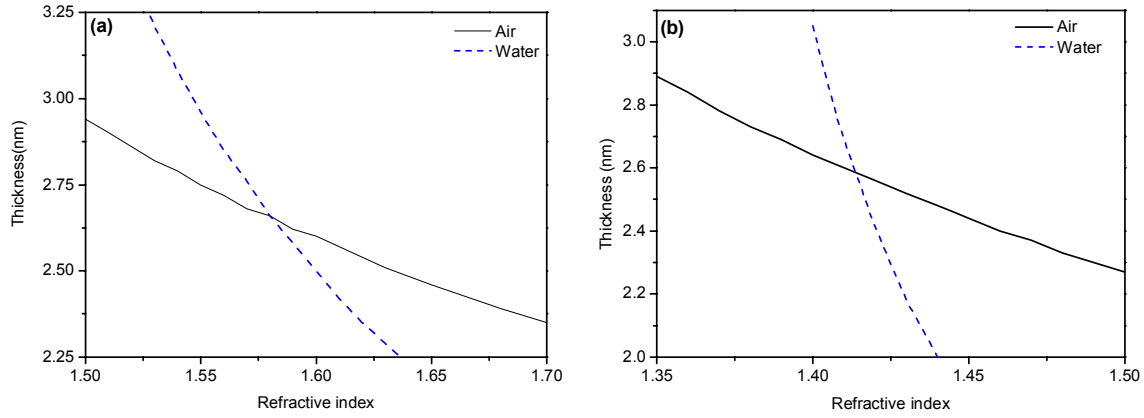

Fig. 6. *Results for SA monolayers determined by two-medium measurements for wavelengths of 635 nm (a) and 670 nm. (b). The RI and thickness for 635 and 670 nm (intersection in (a) and (b)) are 1.58, 2.66 nm and 1.4138, 2.585 nm, respectively.*

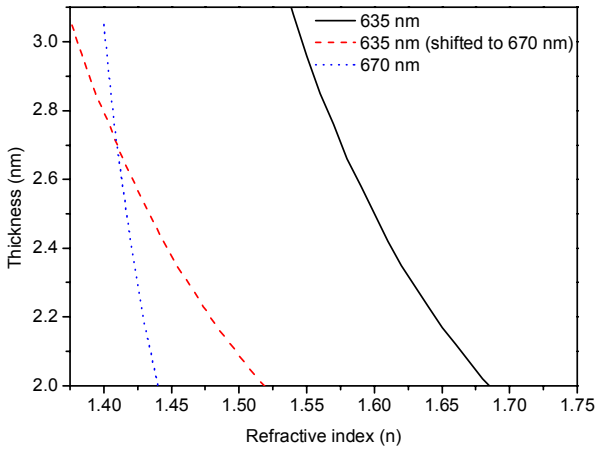

Fig. 7. *The results of simultaneous determination of refractive index and thickness with two-wavelength SPR measurements. The RI and thickness (intersection) is 1.41 and 2.7 nm.*

The results for the two-medium measurements are shown in Fig. 6. The intersection of the two curves in Fig. 6 gives the unique refractive index (RI) and thickness for both wavelengths (635 and 670 nm). The RI and thickness for the SA monolayer for wavelengths of 635 nm and 670 nm are 1.5800, 2.66 nm and 1.4138, 2.585, respectively. The dispersion for the SA monolayer between 635 and 670 nm, Δn (635 nm, 670 nm) = 0.1662 ($dn/d\lambda$ = 0.00463), which is obtained from the two-medium measurements, is then used to shift the RI of 635 nm to 670 nm to find the real intersection at a wavelength of 670 nm. The results are shown in Fig. 7. The unique RI at 670 nm and the thickness for the SA monolayer obtained from the two-wavelength measurement in water are 1.41 and 2.7 nm, respectively. The RI of SA monolayer for 670 nm obtained from the two-medium measurement was 1.4138, which is in good agreement with the RI from the two-wavelength measurements. Additionally, the three thickness values from two-medium (air

and water) and two-wavelength measurements, 2.66, 2.585 and 2.7 are also quite close to each other and these are also in good agreement with the average thickness (2.68 nm) per layer for SA multilayers determined above by assuming the refractive index. The average value for these four thicknesses (2.66, 2.585, 2.7, and 2.68) is 2.656. It has a very low standard deviation (SD) and relative standard deviation (RSD), 0.05 and 1.89%, respectively. These results further prove the fact that the goniometer based standard or custom modified SPR instrument shows high performance and is a suitable to be utilized as a refractometer for ultrathin films.

4.3.3 Sucrose solutions

The sucrose solutions of different concentrations were measured in angular scan mode at the flow rate of 50 µl/min. In the angular scan mode, the measured curves and dynamic angle change as a function of time can be simultaneously acquired, which provides us with more information for the measured samples. Fig. 8 shows the angle change as a function of time for five different concentrations, 5, 10, 25, 50 and 300 mM. Based on the angle at different concentrations from Fig. 8a, the angle shift as a function of concentrations is achieved (Fig. 8b), which indicates a good linear relation. This angle shift is a result of the refractive index of sucrose solution (the medium in contact with gold surface). The refractive index of sucrose increases linearly at the lower concentration, which can be confirmed by the literature (Fig. 10) while at the higher concentration the refractive index versus concentration is nonlinear (Lide, 2007). Therefore, the linear refractive index change results in the linear angle shift.

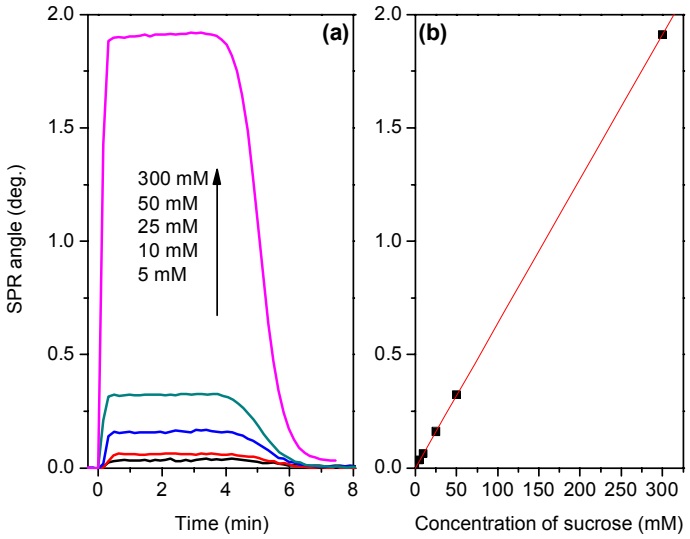

Fig. 8. *(a) Angular change as a function of time for 5, 10, 25, 50 and 300 mM sucrose in water. (b) Angular change as function of concentration of sucrose solution. The dots are from measurement, and the solid line is a linear regression of the data (R^2 = 0.99999).*

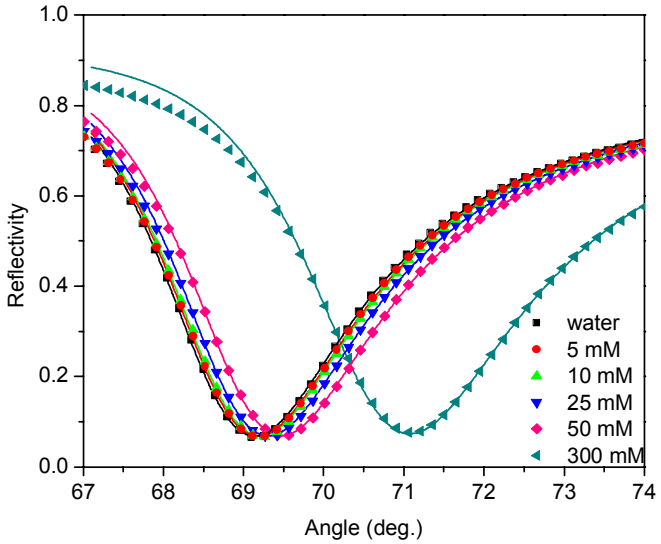

Fig. 9. *Measured (dots) and fitted (solid) SPR curves for water, 5, 10, 25, 50 and 300 mM sucrose in water.*

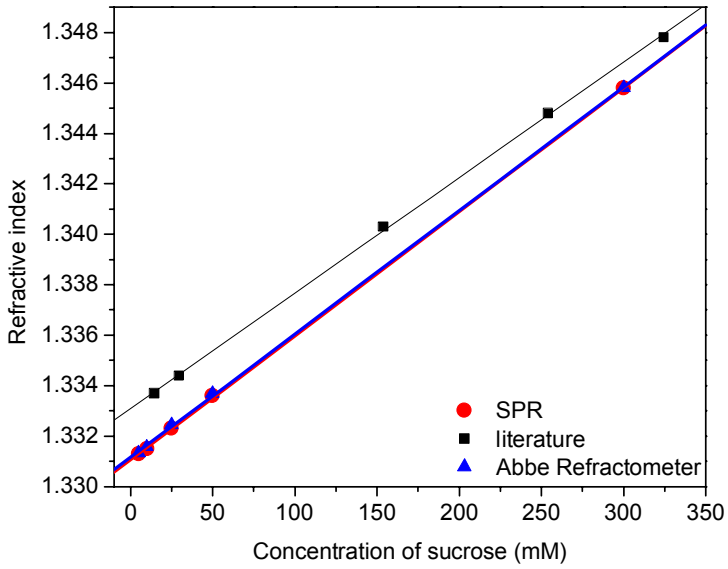

Fig. 10. *Refractive index of sucrose solution from SPR, Abbe Refractometer and literature (Lide, 2007) as a function of concentration. The solid lines are the linear regression fitting (R^2 respectively 0.99994, 0.99986 and 0.99959). The linear equations are: Y = 1.33107 + 4.91485E−5 × X, Y = 1.33116 + 4.89234E−5 × X, Y = 1.3331 + 4.57272E−5 × X.*

The measured SPR curves as a function of concentration are shown in Fig. 9. These curves are fitted (solid curves in Fig. 9) with Winspall 3.01. The refractive index of water for fitting is assumed to be 1.33096, from the determination with Abbe Refractometer (Fig. 10). The obtained refractive indices of the sucrose solution as a function of the concentration are shown in Fig. 10. In order to use the SPR system as a refractometer, we also determined the refractive indices of sucrose solution with Abbe Refractometer at the

wavelength of 633 nm at 25 °C (triangles in Fig. 10); they have a linear relationship with concentration. Moreover, the refractive indices from SPR are consistent with those measured with Abbe Refractometer. However, they are somewhat different from the refractive indices in literature (Lide, 2007), which is possibly a result from the different measuring conditions, at 670 nm and room temperature for SPR, 633 nm and 25 °C for Abbe and 589.3 nm and 20 °C in literature.

4.3.4 Ethanol and EG solutions using angular and fixed angle scans

Ethanol and EG were measured with AS mode. However, in order to make a comparison, SPR measurements with FA mode for ethanol were also performed. For the ethanol experiments, the lowest detectable concentrations were 0.096 wt% for AS and 0.0095 wt% for FA. For ethylene glycol AS experiment, the lowest concentration used was 0.139 wt%.

All experiments were plotted as signal versus mass concentrations and fitted with linear fit (Fig. 11). Fit results are displayed in Table 1. The theoretical *dn/dc* of the analytes are shown as reference, as well as the conversion coefficients of signal to refractive index unit (RIU), are summarized in Table 2.

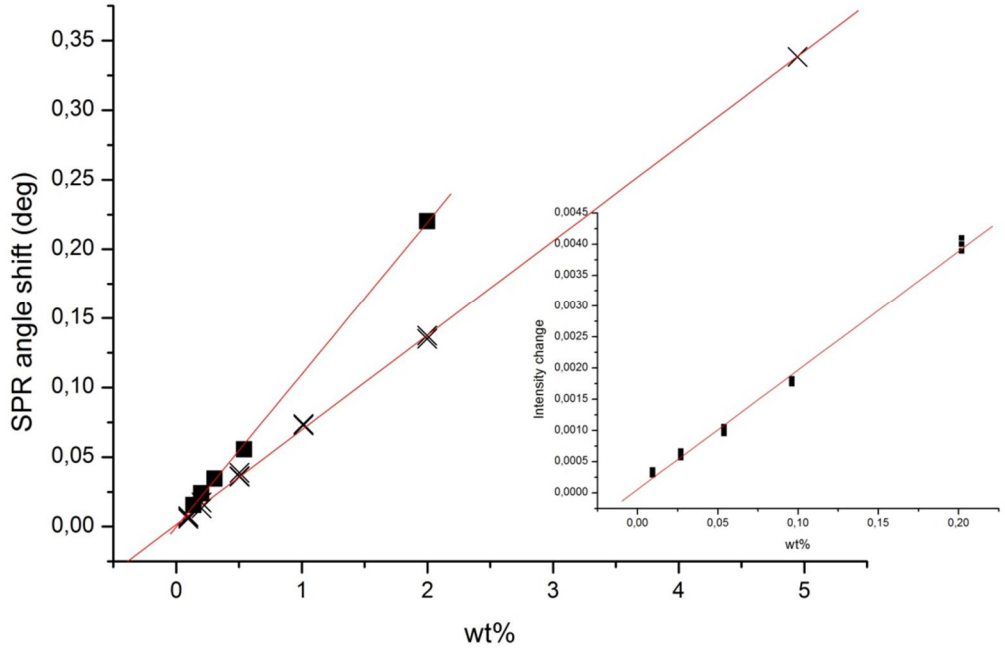

Fig. 11. *SPR angle minimum shift as a function of ethanol (×) and ethylene glycol (■) concentration in angular scan mode. Inset: Fixed angle intensity as a function of ethanol concentration in a fixed angle experiment.*

The data of all experiments fit well into a linear equation, as all the R values are close to 1.0. Based on the R values, the AS experiments give better linear fits than the FA experiments. This is reasonable as the SPR minima shifts linearly with the change of RI of the sample solution in the AS mode, and in the FA mode we measure the near-linear area of the SPR-band slope. Theoretically, all the intercepts should be zero in all cases, as zero change in RI should result in zero signal change. In an analytical method, a calibration curve would be corrected to make this value to pass through zero. The standard deviation of a fit is the root mean square (RMS) error for the line fit, and it is further used in error calculations.

The SD of repetitive injections was used to estimate the maximum error of the experiment. For the EG no repetitions were done, and the error for this was estimated from the ethanol experiment. The experimental analytical error was calculated using RMS averaging. The results are displayed in Table 2. LOD and LOQ in terms of the RI of the analyte were calculated from the SD of the baseline of each experiment and converted to RI units by using the conversion coefficient of the linear fits. The results are displayed also in Table 2.

The LOD and LOQ values for the experiments are excellent, which indicates that we are able to measure analytically meaningful changes of RI in the range of 10^{-6} at best. The FA mode has a lower level of detection (higher sensitivity), but it has poorer linearity and larger relative RMS error than the AS mode. The FA mode is clearly better for measuring really small changes in RI because of its sensitivity, and the AS mode is better for experiments where a larger dynamic range is needed. Other solvent-analyte pairs could be used to test the dynamic range further, as long as they are compatible with PDMS.

Table 1. *Linear fit data for the experiments. Slope and SD in units are deg/wt% for AS and RU/wt% for FA. Y-intercept unit is deg for AS and RIU for FA. Unit for dn/dc is RI/wt%. The calibration coefficient is (ds/dc)/ (dn/dc) = (ds/dn) in 1/deg for AS and 1/RIU for FA.*

	Slope (*ds*/*dc*)	Y-intercept	R^2	SD (fit)	Theor (*dn*/*dc*)	Conv. coeff.
EG-AS	0.109748	−1.55E−04	0.999647	0.002618	9.49E−04	115.62
EtOH-AS	0.06817	0.0014	0.99977	0.0019	6.00E−04	113.62
EtOH-FA	0.01914	5.60E−05	0.9972	1.04E−04	6.00E−04	31.9

Table 2. *Relative errors in arbitrary units. RMS error in percentages. Background SD, in deg for AS and in RIU for FA. LOD and LOQ for change in RI for the experiments.*

	Err (slope)	Err (rep)	RMS err %	SD (bg, signal)	LOD (RIU)	LOQ (RIU)
EG-AS	0.0239	0.05	5.54	7.03E−04	1.82E−05	3.04E−05
EtOH-AS	0.0279	0.0462	5.4	1.35E−03	3.55E−05	5.92E−05
EtOH-FA	0.00542	0.0681	6.83	6.27E−05	5.90E−06	9.83E−06

4.3.5 Nonspecific and specific binding of BSA and streptavidin to thiol self-assembled monolayers (SAM)

The dynamic change of adsorption of BSA on the SAM obtained with the fixed angle scan are shown in Fig. 12b. Relatively clear nonspecific adsorption of BSA can be observed. Moreover, the intensities of nonspecific adsorption for EG_3 and EG_3/EG_3-biotin SAMs are different. The adsorption of BSA to EG_3/EG_3-biotin SAM is stronger than for EG_3 SAM. Amount of BSA binding to EG_3 SAM is almost close to zero because the signal for BSA binding to EG_3 SAM returns to baseline after rinsing with buffer. After that, 30 µg/ml streptavidin in PBS is injected to both channels. Fig. 12a shows the sensogram of streptavidin binding. The signal for EG_3 SAM is clearly lower than for EG_3/EG_3-biotin. Moreover, the streptavidin binding signal for EG_3/EG_3-biotin is also greatly stronger than that of BSA adsorption (Fig. 12a), which further implies a strong specific interaction between streptavidin and biotin.

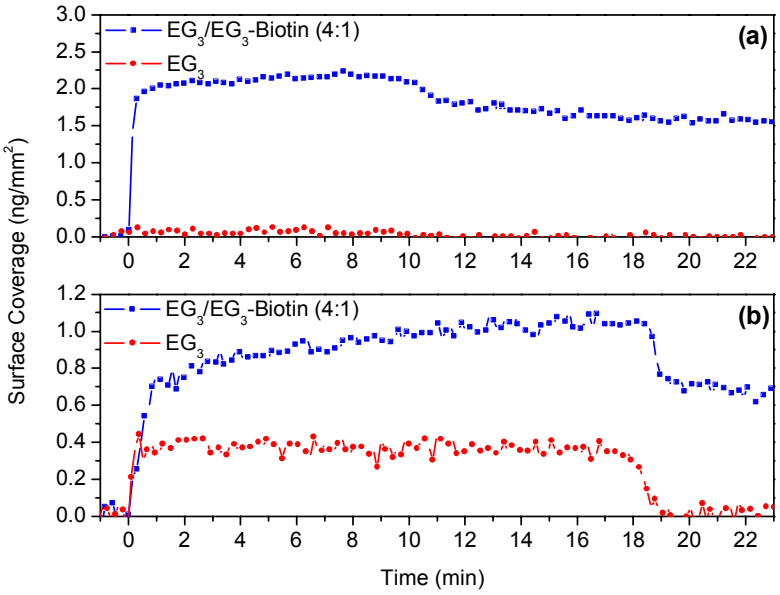

Fig. 12. *SPR sensogram for binding of BSA and streptavidin to the functionalized surface, thiol SAM. (a) Specific binding of streptavidin solution of 30 µg/ml to biotinylated thiol SAM. (b) Nonspecific binding of BSA solution of 0.5 mg/ml to thiol SAM. Flow rate: 10 µl/min. EG_3: HS-$(CH_2)_{11}$-$(OCH_2OCH_2)_3$-OH, EG_3-biotin: HS-$(CH_2)_{11}$-$(OCH_2OCH_2)_3$-biotin. EG_3 SAM and EG_3/EG_3-biotin (molar ratio 4:1) were prepared outside the SPR equipment.*

4.3.6 Determination of kinetics between streptavidin and biotin

The measured SPR sensograms are shown in Fig. 13. The sensograms are processed with the Scrubber-2 software to obtain affinity of streptavidin with biotin-SAMs (Nguyen, et al., 2007). The calculation based on Fig. 13 gives a value of K_A of 1.01×10^8 M^{-1}, which is the affinity constant for single sub-unit of streptavidin to the immobilized biotin. This value of K_A is comparable with the solution-based value of 2×10^7 M^{-1} (Green & Toms, 1973), indicating that coating of the gold substrate outside the equipment is feasible.

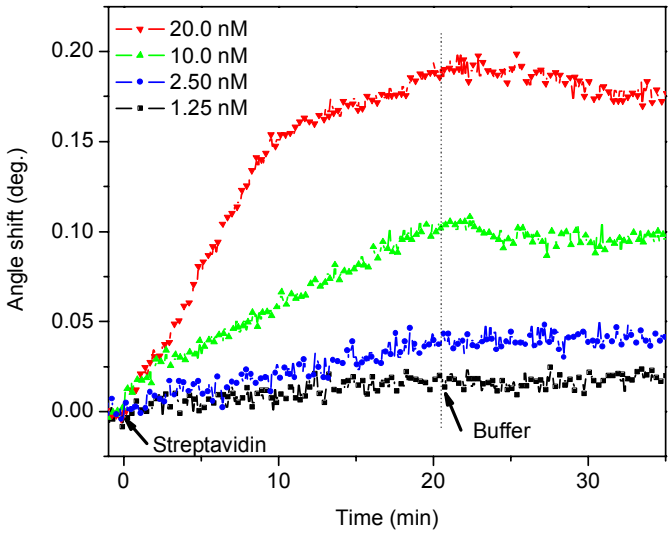

Fig. 13. *SPR sensogram for the interaction of streptavidin with the functionalized surface, EG_3-biotin SAMs. Streptavidin solutions: 1.25, 2.5, 10 and 20 nM. Flow rate: 10 µl/min. EG_3 SAM and EG_3/EG_3-biotin (molar ratio 5:1) were prepared outside the SPR device.*

4.4 Conclusions

We have shown that the goniometer based SPR instrument could be utilized as a refractometer for thin films as well as for bulk solutions. Especially the two-wavelength approach combined with the two-medium measurements showed its capabilities to determine simultaneously the dispersion, refractive index and thickness of thin films. Moreover, the use of the wide angular scan range from 40° to 78° enables analysis both in gas and liquid phases. The tested sensor-plate holder, designed for easy "drop-in" placement in the instrument seems to work well. The gold slide can be coated either inside or outside the instrument with practically equal results. Additionally, the use of two measurement channels enables on-line reference signal detection or duplicates measurements.

When reference correction is needed, the angular scan mode is more versatile than the fixed angular mode, especially if the RI-difference between the channels increases, while the angular scan mode does not have the same problem. This is useful in biochemical systems where there is a high degree of surface immobilization on one channel, while the other is being used to subtract matrix interactions from the injection.

Acknowledgements

The authors want to thank China Scholarship Council (CSC) for funding the Huamin Liang's study overseas. We are grateful to Jussi Tuppurainen from BioNavis for his valuable help and comments concerning our work. We also would like to thank Arto Urtti for his valuable opinions concerning our manuscript.

4.5 References

Boncheva, M., & Vogel, H. (1997). Formation of stable polypeptide monolayers at interfaces: Controlling molecular conformation and orientation. *Biophysical Journal, 73*(2), 1056-1072.

Critchley, P., Kazlauskaite, J., Eason, R., & Pinheiro, T. J. T. (2004). Binding of prion proteins to lipid membranes. *Biochemical and Biophysical Research Communications, 313*(3), 559-567.

Du, X. Z., & Wang, Y. C. (2007). Directed assembly of binary monolayers with a high protein affinity: Infrared reflection absorption spectroscopy (IRRAS) and surface plasmon resonance (SPR). *Journal of Physical Chemistry B, 111*(9), 2347-2356.

Fitrilawati, F., Renu, R., Baskar, C., Xu, L., Chan, H., Valiyaveettil, S., et al. (2005). Langmuir-Blodgett-Kuhn and self-assembled films of asymmetrically substituted poly(paraphenylene). *Langmuir*, 12146-12152.

Gervais, T., Tsau, C., El-Ali, J., Manalis, S. R., & Jensen, K. F. (2005). *Convection-limited surface transport in nanofluidic channels.* Paper presented at the Proceedings of the Ninth International Conference on Miniaturized Systems for Chemistry and Life Sciences.

Green, N. M., & Toms, E. J. (1973). The properties of subunits of avidin coupled to sepharose. *Biochem J, 133*(4), 687-700.

Hanken, D. G., Naujok, R. R., Gray, J. M., & Corn, R. M. (1997). Synthesis, spectroscopic characterization, and electro-optical properties of noncentrosymmetric azobenzene/zirconium phosphonate multilayer films. *Analytical Chemistry, 69*(2), 240-248.

Homola, J., Yee, S. S., & Gauglitz, G. (1999). Surface plasmon resonance sensors: review. *Sensors and Actuators B: Chemical, 54*(1–2), 3-15.

Ito, S., Imura, T., Fukuoka, T., Morita, T., Sakai, H., Abe, M., et al. (2007). Kinetic studies on the interactions between glycolipid biosurfactant assembled monolayers and various classes of immunoglobulins using surface plasmon resonance. *Colloids and Surfaces B: Biointerfaces, 58*(2), 165-171.

Jung, L., Nelson, K., Campbell, C., Stayton, P., Yee, S., Perez-Luna, V., et al. (1999). Surface plasmon resonance measurement of binding and dissociation of wild-type and mutant streptavidin on mixed biotin-containing alkylthiolate monolayers. *Sensors and Actuators B-Chemical*, 137-144.

Lide, D. R. (2007). *CRC Handbook of Chemistry and Physics (88th ed.)*: CRC Press.

Lin, M., Chiu, H., Fan, F., Tsai, H., Wang, S., Chang, Y., et al. (2007). Kinetics and enthalpy measurements of interaction between β-amyloid and liposomes by surface plasmon resonance and isothermal titration microcalorimetry. *Colloids and Surfaces B: Biointerfaces, 58*(2), 231-236.

Malmsten, M. (1999). Studies of serum protein adsorption at phospholipid surfaces in relation to intravenous drug delivery. *Colloids and Surfaces a-Physicochemical and Engineering Aspects, 159*(1), 77-87.

Masson, J.-F., Battaglia, T. M., Khairallah, P., Beaudoin, S., & Booksh, K. S. (2007). Quantitative Measurement of Cardiac Markers in Undiluted Serum. *Analytical Chemistry, 79*(2), 612-619.

Nguyen, B., Tanious, F., & Wilson, W. (2007). Biosensor-surface plasmon resonance: Quantitative analysis of small molecule-nucleic acid interactions. *Methods*, 150-161.

Peterlinz, K., & Georgiadis, R. (1996). Two-color approach for determination of thickness and dielectric constant of thin films using surface plasmon resonance spectroscopy. *Optics Communications*, 260-266.

Peterlinz, K. A., Georgiadis, R. M., Herne, T. M., & Tarlov, M. J. (1997). Observation of hybridization and dehybridization of thiol-tethered DNA using two-color surface plasmon resonance spectroscopy. *Journal of the American Chemical Society, 119*(14), 3401-3402.

Ren, S. L., Yang, S. R., Wang, J. Q., Liu, W. M., & Zhao, Y. P. (2004). Preparation and tribological studies of stearic acid self-assembled monolayers on polymer-coated silicon surface. *Chemistry of Materials, 16*(3), 428-434.

Roberts, G. G. (1984). Langmuir-Blodgett films. *Contemporary Physics, 25*(2), 109-128.

Sadowski, J. W., Korhonen, I. K. J., & Peltonen, J. P. K. (1995). Characterization of Thin-Films and Their Structures in Surface-Plasmon Resonance Measurements. *Optical Engineering, 34*(9), 2581-2586.

Shumaker-Parry, J. S., & Campbell, C. T. (2004). Quantitative methods for spatially resolved adsorption/desorption measurements in real time by surface plasmon resonance microscopy. *Analytical Chemistry, 76*(4), 907-917.

Striebel, C., Brecht, A., & Gauglitz, G. (1994). Characterization of Biomembranes by Spectral Ellipsometry, Surface-Plasmon Resonance and Interferometry with Regard to Biosensor Application. *Biosensors & Bioelectronics, 9*(2), 139-146.

Tang, Y., Mernaugh, R., & Zeng, X. (2006). Nonregeneration Protocol for Surface Plasmon Resonance: Study of High-Affinity Interaction with High-Density Biosensors. *Analytical Chemistry, 78*(6), 1841-1848.

Taylor, A., Ladd, J., Etheridge, S., Deeds, J., Hall, S., & Jiang, S. (2008). Quantitative detection of tetrodotoxin (TTX) by a surface plasmon resonance (SPR) sensor. *Sensors and Actuators B: Chemical, 130*(1), 120-128.

5 CHARACTERIZING ULTRITHIN AND THICK ORGANIC LAYERS BY SURFACE PLASMON RESONANCE THREE-WAVELENGTH AND WAVEGUIDE MODE ANALYSIS*

Abstract:

A three-wavelength angular-scanning surface plasmon resonance based analysis has been utilized for characterizing optical properties of organic nanometer-thick layers with a wide range of thicknesses. The thickness and refractive index were determined for sample layers with thicknesses ranging from subnanometer to hundreds of nanometers. The approach allows for simultaneous determination of both the refractive index and thickness without prior knowledge of either of them and without the help of other instruments, opposite to current methods and approaches. The applicability of the three-wavelength angular-scanning surface plasmon resonance approach was demonstrated with ex situ deposited mono- and multilayers of stearic acid and hydrogenated soy phosphatidylcholine and by in situ layer-by-layer deposition of two different polyelectrolyte multilayer systems. In addition to this approach, the surface plasmon resonance waveguide mode was utilized to characterize organic sample layers whose thicknesses border the micrometer scale. This was demonstrated by characterizing both in situ layer-by-layer deposited polyelectrolyte multilayer systems and an ex situ deposited spin-coated polymer layer.

*Adapted from (Reprinted with permission from American Chemical Society): Niko Granqvist ‡, Huamin Liang ‡, Terhi Laurila, Janusz Sadowski, Marjo Yliperttula, Tapani Viitala: Characterizing ultrathin and thick organic layers by surface plasmon resonance three-wavelength and waveguide mode analysis. Langmuir 29: 8561-8571, 2013.

‡ Contributed equally to this work

5.1 Introduction

The determination of organic ultrathin film properties, i.e., thickness (d) and refractive index (n), in the range of 0.1–100 nm is still a challenging task, especially when reaching the lower limit of 0.1–10 nm. (Hilfiker et al., 2008; Rodenhausen et al., 2011) The lower limit is highly relevant for chemical sensing, organic optics, and electronics, as well as characterizing and measuring biological processes and biological barrier layers, such as cell walls, cell membranes, and lipid bilayers. (Castellana & Cremer, 2006; Rossi & Chopineau, 2007) Furthermore, relatively thick layers from 400 nm to a few micrometers are also relatively difficult to characterize, as they fall into a gap between nano- and macro-characterization techniques. Examples of layer structures with a few micrometer thickness are, for instance, bacteria, certain cell types, such as red blood cell monolayers (Campbell, 2009), many natural structural components, such as cellulose cell walls in plants (Campbell, 2009; Ververis et al., 2004), and biologically relevant hydrogels and structural or fibrillar proteins such as actin, collagen, and keratin fibers. (Campbell, 2009) There are several techniques that provide accurate information on organic thin film properties and are commonly used for thin film characterization, e.g. ellipsometry (Azzam, 1987), spectroscopic ellipsometry (SE) (Rodenhausen, et al., 2011), surface plasmon resonance spectroscopy (SPR) (Rossi & Chopineau, 2007), quartz crystal microbalance (QCM) (Rodenhausen, et al., 2011), and atomic force microscopy (AFM) (Hansma & Pietrasanta, 1998). However, in many cases several different techniques have to be simultaneously employed to obtain a reliable estimate of d and n of ultrathin and thick organic films. (Rodenhausen, et al., 2011)

Ellipsometry and SE utilize polarized light for determining d and n of thin organic layers. In the case of SE the dispersion coefficient for materials is also obtained. (Azzam, 1987; Rodenhausen, et al., 2011) However, when using monochromatic light for determining d and n for thin organic layers by ellipsometry, these two parameters are inseparable. Therefore, it is necessary to know, assume, or measure with some other techniques either d or n. Even with a known n, it is still difficult to obtain accurate values for organic layer thicknesses below 10 nm with ellipsometry. (Tonova et al., 1996) With SE it is possible to independently determine both d and n for organic layers, but for organic ultrathin films where $2\pi dn/\lambda \ll 1$, the relative error of d becomes linked to the initial assumption of n for the layer, and a unique determination of both d and n becomes impossible. (Rodenhausen, et al., 2011) When the thickness of the sample layers approaches the micrometer range, the output vector (Ψ, Δ) obtained from ellipsometry measurements will have a periodicity, which complicates the analysis of such sample layers with single-wavelength ellipsometry. This is, however, not a major issue in SE due to multiple output vectors as a function of the wavelength. (Azzam, 1987) Characterizing sample layers with ellipsometry or SE with samples immersed in liquid is also often challenging, because of the optical setup required. The incident light and reflected light need to travel through optical windows, as well as the surrounding medium and the sample layer. This creates challenges in engineering flow systems with low volume and good flow control and prevents the use of opaque liquids. (Azzam, 1987)

QCM is a mechanical technique which makes use of an AT-cut quartz resonator oscillating at its resonance frequency. (Buttry & Ward, 1992) It can be used to measure the amount (mass) and mechanical properties (viscoelasticity) of sample layers deposited on top of the quartz crystal resonator by measuring the change in frequency and dampening of the oscillation. If the change in frequency and the dampening of oscillation are measured at several overtones, the thickness, density, and viscoelasticity of the sample layer can be obtained by theoretical modeling. (Bandey et al., 1999) However, for accurate modeling in QCM also the density of the material should be known, which is practically never accurately known for ultrathin films but is often estimated from bulk properties. (Rodenhausen, et al., 2011) Furthermore, the sensing depth of QCM in liquid media is approximately 300 nm, and highly viscoelastic layers with thicknesses in the range of 200–500 nm easily dampen the crystal oscillation completely.

AFM is a mechanical technique where an oscillating or stationary cantilever probe is brought in close contact with the sample surface until van der Waals force repulsion starts to affect the oscillation amplitude or deflection of the cantilever. The oscillation amplitude and/or deflection of the cantilever can then be used to directly measure the topography, as well as the viscoelasticity and viscoelasticity distribution in the sample layers. With AFM it is also possible to measure interaction forces, nanoscale friction, conductivity, and other properties depending on what type of probes are used for the measurements. To accurately measure sample layer thicknesses with AFM, it is necessary to use a mask or some other method to create an internal reference within the sample layer. Additionally, the film thickness obtained by AFM will depend on the tip force or tapping strength used during the measurement, especially for soft and fluid-like films where the tip can penetrate through the sample layer. Another challenge with AFM is that performing in situ measurements, especially in liquid media, is not at all a trivial procedure. (Hansma & Pietrasanta, 1998; Santos & Castanho, 2004; You & Lowe, 1996)

SPR is an optical method where the free electron plasma on a metal surface is excited by p-polarized visible light. The excitation of surface plasmons can be monitored as a function of the incoming light angle or a change in the wavelength of light. In the most common optical configuration for SPR, i.e., the Kretschmann configuration, the light is coupled to the metal layer through a glass prism from one side, while the sample and the outside medium in contact with the sample are located on the opposite side. This configuration enables signal detection which does not have any interference from the surrounding media as the incoming light is not passing through the media or sample layer as is the case with ellipsometry. (Schasfoort, 2008) To obtain d and n information on a sample layer, a single-wavelength SPR angle versus light reflection intensity spectrum can be fitted using multilayer models in the same way as in ellipsometry. In the cases where the sample layer does not absorb light at the wavelengths used for detection, the same limitations also occur for SPR as for ellipsometry; i.e., d and n are not separable variables. (Sadowski et al., 1995; Albers & Vikholm-Lundin, 2011) However, it has previously been shown that if the SPR spectra are measured in two different media (Liang et al., 2010; Albers & Vikholm-Lundin, 2011), or the SPR measurement is performed with two different wavelengths of light and the dispersion relation is known, then a unique d and n can be calculated for the sample layer (Grassi & Georgiadis, 1999; Liang, et al., 2010;

Peterlinz & Georgiadis, 1996; Zhou et al., 2001). Usually the limit of thickness determination of sample layers with SPR is taken to be around 300 nm on the basis of the fact that the plasmon evanescent field that decays exponentially penetrates approximately half of the wavelength of the incident light into the media. (Homola et al., 1999) However, when the sample layer thickness approaches and exceeds half of the wavelength of light used for detection, then a harmonic type of waveguide behavior of the SPR begins, which can be used to uniquely determine *d* and *n* of the sample layers (Aulasevich et al., 2009; Baba et al., 2010; Lévesque et al., 1994).

5.2 Materials and methods

5.2.1 Materials

Hydrogenated l-α-phosphatidylcholine (HSPC; >99%) was obtained from Avanti Polar Lipids, and stearic acid (SA; ≥98.5%), uranyl acetate dihydrate (UAc; ≥98%), poly(styrenesulfonate) sodium salt (PSS; M_w = 70 kDa), poly(allylamine hydrochloride) (PAH; M_w = 15 kDa), poly(ethyleneimine) (PEI; M_w = 750 kDa), poly(l-lysine) (PLL; M_w 300 = kDa), and hyaluronic acid (HA; M_w = 1500 kDa) were obtained from Sigma-Aldrich. NaCl, Tris, NH_3OH (30%), and H_2O_2 (30%) were of analytical grade and obtained from Sigma-Aldrich. All chemicals were used as received. All water used was Milli-Q grade with a conductivity of 18 MΩ cm^{-1} and a total organic content of <4 ppm.

5.2.2 Three-wavelength SPR measurements

Three-wavelength surface plasmon resonance measurements were performed with an SPR Navi 200-L instrument equipped with two light source pairs providing 655 and 782 nm, as well as 670 and 783 nm, wavelengths and an autosampler accessory (BioNavis Ltd., Tampere, Finland). SPR sensors were gold-coated sensors (~ 50 nm) with a chromium adhesion layer (ca. 2 nm) and were obtained from BioNavis Ltd. SPR sensors were cleaned before use by boiling them for 15 min in an NH_3 (30%)/H_2O_2 (30%)/H_2O (1:1:5, v/v) oxidizing solution.

All three-wavelength SPR experiments were processed using the BioNavis Data viewer software. Multilayer models for sample layer analysis were done by using the Winspall 3.02 software (Knoll, 2013). The three-wavelength and two-medium cross point analyses were performed by using Microsoft Office Excel 2007.

5.2.3 Compression Isotherms and Langmuir-Blodgett film deposition

A KSV Minitrough instrument (KSV-NIMA, Biolin Scientific Oy, Espoo, Finland) was used for all compression isotherms and Langmuir–Blodgett deposition experiments. The experiments were carried out at 23 °C using a thermostated Teflon trough (330 mm × 75 mm) and 50 µM UAc in the subphase. The isothermal compressions were started 10 min after the monolayer substance was spread onto the subphase. A constant barrier compression speed of 7.5 cm^2/min was used during the whole monolayer compression. For LB depositions the monolayer was first left to stabilize for 10 min at the predetermined surface pressure before the deposition procedure was started. The speed for the deposition of mono- and multilayers of SA and HSPC was 5 mm/min. The deposited layers were dried in air for at least 15 min before the SPR spectra at different wavelengths were measured. Thereafter, the multilayer buildup was continued using the same sensor. SA monolayers were deposited at surface pressures of 15 and 45 mN/m and multilayers at a surface pressure of 45 mN/m. HSPC monolayers were deposited at surface pressures of 10 and 30 mN/m and multilayers at a surface pressure of 30 mN/m.

d and *n* of the LB films were determined by three-wavelength SPR analysis from spectra of 1, 3, 5, 7, 9, and 11 deposited layers of SA, and from spectra of 1 and 3 deposited layers of HSPC. Additionally, *d* and *n* of 11 SA and 3 HSPC layers were determined by two-medium SPR analysis from spectra measured in both air and water.

5.2.4 PM-IRRAS measurements

Polarization-modulated infrared reflection absorption spectroscopy (PM-IRRAS) is a reflection-based infrared tool where p- and s-polarized spectra are simultaneously measured from a sample deposited on an IR reflecting substrate, such as an air-metal interface. (Buffeteau et al., 1991) If the substrate is a good electrical conductor (e.g., gold), there is an enhancement effect of molecular dipoles perpendicular to the surface and an elimination of dipoles parallel to the surface. This effect can be used to qualitatively determine the orientation and packing of molecules on the metal surface.

PM-IRRAS measurements were performed with a KSV-NIMA PMI 550 instrument (KSV-NIMA, Biolin Scientific Oy, Espoo, Finland). PM-IRRAS spectra of LB monolayers of SA and HSPC deposited on the SPR gold sensor at different surface pressures were recorded at an incident light angle of 80°, which gives the highest sensitivity for gold substrates. The maximum retardation wavelength was set to 3000 cm^{-1} for all measurements.

5.2.5 Polyelectrolyte multilayer deposition

The polyelectrolyte multilayer (PEM) were deposited and monitored *in situ* in the SPR Navi 200-L instrument. All PEM buildup experiments were performed in a 0.15 M NaCl, 20 mM Tris buffer at a pH 7.4 and 20 °C. The flow rate was 50 µl/min, the sample contact

time 4 min, and the rinsing time between oppositely charged polyelectrolyte injections 10 min. One layer of PEI (0.1 mg/ml) was first deposited on gold as an adhesion layer for all PEM experiments. After this, the PEMs were formed with sequential deposition of PSS and PAH (0.1 mg/ml) for PSS–PAH PEM formation or HA and PLL (0.1 mg/ml) for HA–PLL PEM formation.

The PSS–PAH PEM formation was measured up to 20 bilayers using both SPR light source pairs and up to 120 bilayers using the 782 and 655 nm SPR light source pair. The measurement was paused, and all the fluidics were thoroughly cleaned with pure water every 40 bilayers to avoid clogging of the samples in the microfluidics of the instrument.

d and *n* of the forming PEM layers were determined by three-wavelength SPR analysis from SPR spectra measured for 3, 5, and 10 bilayers for PSS–PAH, for 2 and 5 bilayers for HA–PLL, and for a relatively thick PSS–PAH multilayer consisting of 120 bilayers.

5.2.6 *Ex situ* prepared SPR waveguides

A waveguide was prepared on the SPR sensor by spin coating 5 wt % PS–PMMA in toluene solution at 1000 rpm. The spin-coated polymer layer was dried at ambient room temperature and humidity for 30 min before the SPR spectrum of the sample layer was measured. The PS–PMMA used was a random copolymer with a 24% fraction of MMA, determined with ^{1}H NMR and an M_w of 500 kDa determined by size exclusion chromatography. The copolymer was a kind gift from the Laboratory of Polymer Chemistry, Department of Chemistry, Faculty of Science, University of Helsinki. The SPR spectrum of the spin-coated polymer layer was measured in air at ambient humidity and room temperature by using a wavelength of 670 nm. The analysis of the optical properties of the waveguide was performed with the Winspall 3.02 software.

5.3 Theory

5.3.1 SPR vector function

Surface plasmons are particle waves of the free electron plasma on a metal surface, which can be excited by p-polarized light under the resonance condition (Figure S1, Supporting Information). A theoretical mathematical description for the resonance condition can be obtained by solving the Maxwell equations for a multilayer optical system. (Albers & Vikholm-Lundin, 2011) A detailed mathematical description of the SPR phenomenon is available in the Supporting Information (section SI). A general solution for a multilayered system linked to measurable or controllable variables can be obtained by using a transfer matrix formalism of 2 × 2 matrices. The overall formalism has already been published several times, and it is not in the scope of this paper to discuss it in detail again. (Albers & Vikholm-Lundin, 2011; Sadowski et al., 1995) In practice,

this matrix formalism is solved by mathematical fitting tools or by dedicated software tools developed for it, such as Winspall. (Knoll, 2013)

5.3.2 Multivariable SPR experiments

Multivariable SPR analysis has previously been described for two-variable systems. (Grassi & Georgiadis, 1999; Peterlinz & Georgiadis, 1996; Zhou, et al., 2001) These approaches have not been widely accepted, and the full analysis described in previous literature is mathematically quite complicated. However, with the ability today to accurately model and calculate multilayer optical system responses from the SPR spectrum by using matrix formalism, we can simplify the overall process and mathematical analysis for solving the sample layer properties.

As stated previously, the SPR spectrum measured in one set of conditions is in practice not sensitive to the unique differences in d and n, and only a continuum solution for the surface plasmon wave vector (k_{sp}) proportional to d and n can be deducted:

(1) $$k_{sp} \propto nd$$

In practice we can assume that k_{sp} contains all the information and constants that cause the differences in the SPR spectra measured at several wavelengths or in two different media. Hence, we can simplify the mathematical relationship in the following way. If we measure the SPR spectrum in two different media with a large enough difference in n, then a unique solution for the final sample layer can be relatively easily calculated from the intersection of the two continuum solutions where $d_1 = d_2 = d$ and $n_1 = n_2 = n$, i.e.

(2) $$\begin{cases} k_{sp1} = nd \\ k_{sp2} = nd \end{cases}$$

A similar but slightly more complex approach is to use a multiwavelength approach, as n also has a wavelength dependency, i.e., $dn/d\lambda$. However, for relatively small changes, this relationship can to a good approximation be assumed to be linear (Supporting Information, section SII, Figure S2) (CRCnetBase, 2012). Hence, this approximation allows us to find a unique solution for d and n by solving the following equation system:

(3) $$\begin{cases} k_{sp1} = n_{\lambda 1} d \\ k_{sp2} = n_{\lambda 2} d \\ k_{sp3} = n_{\lambda 3} d \end{cases}$$

where

(4) $$n_{\lambda 2} = n_{\lambda 1} + \frac{dn}{d\lambda}(\lambda_2 - \lambda_1) \qquad n_{\lambda 3} = n_{\lambda 1} + \frac{dn}{d\lambda}(\lambda_3 - \lambda_1)$$

and

(5)
$$\begin{cases} k_{sp1} = n_{\lambda 1} d \\ k_{sp2} = \left(n_{\lambda 1} + \frac{dn}{d\lambda} (\lambda_2 - \lambda_1) \right) d \\ k_{sp3} = \left(n_{\lambda 1} + \frac{dn}{d\lambda} (\lambda_3 - \lambda_1) \right) d \end{cases}$$

If even more wavelengths are available, then in theory it should be possible to use a true Cauchy relation instead of the linear approximation of dn/dλ. It is worth mentioning that the discussion above is only valid for sample layers that *do not* absorb light at the wavelengths used for SPR spectrum measurement, i.e., for $k = 0$, which is often the case for organic sample layers. If $k \neq 0$, then there is actually a unique solution for the sample layer in the $k_{sp} = d(n + ik)$ space, and the above approach would be unnecessary.

5.3.3 SPR waveguide

A so-called SPR waveguide mode can be utilized in SPR sensing when relatively thick dielectric layers are deposited on the SPR sensor surface, i.e., when the thickness of the sample layer is higher than half of the incident light wavelength. When using the Kretschmann configuration, it is even possible to couple surface plasmons and optical waveguide modes so that the excitation light and the guided wave modes are phase matched. (Aulasevich, et al., 2009) The effect of matching these conditions has been discussed previously for thin and loose hydrogels (Aulasevich, et al., 2009) and for dense spin-coated polymers (Lévesque, et al., 1994). The SPR waveguide coupling can theoretically be investigated and analyzed by using the same mathematical models as for standard SPR as described above.

5.4 Results and discussion

5.4.1 Compression isotherms and Langmuir-Blodgett deposition

The purpose of utilizing Langmuir and Langmuir–Blodgett methods in this study is discussed briefly in the Supporting Information (section SIII). Parts A and B of Figure S3 (Supporting Information, section SIII) show the compression isotherms of SA and HSPC on pure water and UAc containing subphases. UAc was chosen as the subphase counterion as it has been shown to enable the deposition of more than one monolayer of phospholipids on a solid substrate. (Tkachenko et al., 1993; Viitala & Peltonen, 1999) The compression isotherms reveal that the UAc expands the liquid state of both the SA and HSPC monolayers compared with the monolayers measured on a pure water subphase. This is an effect opposite what is usually encountered with multivalent counterions, such as Mn^{2+}, Cd^{2+}, and Tb^{3+}. (Linden & Rosenholm, 1995) Also, the area per molecule is slightly larger for both monolayers on a UAc containing subphase than with pure water.

These effects can be attributed to the complex state of uranium(IV), which forms $[UO_2(OH)_2]_2^{2-}$ or $UO_2(CO_3)_2^{2-}$ complexes at pH 5.6 used in the experiments shown in Figure S3. (Gorwyn & Barnes, 1990). The formation of these uranyl complexes consequently makes the counterion larger than simple multivalent ions. Therefore, the uranyl counterion complexes become the limiting factor in the packing of the monolayers instead of the hydrophobic lipid tail of the amphiphilic substances in the monolayer. (Györvary et al., 1996; Peltonen et al., 1994) However, the UAc counterion clearly stabilizes and rigidifies the monolayer similar to other multivalent counterions, which can be seen from the increase in the maximum pressure that can be achieved in the compression isotherm. The UAc counterions in the subphase thus enabled us to deposit mono- and multilayers of both SA and HSPC monolayers on SPR sensor slides for further optical characterization of ultrathin organic layers. The transfer ratios of all the LB depositions were close to 1 (data not shown), which indicates that the transfer of the mono- and multilayers was complete and that the transferred layers were intact and of good quality.

The PM-IRRAS (Supporting Information, section SIII, Figure S3C and D) and isotherm (Supporting Information, section SIII, Figure S3A and B) data show that the SA monolayer has a more ordered packing than the HSPC monolayer at higher surface pressures and that the order in the SA monolayer increases with increasing surface pressure. The difference in the SA and HSPC monolayer properties should clearly be reflected in the optical properties of the monolayers. Furthermore, the SA monolayer deposited from a UAc subphase is not as highly ordered as an SA monolayer deposited from a Cd^{2+}-containing subphase, which exhibits a crystalline hexagonal packing. (Györvary, et al., 1996; Peltonen, et al., 1994) For optical measurements such as SPR and ellipsometry, a slightly more random order makes comparison between the two different molecules more reliable. For example, crystalline hexagonal packing of SA with cadmium (CRCnetBase, 2012) has a relatively large effect on the optical properties of the layer (Liang, et al., 2010), which is reflected as an anomaly large dispersion coefficient for the Cd–stearate monolayer.

5.4.2 Three-wavelength and two-medium SPR analysis of ultrathin films

The SPR full angle scans measured for SA and HSPC mono- and multilayers were separately fitted with a multilayer model in Winspall for each thickness, wavelength, and appropriate surrounding medium to gather the *d*–*n* continuum solutions for the layers. The procedure started with finding the optimized optical properties for the pure SPR sensor slide by accurately fitting the background SPR scan. The optical properties of the pure slide were then used as the starting point for finding the optical properties of the deposited sample layers. Parts A–C of Figure 1 show examples of the results of the Winspall fits to the SPR full angle scans measured in air with λ = 655, 670, and 782 nm for the pure SPR sensor slide and one SA monolayer deposited at 45 mN/m. Figure 1D shows the scans measured in both air and water with λ = 783 nm for the pure SPR slide and for 11 SA monolayers deposited at 45 mN/m.

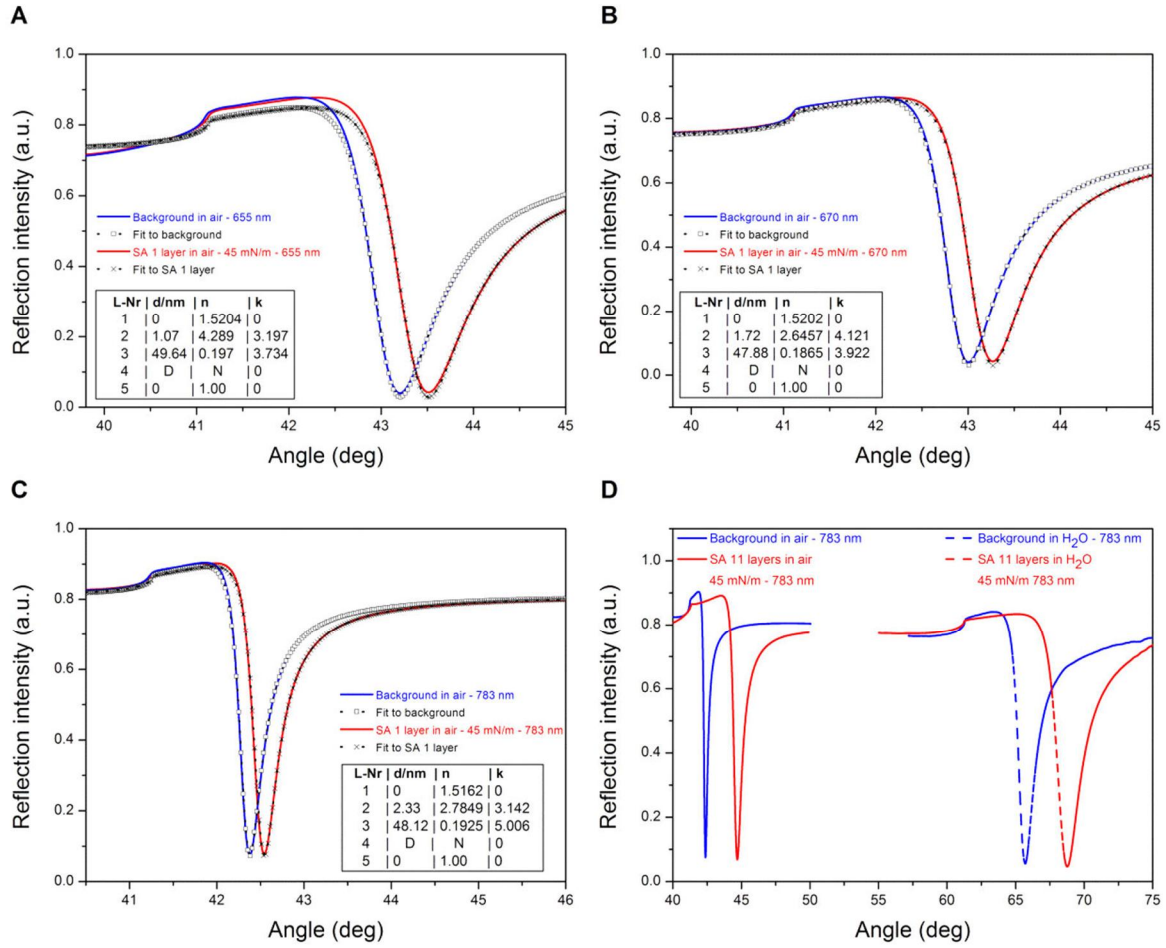

Figure 1. *SPR scans of the pure SPR sensor background (blue solid lines) and a single deposited SA monolayer (red solid lines) with corresponding Winspall fits (symbols and black dashed lines) measured with λ = 655 nm (A), 670 nm (B), and 783 nm (C). (D) SPR scans of 11 SA layers with λ = 783 nm, both in air (solid lines) and in water (dashed lines). Inset: optical parameters in Winspall fits (1 = prism, 2 = chromium, 3 = gold, 4 = sample layer, 5 = air).*

For the three-wavelength analysis, the *d* and *n* continuum solutions were plotted against each other, and the d*n*/dλ value was varied manually until a matching cross point between the wavelength pairs was found (Supporting Information, section SIV, Figure S4). In the two-medium (air and water) analysis the continuum solution was directly obtained by determining the cross point in the *d*–*n* plot. The cross point determined through the two-medium analysis is also the unique solution for *d* and *n* of the corresponding multilayer. Tables 1 and 2 summarize the results from the two-medium and three-wavelength analyses for these ultrathin films.

It is interesting to notice in the three-wavelength analysis (Table 2) that the thickness of the SA monolayers deposited at low and high surface pressures show large differences, while the differences in the thickness of the HSPC monolayers at low and high surface pressures are much smaller. This is in good agreement with the compression isotherms (Figure S3A and B, Supporting Information) and PM-IRRAS data (Figure S3C and D) of

SA and HSPC monolayers, which clearly indicated that the SA monolayer undergoes a structural ordering in the form of increased trans conformers along the hydrocarbon chain when the surface pressure is increased from 15 to 45 mN/m. On the other hand, the structural changes in the HSPC monolayer were merely due to a slight change in the tilt angle of the hydrocarbon chains with respect to the SPR sensor slide surface.

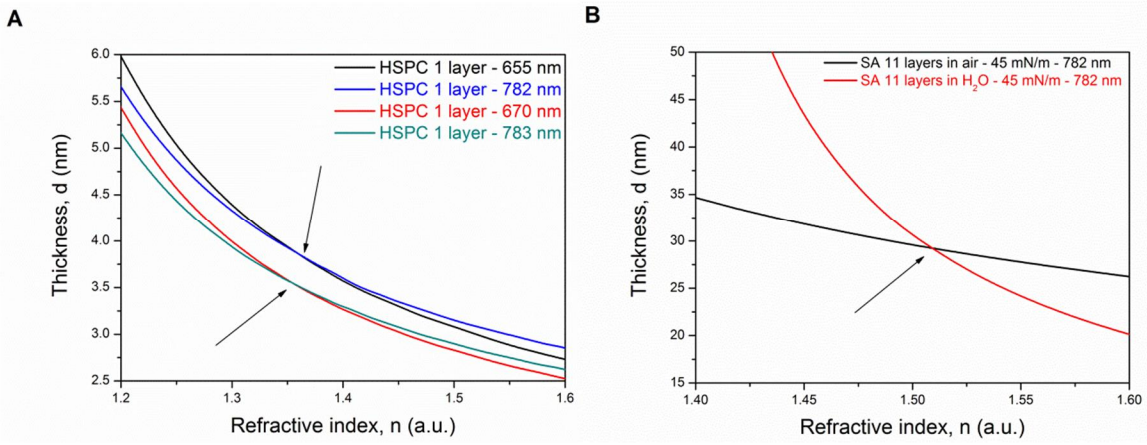

Figure 2. *Example of finding the intersection points from thickness (d) versus refractive index (n) plots of (A) 1 monolayer of HSPC in air using the three-wavelength analysis and (B) 11 layers of SA with the two-medium analysis.*

Table 1. *Thickness (d), refractive index (n), dispersion (dn/dλ), thickness per layer (d/layer), and error estimates ("±") obtained from the two-medium analysis for HSPC and SA multilayer films deposited at 30 and 45 mN/m, respectively.*

HSPC	*d* (nm)	"±"	*n* (780nm)	"±"	*dn/dλ* calculated	*d*/layer
3 LB, 655 nm	8.86	0.01	1.506	0.001		2.95
3 LB, 670 nm	8.03	0.01	1.552	0.001		2.68
3 LB, 782 nm	8.65	0.01	1.525	0.001	0.00015	2.88
3 LB, 783 nm	7.65	0.01	1.599	0.001	0.00037	2.55
AVG	**8.30**				**0.00026**	**2.77**
STD	**0.55**					**0.18**

SA	*d* (nm)	"±"	*n* (780nm)	"±"	*dn/dλ* calculated	*d*/layer
11 LB 655 nm	28.76	0.01	1.512	0.001		2.61
11 LB 670 nm	27.84	0.01	1.531	0.001		2.53
11 LB 782 nm	29.26	0.01	1.509	0.001	2.6E-05	2.66
11 LB 783 nm	28.60	0.01	1.520	0.001	9.0E-05	2.60
AVG	**28.62**				**0.00006**	**2.60**
STD	**0.59**					**0.05**

Table 2. *Thickness (d), refractive index (n), dispersion (dn/dλ), thickness per layer (d/layer), and error estimates of the cross point determination ("±") obtained from the three-wavelength analysis in air for HSPC and SA monolayers deposited at two different surface pressures and for SA multilayers deposited at 45 mN/m.*

	d (nm)	"±" (nm)	*n* (780nm)	"±"	*dn/dλ* (1/nm)
HSPC					
1 LB 10 mN/m	3.4	0.10	1.404	0.001	0.0002
1 LB 30 mN/m	3.7	0.10	1.334	0.001	0.0002
SA					
1 LB 15 mN/m	2.4	0.10	1.584	0.5	0.0002
1 LB 45 mN/m	3.88	0.70	1.351	0.07	0.00015

SA 45 mN/m	*d* (nm)	"±" (nm)	*n* (780nm)	"±"	*dn/dλ* (1/nm)	*d*/layer (nm)
1 LB	3.88	0.70	1.351	0.07	0.00015	3.88
3 LB	8.8	0.20	1.471	0.0099	0.00015	2.94
5 LB	12.7	0.08	1.551	0.01	0.00015	2.54
7 LB	17.9	0.29	1.536	0.0049	0.00015	2.56
9 LB	21.9	0.09	1.571	0.00075	0.00015	2.43
11 LB	26.4	0.34	1.573	0.0078	0.00015	2.40
AVG of LB 5-11		**0.20**	**1.558**	**0.0057**		**2.48**
STD of LB 5-11		**0.136**	**0.018**	**0,004**		**0.08**

As can be seen in Figure 2A, all the *d–n* continuum solutions obtained by the three-wavelength analysis in air did not necessarily cross perfectly as would be expected from a purely theoretical point of view. The reason for this was most probably the fact that the wavelength pairs in the SPR instrument used in this study actually measure the sample layers from two physically different spots. To take this uncertainty into account in the analysis, the parameter values were estimated graphically as the average of the two cross points in the *d–n* plots for different laser pairs (Supporting Information, section SIV), and the difference between the average of the cross points and the actual cross points has been given as an error estimate ("±") in the values provided for each analysis in Tables 1 and 2.

The three-wavelength analysis of single deposited monolayers of both HSPC and SA shows relatively high uncertainty in the obtained values, and it seems to overemphasize the thickness of the first layer compared with the two-medium analysis (Tables 1 and 2). However, the individual thickness of SA mono- and multilayers plotted against the number of layers in Figure 3A show an excellent linear dependency, as well as a transition of the intersection with the *y* axis at 1.7 nm. The transition is of the same order of magnitude than the peak-to-peak roughness of the SPR sensor slide (2 nm, Supporting Information, section SV, Figure S5). The linear trend of the individual analyses of the SA mono- and multilayers confirms that the three-wavelength analysis behaves as expected

aside from the deviation in the first layer. The slope in the plot *d* vs number of layers of the SA mono- and multilayers gives a thickness of 2.24 nm/layer, while the three-wavelength analysis for SA multilayers with five or more deposited layers gives an average thickness of 2.48 ± 0.08 nm (Table 2). This is in good agreement with the value of 2.6 ± 0.05 nm obtained from the two-medium analysis (Table 1). The average layer thicknesses obtained from both the three-wavelength and two-medium analyses correspond well to the theoretical length of 2.5 nm of SA (Györvary, et al., 1996), the thickness of 2.66 ± 0.05 nm reported for Cd–stearate monolayers (Györvary, et al., 1996; Liang, et al., 2010), and the average thickness between 2.66 and 2.79 nm/layer obtained with ellipsometry for arachidic acid/uranyl acetate multilayers (Knobloch et al., 1997).

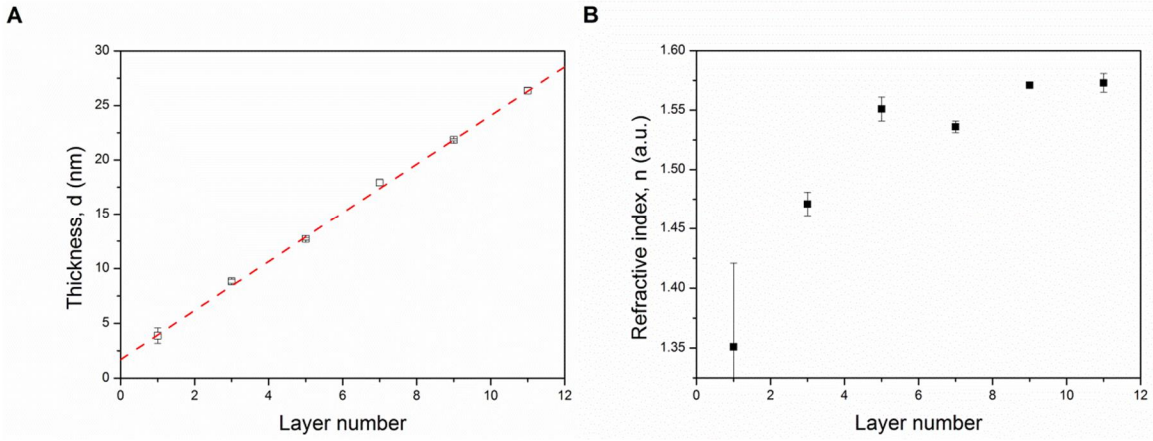

Figure 3. *Dependency of the (A) thickness (d) and (B) refractive index (n) on the number of layers of SA mono- and multilayers using the three-wavelength analysis. The thickness has a slope of 2.24 nm and a y intersection at 1.7 nm. The refractive index increases for the first deposited layers and levels out after five deposited layers. The error bars portray the uncertainty in the graphical determination of the intersection from the d–n plots.*

The individually extracted refractive indices from the three-wavelength analysis of the SA mono- and multilayer films plotted against the number of layers in Figure 3B show a nonlinear increasing trend in the refractive index values, which levels out after five deposited layers. This can be explained by a space-filling model where the first layers partially follow the roughness of the SPR sensor surface, and the further layers gradually bridge the gaps and finally start to deposit more smoothly with better organization and orientation. This probably also causes the slightly lower thickness of 2.24 nm/layer for the SA monolayers from the slope in Figure 3A compared with the individually determined average thicknesses from the three-wavelength and two-medium analyses.

The results of the three-wavelength analysis indicate that this approach detects the real thickness and the apparent (layer density dependent) refractive index of the ultrathin layers. The two-medium analysis, on the other hand, probes the real refractive index and the apparent thickness of the sample layers. This is surprising, as usually similar optical methods are thought to give an apparent thickness of a virtual full layer, which is of course always lower than the real layer thickness if there is any roughness present in the system.

The three-wavelength SPR analysis on the other hand uses multiple and simultaneous probing wavelengths which interact with the system slightly differently. This means that, although the dispersion coefficient has to be empirically determined, or assumed if only two wavelengths are used, the three-wavelength analysis actually determines the real layer thickness more accurately than the single-wavelength analysis where the refractive index has to be completely assumed or is taken from literature for bulk materials. Regarding the dispersion coefficient, it is obvious that the uranyl acetate counterion has a smaller effect on the refractive index of the condensed monolayers than the cadmium ions, which earlier showed a little bit large $dn/d\lambda$ value of 0.00463 for Cd–stearate (Liang, et al., 2010). The dispersion coefficients obtained for the ultrathin films in this study are close to those of other organic compounds, such as palmitic acid ($dn/d\lambda \approx 0.00005$) (Timmermans, 1965) and different polymers (0.00008–0.00003) (Kasarova et al., 2007), and those of the polyelectrolyte multilayers (see the SPR analysis of polyelectrolyte multilayers section below). This difference is probably due to the fact that the Cd–stearate monolayer is arranged in a hexagonal crystalline lattice, while uranyl acetate and other complex counterions result in a less ordered packing in the monolayers, and therefore, the optical properties of the layer are not affected by the crystallization.

5.4.3 Three-wavelength SPR analysis of polyelectrolyte multilayers

Two types of polyelectrolyte multilayers, i.e., PSS–PAH and HA–PLL, with different growth characteristics and properties were chosen for three-wavelength analysis. The thickness of the PSS–PAH polyelectrolyte multilayer is known to grow relatively slowly for each additional, but quite dense layers (Ladam et al., 1999). The thickness of the HA–PLL polyelectrolyte multilayer grows very fast, forming relatively low density layers compared with the PSS–PAH multilayer (Picart et al., 2001). As the PEM deposition can include tens or hundreds of layers, only a few layers close to the beginning of the depositions were characterized in detail. The actual three-wavelength characterization of the polyelectrolyte multilayers followed the same procedure as described earlier for the LB deposited SA and HSPC mono- and multilayers, with the exception that the SPR full angle spectra of the polyelectrolyte multilayers were measured in liquid media, not in air as the LB films. Table 3 summarizes the results obtained for the thicknesses and refractive indices of 3, 5, and 10 bilayers of PSS–PAH and 2 and 5 bilayers of HA–PLL multilayers.

The characteristic behavior of the two different polyelectrolyte multilayers is very clear, i.e., the thickness per layer of the HA–PLL multilayer is always at least 4 times larger than that of the PSS–PAH multilayer and already reaches a thickness of ca. 67 nm after five deposited bilayers. The thickness per layer for both polyelectrolyte multilayers also increases slightly with the number of layers, which is often the case because the first few layers during the buildup usually grow in a nonlinear fashion (Ladam, et al., 1999; Picart, et al., 2001). Furthermore, the refractive indices obtained for the HA–PLL multilayers are clearly smaller than for the PSS–PAH multilayers. The results from the three-wavelength analysis are in good agreement with the facts that HA–PLL polyelectrolyte multilayers exhibit exponential growth characteristics, forming low density layers (Picart, et al.,

2001). PSS–PAH has been reported to exhibit a linear growth pattern with high–density layers (Ladam, et al., 1999). The thickness values obtained from the three-wavelength analysis correlate very well with previously reported thickness values of 4 nm/layer for PSS–PAH, especially when taking into account that the concentration used for the polyelectrolyte multilayer buildup in the present study was 1/10 of the concentration normally used (Ladam, et al., 1999).

Table 3. *Thickness (d), refractive index (n), dispersion (dn/dλ), thickness per layer (d/layer), and error estimates ("±") obtained from the three-wavelength analysis for PSS–PAH and HA–PLL polyelectrolyte multilayer films.*

	No. of bilayers	*d* (nm)	"±" (nm)	*n* (780nm)	"±"	*dn/dλ* (1/nm)	*d*/layer (nm)
PSS:PAH	3	9.2	0.5	1.495	0.010	0.00003	3.07
	5	16.8	0.5	1.481	0.005	0.00003	3.36
	10	35.0	1	1.470	0.005	0.00002	3.50
	120 (783 nm)	400.0		1.501			3.33
	120 (655 nm)	404.0		1.503			3.37
HA:PLL	2	25.2	3	1.356	0.001	0.00003	12.61
	5	67.1	3	1.351	0.001	0.00005	13.42

The results from the three-wavelength analysis for both the LB films and the polyelectrolyte multilayers indicate that the SPR technique can effectively be utilized for characterizing optical properties of ultrathin films without previous knowledge of the system. While the examples in this study still show some uncertainty in the results, the three-wavelength analysis approach is rather easy to perform, while the level of the uncertainties can be easily estimated and evaluated for acceptance. Critical assessment of the limits of detection and accuracy of the three-wavelength SPR analysis in this study compared with established methods such as ellipsometry or SE, appeared to be difficult because of insufficient literature available. However, a careful evaluation of published results of ultrathin film measurements indicates that the SPR three-wavelength analysis approach is able to characterize thinner layers with less uncertainty in thickness and refractive index values. Additionally, the ability of the three-wavelength SPR analysis to determine the real thickness instead of apparent thickness obtained from single-wavelength and two-medium analysis could be extremely beneficial in the future when characterizing ultrathin films in the range of a few to tens of nanometers.

Schoch and Lim recently published a study (Schoch & Lim, 2013) where SPR was used for analyzing the layer thickness by utilizing a noninteracting sample which probes the excluded volume created by the layers on the sensor surface. Their study showed a capability of determining the real thickness and apparent (layer density dependent) refractive index of thin organic layers similar to that of the three-wavelength analysis approach presented in the current study. As stated by Schoch and Lim, self-assembly of polymers into loose solvated polymer brushes tends to occupy a space related to their hydrodynamic size, and use of the bulk material refractive index is clearly incorrect for

such systems. Therefore, any approach that can take into account the material density related refractive index is always more correct than using bulk refractive indices. The benefit of their approach is that it does not need any knowledge about the underlying optical system (sensor structure), but it is a relative measurement, unlike our approach. However, the approach of Schoch and Lim requires a lot of knowledge about the sample layer properties, reference cells, and a noninteracting probe sample, which actually makes it quite a tedious measurement to perform in practice. The analysis approach presented in the current study does not need any of these. Furthermore, the molecular probes approach utilized by Schoch and Lim is suitable mostly for liquid-phase measurements, and there will always be an issue of finding completely noninteracting samples with sufficiently high refractive index. After all, most noninteracting samples, such as polysaccharides and polyethylene glycol, are materials with extremely low refractive index, which produce low signal responses in SPR. In addition, Schoch and Lim claim that their approach bypasses the refractive index constraint in SPR. However, one of the most important properties of organic layers is the real refractive index, which should not be neglected, especially for layer-related optical applications. From another point of view, the refractive index itself reflects the integrity of the deposited layers, because the refractive index is sensitive to the molecular packing density of the sample layers.

5.4.4 SPR analysis of relatively thick films

It is possible to build very thick and dense layers with polyelectrolytes under proper experimental conditions and by the choice of the polyelectrolytes used for the layer buildup. It has been shown that the PSS–PAH polyelectrolyte pair can be used to prepare polyelectrolyte multilayers consisting of hundreds of layers, partly because of its ability to form densely packed layers with linear growth characteristics (Ladam, et al., 1999). Figure 4A shows a time sensogram of the change in SPR minimum angle measured with a 655 nm laser wavelength for 110–120 PSS–PAH bilayers. Every single peak in the time sensogram represents an injection of an oppositely charged polyelectrolyte followed by a rinsing period. The time sensogram clearly shows that the signal from the growing PSS–PAH polyelectrolyte multilayer was still behaving in a linear fashion when the SPR waveguide mode minimum was monitored. It is also clear from the sensogram that the SPR waveguide mode is still sensitive enough to measure the addition of nanometer-scale layers on top of the waveguide layer, and not only for detecting changes in the layer density in the form of sample absorbing into the waveguide as shown earlier (Aulasevich, et al., 2009; Baba, et al., 2010).

Interestingly, the PSS–PAH polyelectrolyte multilayer induced an SPR waveguide when approximately 100 bilayers had been deposited, which could be seen as a dramatic decrease in the SPR peak intensity, as well as the appearance of an additional peak at lower angles compared with the main SPR peak (Figure 4B). The waveguide formed by the PSS–PAH polyelectrolyte multilayer also showed a significant wavelength dependency (Figure 4B and C). The resonance peak with 655 nm has shifted to sufficiently high angles to be clearly distinguishable from the additional waveguide peak

appearing in the critical angle region of the SPR spectrum (Figure 4B). The spectrum measured with 782 nm for the same layer thickness shows that the main resonance peak and the waveguide peak in the critical angle region can still be detected as an overlapping optical phenomenon (Figure 4C). However, an overlapping critical angle and the main resonance peak can still be used to calculate the thickness of the layer.

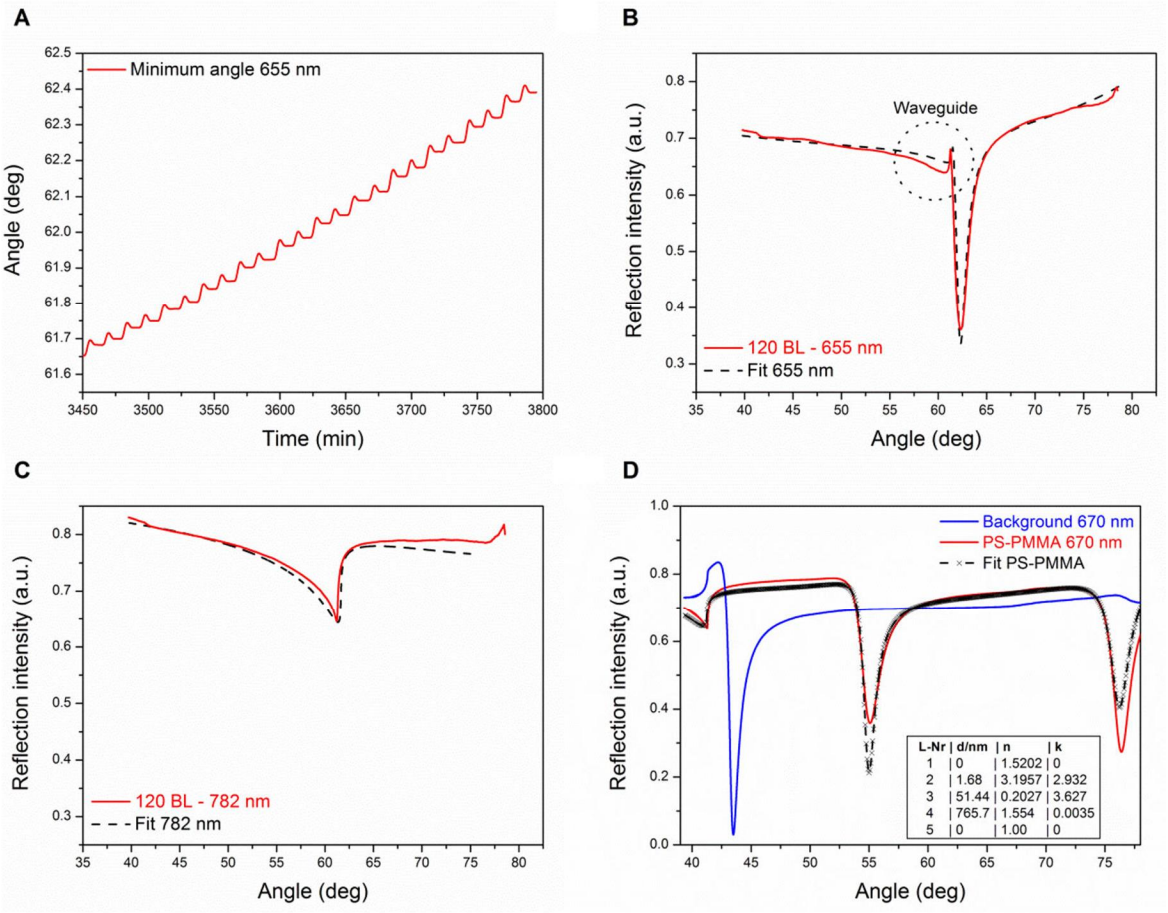

Figure 4. *(A) Time sensogram of the SPR minimum angle with λ = 655 nm for 110–120 bilayers: SPR scans (solid red lines) and Winspall fits (dashed black line) for 120 bilayers of PSS–PAH with (B) λ = 655 nm and (C) λ = 782 nm. (D) SPR scan of a spin-coated PS–PMMA copolymer layer in air with λ = 670 nm (red solid line) and Winspall fit (black times signs, dashed black line) with a pure gold background (blue solid line). Inset: optical parameters used for the Winspall fit (1 = prism, 2 = chromium, 3 = gold, 4 = PS–PMMA layer, 5 = air).*

Actually, whenever a layer is thick enough to induce an SPR waveguide mode, there is only one solution for the real thickness and the apparent (layer density dependent) refractive index, which means that there is no need to assume one or the other. The thicknesses and refractive indices obtained by fitting the SPR full angle spectrum measured for the 120 bilayer thick PSS–PAH multilayer with two wavelengths of 655 and 782 nm were 404 and 400 nm and 1.503 and 1.501, respectively (Table 3). The thickness per layer is also in good agreement with the values obtained for the PSS–PAH multilayers

consisting of 5 and 10 bilayers. The refractive index obtained for the thick PSS–PAH multilayers was on the other hand slightly larger than the refractive indices obtained for 5 and 10 bilayers. This is a consequence of the fact that polyelectrolyte multilayers forming dense layers tend to compact their structure with increasing layer number by excluding excess water from the layer structure (Ladam, et al., 1999). The resonant waveguide peaks actually retain the thickness development after its formation, which is evident from the waveguide node minimum shift (Figure 4A). This makes it possible to use them to characterize both the thickness and refractive index of thick organic layers or as a detection element in biosensor assays, as previously shown in the literature (Aulasevich, et al., 2009; Lévesque, et al., 1994).

Finally, it was also possible to measure waveguides deposited *ex situ* in a fashion similar to that for the *in situ* prepared waveguides of PSS–PAH multilayers. This allows for the determination of the real thickness and apparent (layer density dependent) refractive index for other types of relatively thick layers as well. Figure 4D demonstrates this for a spin-coated PS–PMMA copolymer layer. The SPR full angle scan measured in air with 670 nm now shows all together three distinct peaks caused by the thick spin-coated PS–PMMA layer. The thickness and the refractive index determined for the PS–PMMA layer were 765.7 nm and 1.554, respectively (inset table in Figure 4D). The refractive index of the PS–PMMA layer is in very good agreement with the weighted average of the refractive indexes of pure PS (1.58425 at 670 nm) and PMMA (1.48741 at 670 nm), considering that PS–PMMA contains 24% PMMA, i.e., 1.561. The slight nonzero imaginary part in the refractive index for the PS–PMMA layer indicates that there is some loss of light in the material, which may occur, for example, when light is reflected from an inhomogeneous surface or cracks in the spin-coated film.

5.5 Conclusions

A three-wavelength angular-scanning surface plasmon resonance based analysis has been demonstrated to be an efficient approach for determining ultrathin films thicknesses within the range that is difficult to access with other methods. The applicability of the multi-parametric SPR (MP-SPR) for measuring the film thickness and optical property determination with relatively thick films using SPR waveguide modes was also demonstrated. These results can be utilized in characterizing and building different detection platforms for sensor development, life sciences, and drug development, as well as for obtaining fundamental information about the optical properties of different biological and organic systems. A one-instrument approach for accurately characterizing such layers without the help of any other instrument was successfully presented in this work. A critical assessment of the limits of detection and accuracy of the three-wavelength SPR analysis compared to the established ellipsometry or SE methods could not be done due to insufficient literature in the area. A careful evaluation of the few publications with results on ultrathin film measurements indicates, however, that the SPR three-wavelength analysis approach is able to characterize thin layers with good accuracy for the resulting thickness and refractive index values.

The ability to perform SPR measurements at multiple wavelengths allows both for an accurate characterization of ultrathin films and also for characterizing relatively thick organic layers in the micrometer range. By proper wavelength selection in the future, it should also be possible to almost completely cover the SPR "blind spot", in which the SPR angle is too high to be modeled, but the waveguide resonance mode has not yet been reached.

Acknowledgements

This research was funded by the Academy of Finland (Project Nos. 137053 and 1140980). N.G. thanks the Foundation of Anja and Mirja Tissari from the Finnish Cultural Foundation (Suomen Kulttuurirahasto). We also express special thanks to Jaakko Välimaa from KSV-NIMA for collaborating with the PM-IRRAS measurements.

5.6 References

Albers, W. M., & Vikholm-Lundin, I. (2011). Surface Plasmon Resonance on Nanoscale Organic Films. In *Nano-Bio-Sensing,* Carrara, S., Ed.; Springer: New York, London, 83-125.

Aulasevich, A., Roskamp, R. F., Jonas, U., Menges, B., Dostalek, J., & Knoll, W. (2009). Optical waveguide spectroscopy for the investigation of protein-functionalized hydrogel films. *Macromol Rapid Commun, 30*(9-10), 872-877.

Azzam R. M. A, B., N.M. (1987). *Ellipsometry and Polarized light*. Amsterdam: Elsevier.

Baba, A., Taranekar, P., Ponnapati, R. R., Knoll, W., & Advincula, R. C. (2010). Electrochemical surface plasmon resonance and waveguide-enhanced glucose biosensing with N-alkylaminated polypyrrole/glucose oxidase multilayers. *ACS Appl Mater Interfaces, 2*(8), 2347-2354.

Bandey, H. L., Martin, S. J., Cernosek, R. W., & Hillman, A. R. (1999). Modeling the Responses of Thickness-Shear Mode Resonators under Various Loading Conditions. *Analytical Chemistry, 71*(11), 2205-2214.

Buffeteau, T., Desbat, B., & Turlet, J. M. (1991). Polarization Modulation FT-IR Spectroscopy of Surfaces and Ultra-thin Films: Experimental Procedure and Quantitative Analysis. *Appl. Spectrosc., 45*(3), 380-389.

Buttry, D. A., & Ward, M. D. (1992). Measurement of interfacial processes at electrode surfaces with the electrochemical quartz crystal microbalance. *Chem Rev, 92*(6), 1355-1379.

Campbell, N. A. (2009). *Biology* (8th ed.). Sydney: Pearson/Benjamin Cummings.

Castellana, E. T., & Cremer, P. S. (2006). Solid supported lipid bilayers: From biophysical studies to sensor design. *Surface Science Reports, 61*(10), 429-444.

CRCnetBase. (2012). *CRC Handbook of Chemistry and Physics* (92 ed.): Taylor and Francis group.

Gorwyn, D., & Barnes, G. T. (1990). Interactions of large ions with phospholipid monolayers. *Langmuir, 6*(1), 222-230.

Grassi, J. H., & Georgiadis, R. M. (1999). Temperature-Dependent Refractive Index Determination from Critical Angle Measurements: Implications for Quantitative SPR Sensing. *Analytical Chemistry, 71*(19), 4392-4396.

Györvary, E., Peltonen, J., Lindén, M., & Rosenholm, J. B. (1996). Reorganization of metal stearate LB films studied by AFM and contact angle measurements. *Thin Solid Films, 284–285*(0), 368-372.

Hansma, H. G., & Pietrasanta, L. (1998). Atomic force microscopy and other scanning probe microscopies. *Current Opinion in Chemical Biology, 2*(5), 579-584.

Hilfiker, J. N., Singh, N., Tiwald, T., Convey, D., Smith, S. M., Baker, J. H., et al. (2008). Survey of methods to characterize thin absorbing films with Spectroscopic Ellipsometry. *Thin Solid Films, 516*(22), 7979-7989.

Homola, J., Yee, S. S., & Gauglitz, G. (1999). Surface plasmon resonance sensors: review. *Sensors and Actuators B: Chemical, 54*(1–2), 3-15.

Kasarova, S. N., Sultanova, N. G., Ivanov, C. D., & Nikolov, I. D. (2007). Analysis of the dispersion of optical plastic materials. *Optical Materials, 29*(11), 1481-1490.

Knobloch, H., Peñacorada, F., & Brehmer, L. (1997). Ellipsometric studies on uranyl arachidate Langmuir-Blodgett films. *Thin Solid Films, 295*(1–2), 210-213.

Knoll, W. (2013). http://www2.mpip-mainz.mpg.de/groups/knoll/software. Retrieved May, 2013

Ladam, G., Schaad, P., Voegel, J. C., Schaaf, P., Decher, G., & Cuisinier, F. (1999). In Situ Determination of the Structural Properties of Initially Deposited Polyelectrolyte Multilayers. *Langmuir, 16*(3), 1249-1255.

Lévesque, L., Paton, B. E., & Payne, S. H. (1994). Precise thickness and refractive index determination of polyimide films using attenuated total reflection. *Appl. Opt., 33*(34), 8036-8040.

Liang, H., Miranto, H., Granqvist, N., Sadowski, J. W., Viitala, T., Wang, B., et al. (2010). Surface plasmon resonance instrument as a refractometer for liquids and ultrathin films. *Sensors and Actuators B: Chemical, 149*(1), 212-220.

Linden, M., & Rosenholm, J. B. (1995). Influence of Multivalent Metal Ions on the Monolayer and Multilayer Properties of Some Unsaturated Fatty Acids. *Langmuir, 11*(11), 4499-4504.

Peltonen, J., Linden, M., Fagerholm, H., Györvary, E., & Eriksson, F. (1994). The influence of multivalent salts on the processability of a stearic acid monolayer: a stability, electron spectroscopy for chemical analysis and atomic force microscopy study. *Thin Solid Films, 242*(1–2), 88-91.

Peterlinz, K. A., & Georgiadis, R. (1996). Two-color approach for determination of thickness and dielectric constant of thin films using surface plasmon resonance spectroscopy. *Optics Communications, 130*(4–6), 260-266.

Picart, C., Lavalle, P., Hubert, P., Cuisinier, F. J. G., Decher, G., Schaaf, P., et al. (2001). Buildup Mechanism for Poly(l-lysine)/Hyaluronic Acid Films onto a Solid Surface. *Langmuir, 17*(23), 7414-7424.

Rodenhausen, K. B., Kasputis, T., Pannier, A. K., Gerasimov, J. Y., Lai, R. Y., Solinsky, M., et al. (2011). Combined optical and acoustical method for determination of thickness and porosity of transparent organic layers below the ultra-thin film limit. *Rev Sci Instrum, 82*(10), 103111.

Rossi, C., & Chopineau, J. (2007). Biomimetic tethered lipid membranes designed for membrane-protein interaction studies. *Eur Biophys J, 36*(8), 955-965.

Sadowski, J. W., Korhonen, I. K., & Peltonen, J. P. (1995). Characterization of thin films and their structures in surface plasmon resonance measurements. *Optical Engineering, 34*(9), 2581-2586.

Santos, N. C., & Castanho, M. A. R. B. (2004). An overview of the biophysical applications of atomic force microscopy. *Biophysical Chemistry, 107*(2), 133-149.
Schasfoort R. B. M, T. A. J. (2008). *Handbook of Surface Plasmon Resonance*. Cambridge,UK: RSC.
Schoch, R. L., & Lim, R. Y. H. (2013). Non-Interacting Molecules as Innate Structural Probes in Surface Plasmon Resonance. *Langmuir, 29*(12), 4068-4076.
Timmermans, J. (1965). *Physico-chemical constants of pure organic compounds*: Elsevier.
Tkachenko, N. V., Grandell, D., Ikonen, M., Jutila, A., Moritz, V., & Lemmetyinen, H. (1993). Excitation energy relaxation in chlorophyll a Langmuir-Blodgett multilayer films. 254-261.
Tonova, D., Depas, M., & Vanhellemont, J. (1996). Interpretation of spectroscopic ellipsometry measurements of ultrathin dielectric layers on silicon: Impact of accuracy of the silicon optical constants. *Thin Solid Films, 288*(1-2), 64-68.
Ververis, C., Georghiou, K., Christodoulakis, N., Santas, P., & Santas, R. (2004). Fiber dimensions, lignin and cellulose content of various plant materials and their suitability for paper production. *Industrial Crops and Products, 19*(3), 245-254.
Viitala, T., & Peltonen, J. (1999). UV-Induced Reaction Kinetics of Dilinoleoylphosphatidylethanolamine Monolayers. *Biophys J, 76*(5), 2803-2813.
You, H. X., & Lowe, C. R. (1996). Progress in the application of scanning probe microscopy to biology. *Current Opinion in Biotechnology, 7*(1), 78-84.
Zhou, M., Otomo, A., Yokoyama, S., & Mashiko, S. (2001). Estimation of organic molecular film structures using surface–plasmon resonance spectroscopy. *Thin Solid Films, 393*(1–2), 114-118.

Appendix: Supporting information

SI. Theory of SPR

Surface plasmons are particle waves of the free electron plasma on a metal surface, which can be excited by p-polarized light under the resonance condition (Figure S1). A theoretical mathematical description for the resonance condition can be obtained by solving the Maxwell equations for a multilayer optical system (Albers & Vikholm-Lundin, 2011), which provides the following mathematical solution for the resonance condition for the Kretschmann configuration (shown in Figure S1):

(S1) $$\frac{\omega}{c}\sqrt{\varepsilon_0}sin\theta = \frac{\omega}{c}\sqrt{\frac{\varepsilon_1\varepsilon_2}{\varepsilon_1+\varepsilon_2}}$$

where ω is the angular frequency of light, c is speed of light in vacuum, and ε_0, ε_1 and ε_2 are the permittivity of the prism, SPR metal layer and the adjacent medium, respectively. The permittivity and refractive index of materials can be used in their complex forms:

(S2) $\varepsilon = \varepsilon' + i\varepsilon''$

(S3) $\tilde{n} = n - ik \ ; \ (k > 0)$

where ε, ε' and ε'' are the complex permittivity, real- and imaginary part of the complex permittivity, respectively. $\tilde{n}$, n and k are the complex refractive index, real- and imaginary part of the complex refractive index, respectively. Permittivity and refractive index have the following relationship:

(S4) $\tilde{n} = \sqrt{\varepsilon}$

(S5) $|\varepsilon| = n^2 + k^2$

where $|\varepsilon|$ is the modulus of the complex permittivity. A general solution for a multilayered system linked to measurable or controllable variables is given with a transfer matrix formalism of 2×2 matrices. The overall formalism has already been published several times, and it is not in the scope of this article. (Sadowski et al., 1995; Albers & Vikholm-Lundin, 2011) In practice it is solved with mathematical fitting tools, or with dedicated software tools, such as Winspall (Knoll, 2013).

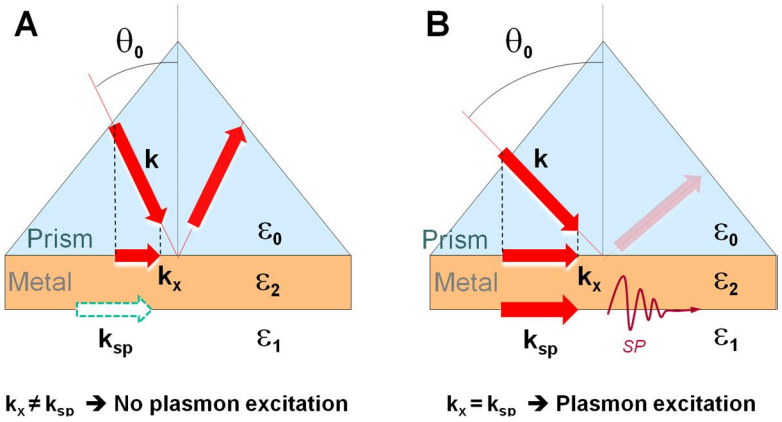

Figure S1. *Schematic representation of the Kretchmann configuration of the SPR used in the study. A) When the projected wave vector of the incident light do not match the wave vector of surface plasmons no excitation occurs. B) At a certain incident light angle the projected wave vector of the incident light matches the wave vector of surface plasmons, which is dependent on the wavelength of light used and the dielectric properties of the prism (ε_0), metal layer (ε_2) and the surrounding medium (ε_1).*

SII. Refractive index linearity approximation

The so called Cauchy materials, such as most polymers and metal oxides, have a non-linear dependency between wavelength and the refractive index. However, in a relatively small wavelength region this dependency can be assumed to be linear, which is apparent from

Figure S2. Figure S2 shows the linear regression fit to the refractive index (n) for different materials obtained from Kasarova *et al* (Kasarova et al., 2007). The triangles in Figure S2 denote the measurement wavelengths used in the SPR analysis. As can clearly be seen from Figure S2, the wavelength dependency of the refractive index in the red-visible light region can be approximated as the residual of the linear fit, which is ca. 2% (R-value). Visual inspection also confirms that the linear fit describes the relevant region with a good correlation.

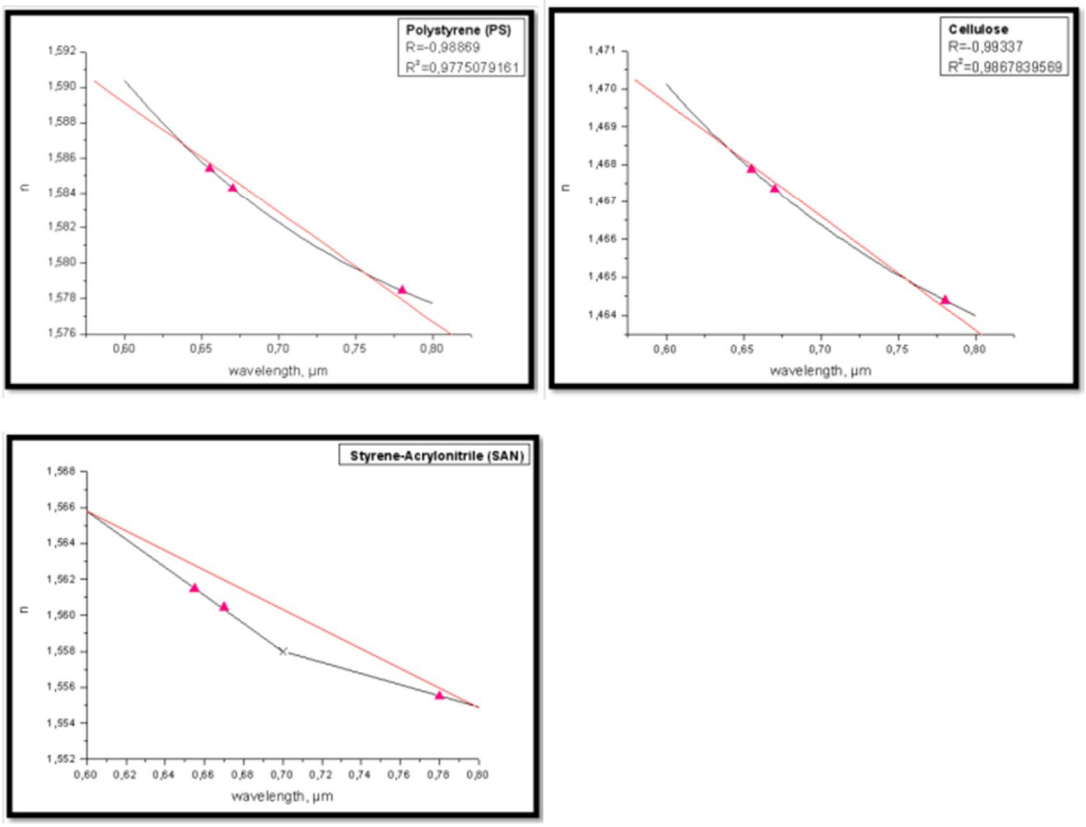

Figure S2. *The wavelength dependency of refractive index for three different polymer materials. The red lines are linear fits to the data in the wavelength region between 0.6 – 0.8 µm. The colored triangles emphasize the wavelengths used in the SPR analysis in the current study.*

SIII. Langmuir and Langmuir-Blodgett technique and PM-IRRAS characterization of monolayers

In this study we utilized the Langmuir-Blodgett technique for preparing well defined thin organic films with controlled number of layers in order to clarify how well a three-wavelength SPR analysis could be used for simultaneous determination of the thickness and refractive index of ultrathin films in the thickness range of 1-10 nm. The Langmuir-Blodgett (LB) technique is a well-established method that enables controlled depositions of mono- and multilayers of a water insoluble organic amphiphilic substance floating on an air-water interface (Blodgett & Langmuir, 1937). Deposition takes place by single or

repeated immersions of a solid substrate through the floating monolayer at a controlled molecular packing density. Thus, the LB technique allows to precisely controlling the number of deposited layers and consequently the thickness of thin organic amphiphilic sample layers on solid substrates. Often multivalent counter ions are used in the subphase beneath the floating monolayer in order to facilitate the deposition of good quality mono- and multilayers (Györvary et al., 1996; Knobloch et al., 1997; Linden & Rosenholm, 1995; Peltonen et al., 1994). Figures S3A and S3B show the compression isotherms of SA and HSPC measured on pure water and UAc containing subphases. The discussion of these results can be found in the main manuscript text.

PM-IRRAS measurements.

PM-IRRAS spectra measured for organic ultrathin films deposited on IR reflective substrates have proven to provide valuable information about the orientation, conformation and structural order of the molecules in the sample layer, even for single monolayers (Buffeteau et al., 1991; Pavinatto et al., 2009). These properties on the other hand have an influence on the thickness and optical properties of ultrathin organic layers determined by optical techniques, such as SPR, especially in the case of the first deposited layers. In order to detect any clear differences in orientation or structural order in the deposited monolayers of SA or HSPC we collected PM-IRRAS spectra for monolayers deposited onto SPR sensor slides from UAc containing subphases at two different surface pressures (Figure S3C and S3D).

The PM-IRRAS spectra for the C-H stretching mode region measured for both SA and HSPC monolayers show bands at 2965 cm^{-1}, 2920 cm^{-1}, 2880 cm^{-1} and 2850 cm^{-1}, which are assigned to the CH_3 asymmetric stretch, CH_2 asymmetric stretch, CH_3 symmetric stretch and CH_2 symmetric stretch vibrations, respectively (Blume, 1996; Rabolt et al., 1983). For the SA monolayer an increase in the surface pressure, i.e. an increase in packing density, shifts the IR band at 2920 cm^{-1} slightly towards lower wavenumbers, whereas the band at 2880 cm^{-1} grew more discrete and shifted to slightly higher wavenumbers. These changes in the PM-IRRAS spectra indicates that the SA monolayer possess an increasing number of trans conformers along the hydrocarbon chain for the monolayer deposited at higher surface pressure (Dicko et al., 1998). This correlates with an increasing order in the SA monolayer at higher surface pressure, which should be reflected in the optical properties of the monolayer. In the case of the HSPC monolayer the PM-IRRAS spectra did not show any shift for the band at 2920 cm^{-1}, whereas the bands at 2965 cm^{-1}, 2880 cm^{-1} and 2850 cm^{-1} shifted to slightly higher wavenumbers. This indicates that the molecules in the HSPC monolayer obtain a slightly more perpendicular orientation against the SPR sensor slide surface without an increase in order when deposited at higher surface pressure. The isotherm behavior of the HSPC and SA monolayers also supports this, as no clear liquid-solid transformation can be seen for the HSPC monolayer, while the SA monolayer exhibits this transition at 40 mN/m.

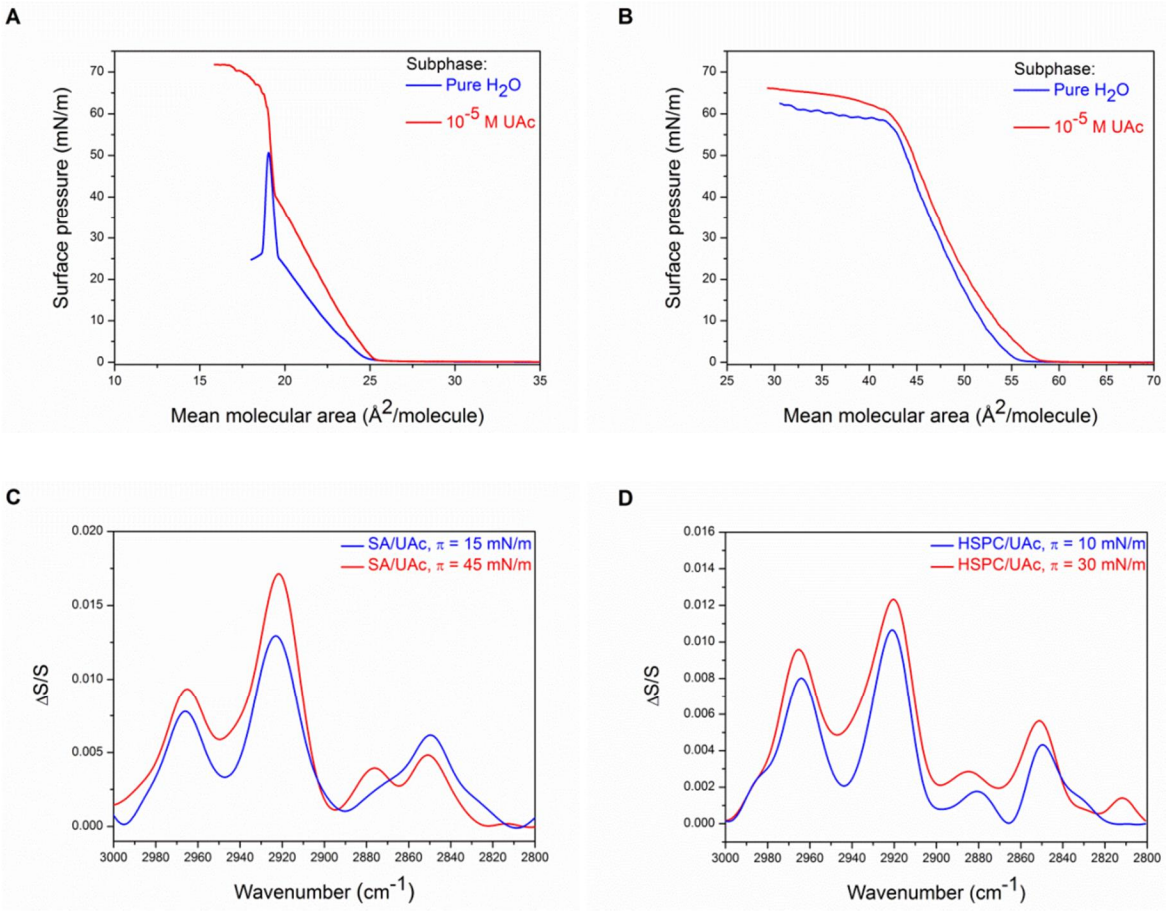

Figure S3. *Compression isotherms for A) SA and B) HSPC monolayers on pure water (blue solid lines) and 10^{-5} UAc subphases (red solid lines). PM-IRRAS spectra of the CH-region for C) SA and D) HSPC monolayers deposited on the SPR sensor slide at different surface pressures; low surface pressure (blue solid lines) and high surface pressure (red solid lines).*

SIV. Three wavelength analysis approach

The thickness (d) versus refractive index (n) continuum solutions for the sample layer deposited on the SPR sensor slide were obtained by using Winspall (Knoll, 2013) to fit the SPR full angle scan measured at a specific laser wavelength. The optical properties of the sample layer were then fitted by fixing the previously optimized optical properties for the pure SPR sensor slide, and then keeping n constant while fitting d for the sample layer. This was then repeated for n-values between 1.2-1.6 with an increment of 0.2. The d-n continuum solutions obtained by this procedure for a HSPC monolayer are shown in Figure S4A for the three different wavelengths used in this study. Hereafter, the d-n curve for 655 nm was kept in place and the d-n curves for all the other wavelengths were shifted by varying the $dn/d\lambda$ value manually so that the two cross-points for the different laser pairs were as close as possible to each other, both in the d and n direction (Figure S4B). The positions of cross-point #1 and cross-point #2 were then used to calculate the average

cross-point, which then provided d and n for the sample layer in question. The difference between the average cross point and the actual cross points (i.e. cross-point #1 and cross-point #2) was then taken as the error estimate ("±") in the values provided for each analysis.

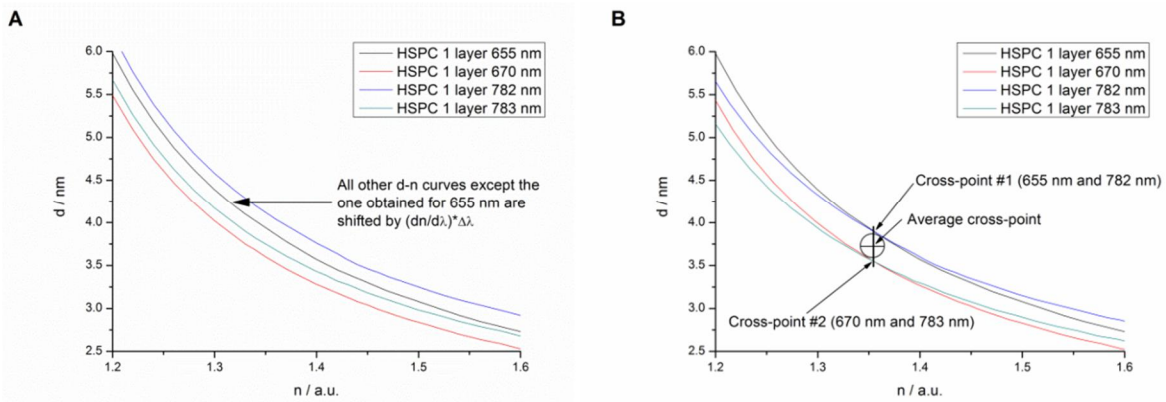

Figure S4. *A) The d-n continuum solutions obtained at different SPR laser wavelengths for a HSPC monolayer deposited at 30 mN/m. B) Illustration of the optimal cross-points found after shifting the d-n continuum solutions for 670 nm, 783 nm and 782 nm by $dn/d\lambda = 0.0002 \times \Delta\lambda$ with respect to d-n continuum solution for 655 nm. The circle in B) represents the error estimate form the cross-point analysis.*

SV. SPR sensor roughness

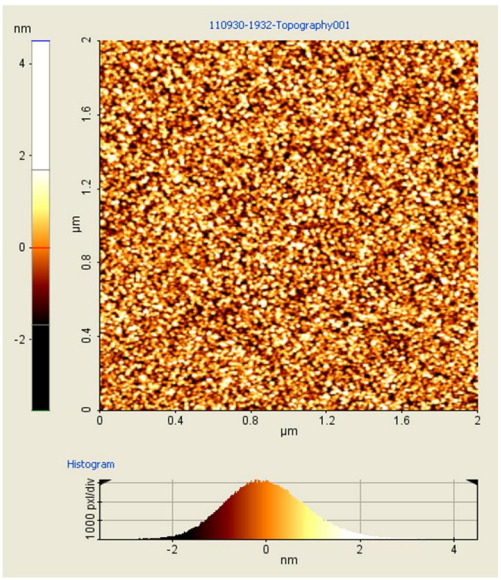

Figure S5. *AFM image and height histogram of a pure SPR sensor slide surface.*

The roughness of the SPR sensors slide is given by the manufacturer. The roughness has been measured using AFM analysis. R_q average of 5 independent measurements was

0.890 nm. It is apparent from the Gaussian-shaped thickness population in Figure S5 that approximately 70-90% of the thickness is within ±1 nm from the average thickness.

References

Albers, W. M., & Vikholm-Lundin, I. (2011). Surface Plasmon Resonance on Nanoscale Organic Films. In *Nano-Bio-Sensing,* Carrara, S., Ed.; Springer: New York, London, 83-125.

Blodgett, K. B., & Langmuir, I. (1937). Built-Up Films of Barium Stearate and Their Optical Properties. *Physical Review, 51*(11), 964-982.

Blume, A. (1996). Properties of lipid vesicles: FT-IR spectroscopy and fluorescence probe studies. *Current Opinion in Colloid & Interface Science, 1*(1), 64-77.

Buffeteau, T., Desbat, B., & Turlet, J. M. (1991). Polarization Modulation FT-IR Spectroscopy of Surfaces and Ultra-thin Films: Experimental Procedure and Quantitative Analysis. *Appl. Spectrosc., 45*(3), 380-389.

Dicko, A., Bourque, H., & Pézolet, M. (1998). Study by infrared spectroscopy of the conformation of dipalmitoylphosphatidylglycerol monolayers at the air–water interface and transferred on solid substrates. *Chemistry and Physics of Lipids, 96*(1–2), 125-139.

Györvary, E., Peltonen, J., Lindén, M., & Rosenholm, J. B. (1996). Reorganization of metal stearate LB films studied by AFM and contact angle measurements. *Thin Solid Films, 284–285*(0), 368-372.

Kasarova, S. N., Sultanova, N. G., Ivanov, C. D., & Nikolov, I. D. (2007). Analysis of the dispersion of optical plastic materials. *Optical Materials, 29*(11), 1481-1490.

Knobloch, H., Peñacorada, F., & Brehmer, L. (1997). Ellipsometric studies on uranyl arachidate Langmuir-Blodgett films. *Thin Solid Films, 295*(1–2), 210-213.

Knoll, W. (2013). http://www2.mpip-mainz.mpg.de/groups/knoll/software. Retrieved May, 2013

Linden, M., & Rosenholm, J. B. (1995). Influence of Multivalent Metal Ions on the Monolayer and Multilayer Properties of Some Unsaturated Fatty Acids. *Langmuir, 11*(11), 4499-4504.

Pavinatto, F. J., Pacholatti, C. P., Montanha, E. r. A., Caseli, L., Silva, H. S., Miranda, P. B., et al. (2009). Cholesterol Mediates Chitosan Activity on Phospholipid Monolayers and Langmuir−Blodgett Films. *Langmuir, 25*(17), 10051-10061.

Peltonen, J., Linden, M., Fagerholm, H., Györvary, E., & Eriksson, F. (1994). The influence of multivalent salts on the processability of a stearic acid monolayer: a stability, electron spectroscopy for chemical analysis and atomic force microscopy study. *Thin Solid Films, 242*(1–2), 88-91.

Rabolt, J. F., Burns, F. C., Schlotter, N. E., & Swalen, J. D. (1983). Anisotropic orientation in molecular monolayers by infrared spectroscopy. *The Journal of Chemical Physics, 78*(2), 946-952.

Sadowski, J. W., Korhonen, I. K., & Peltonen, J. P. (1995). Characterization of thin films and their structures in surface plasmon resonance measurements. *Optical Engineering, 34*(9), 2581-2586.

6 FLUID DYNAMICS MODELING FOR SYNCHRONIZING SURFACE PLASMON RESONANCE AND QUARTZ CRYSTAL MICROBALANCE USED FOR BIOMOLECULAR AND TARGETED DRUG DELIVERY STUDIES*

Abstract:

We have used computational fluid dynamics modeling (CFD) to synchronize the flow conditions in the flow channels of two complementary surface-sensitive characterization techniques, surface plasmon resonance (SPR) and quartz crystal microbalance (QCM). Since the footprint of the flow channels is specified by their function, the flow behaviour can only be varied either by altering the height of the flow channel, or altering the flow rate. The relevant quantity that must be calibrated is the shear stress on the measurement surface (center and bottom) of the flow channel. Our CFD modeling shows that the flow behaviour is in the Stokes flow regime. We were thus able to generate a scaling expression with parameters for flow rate and flow channel height for the two devices:

$$f_{QCM} = 2.64 f_{SPR} (\frac{h_{QCM}}{h_{SPR}})^2$$

where f_{QCM} and f_{SPR} are the flow rates in the SPR and QCM flow channels, respectively, and h_{QCM}/h_{SPR} is the ratio of the heights of the two channels. With the combined use of commercially available SPR and QCM, the calibration procedure is further verified by the interaction of a biomolecule (streptavidin) and a nanoparticle drug delivery (biotinylated liposome) with their individual receptor immobilized surface.

*Adapted from (Reprinted with permission from Elsevier): Tapani Viitala, Huamin Liang, Mayur Gupta, Thomas Zwinger, Marjo Yliperttula, Alex Bunker: Fluid dynamics modeling for synchronizing surface plasmon resonance and quartz crystal microbalance as tools for biomolecular and targeted drug delivery studies. Journal of Colloid and Interface Science 378: 251-259, 2012.

6.1 Introduction

The targeting of nanoparticle drug delivery to their cellular targets is anticipated to improve dramatically the intracellular delivery efficacy of drugs and genes with a narrow therapeutic window and low cell membrane permeability. Successful targeting depends on the selective binding of targeting ligands on the surface of the nanoparticle to receptors expressed in the membranes of target cells. The potency of a therapeutic product is often demonstrated by testing its biological activity, using cell cultures, tissue preparations, or entire animals. These biological assays are not as precise and reproducible as physicochemical methods for the determination of specific targeting and binding events. While it is widely accepted that blood stream hydrodynamics is an important pharmacokinetic factor, its study has been limited, as a result of the difficulty of both measuring this effect and of developing a comprehensive understanding of the results of these measurements. Two *in vitro* methods capable of obtaining this insight are surface plasmon resonance (SPR) and quartz crystal microbalance (QCM).

Both SPR and QCM are surface-sensitive label-free techniques for real-time monitoring of bioaffinity reactions, for which they have both been widely used since the early 1990s (Becker & Cooper, 2011; Frazier et al., 2008; Geddes et al., 1994; Glaser, 1993; Muratsugu et al., 1993; Sjölander & Urbaniczky, 1991). The flow channel configuration of these two devices enables an easy and accurate control of the physiochemical conditions throughout the experiments. The combined use of data from both experimental devices has become common. However, in most cases, the difference in hydrodynamic flow conditions between them has either been dealt with only superficially or not at all (Ayela et al., 2007; Kößlinger et al., 1995; Peeters et al., 2008; Peh et al., 2007; Reimhult et al., 2004; Su et al., 2006; Su et al., 2005a; Vikholm et al., 1999; Wilczewski et al., 2008). The static and batch flow measurements with SPR and QCM are problematic, because these conditions do not very well represent the situation *in vivo* where blood flow and shear stress in different vessels and organs can vary substantially. We attempt to rectify this through the development of a dynamic measurement protocol using these two apparatuses in concert.

Since the earliest reports on the use of SPR for biomolecular interaction studies, considerable effort has been put into the understanding of how the signal response is influenced by sample delivery, liquid flow profiles, and dynamics (Christensen, 1997; Glaser, 1993; Myszka et al., 1997; Sjölander & Urbaniczky, 1991). This has led to a comprehensive understanding of the effect of flow channel design (Sjölander & Urbaniczky, 1991) and sampling protocols (Glaser, 1993) on mass transfer and kinetics models, which are now widely used for the analysis of SPR sensograms (Christensen, 1997; Karlsson et al., 2006; Myszka, et al., 1997). While QCM has been used for bioaffinity studies as long as SPR, only a few attempts have been made to increase our understanding to the QCM technique itself and to use this understanding to optimize it for biomolecular interaction studies (Anderson et al., 2007; Jönsson et al., 2007; Ohlsson et al., 2010). A possible reason for this could be that QCM has mainly been seen as a complimentary technique to SPR, providing additional information of structural changes that occur during a binding event. QCM measures the amount of water coupled

dynamically to the biomolecules, as often binding events are accompanied by structural changes (Peh, et al., 2007; Reimhult, et al., 2004; Su, et al., 2005a). So far, only a few studies have focused on achieving identical measurement conditions in the combined use of SPR and QCM devices for biomolecular interaction studies (Kößlinger, et al., 1995; Reimhult, et al., 2004). In these studies, the SPR and QCM sensors have been integrated in specially designed measuring chambers hosting both sensor surfaces, which are not commercially available. Hence, the synchronization of hydrodynamic flow conditions in the combined use of separate SPR and QCM instruments has not so far been addressed in the literature.

In this study, we synchronized the fluid flow conditions in SPR and QCM flow channels by determining calibration constants for the flow channels through CFD modeling. Our protocol for synchronizing the flow conditions between SPR and QCM flow channels involves calculating the shear stress on the measurement surface of the flow channels as a function of the flow rate and the flow channel height. Interaction between surface immobilized biotin and streptavidin was used as a biomolecular binding model system. The interaction of biotinylated liposomes and streptavidin functionalized surface was used as a targeted drug delivery model system.

6.2 Materials and methods

6.2.1 Materials

Streptavidin (Catalog No.21125) was purchased from Pierce Protein Research Products, USA. HS–$(CH_2)_{11}$–$(OCH_2OCH_2)_3$–OH (EG_3, Catalog No. TH002-02) and HS–$(CH_2)_{11}$–$(OCH_2OCH_2)_3$-biotin (EG_3-biotin, Catalog No. TH012-02) were purchased from ProChimia Surfaces Sp. z o. o., Poland. L-α-phosphatidylcholine, hydrogenated (Soy) (HSPC), 1,2-distearoyl-sn-glycero-3-phosphoethanolamine-N-[biotinyl(polyethylene glycol)-2000] (ammonium salt) (DSPE-PEG_{2000}-Biotin), 1,2-distearoyl-sn-glycero-3-phosphoethanolamine-N-[methoxy(polyethylene glycol)-2000] (ammonium salt) (DSPE-PEG_{2000}), and cholesterol (ovine wool, >98%) (CHOL) were purchased from Avanti Polar Lipids, Inc. (http://www.avantilipids.com/). Ammonium hydroxide (NH_4OH, Catalog No. 320145), bovine serum albumin (BSA, Catalog No. A2153), 4-(2-Hydroxyethyl) piperazine-1-ethanesulfonic acid (HEPES, Catalog No. H3375), hydrogen peroxide (H_2O_2, Catalog No. 516813), and sodium chloride (NaCl, Catalog No. 31434) were purchased from Sigma–Aldrich. Ethanol (EtOH, grade A) was purchased from Altia group, Finland. High purity water (18.2 MΩ cm) from a Milli-Q system (Millipore, Bedford, USA) was used for the preparation of buffer solutions. Glass slides (Schott D263, 20 mm × 12 mm × 0.5 mm) with ca. 50 nm gold sputtered on 2 nm of Cr (BioNavis Ltd., Helsinki. Finland) were used as the SPR sensor slides. Gold coated AT-cut quartz crystals with a nominal frequency of 5 MHz (Biolin Scientific AB, Sweden) were used as the QCM sensor. Milli

Pore membranes with 100 nm pores were purchased from Millipore (http://www.Millipore.com).

6.2.2 Computational fluid dynamics

Computational Fluid Dynamics (CFDs) was used to calculate the flow profile/pattern in the flow channels of both the QCM and SPR devices. The geometries of the SPR and the QCM flow channels were constructed and meshed using the commercial pre-processing software Gambit. Two different mesh resolutions were used in order to insure the consistency of the results. An open-source, multiphysics software package Elmer (http://www.csc.fi/elmer) which utilizes the Finite Element method was used for the solution of the Navier-Stokes equation, assuming an incompressible fluid. The detailed procedure and results of the computational fluid dynamics modeling are given in Supporting Material (SI).

6.2.3 Surface plasmon resonance measurements

The SPR measurements were performed by using a commercially available SPR Navi 200 (BioNavis Ltd., Finland) instrument. This is a true goniometer and prism-coupling based device with two independent channels and an integrated peristaltic pump (Liang et al., 2010). Molecular adsorption or interactions on the gold sensor slide can be followed by monitoring either the intensity change at a fixed angle (fixed angle mode) or change in angular position (angular scan mode) over time. The measured change in angular position corresponds to the amount of adsorbed material with a mass sensitivity of 100 mdeg per 100 ng/cm^2. The SPR measurements were conducted at room temperature with the angular scan mode.

6.2.4 Impedance based quartz crystal microbalance measurements

The QCM measurements were performed using the impedance based QCM-Z500 instrument (KSV, Biolin Scientific Oy, Finland). This instrument allows for the simultaneous measurement of resonance frequency change (Δf) and quality of the resonance (Q) at 6 harmonics (fundamental frequency, 15, 25, 35, 45, and 55 MHz, corresponding to the overtones, 0, 3, 5, 7, 9 and 11) of a 5 MHz crystal (Kujawa et al., 2007; Viitala et al., 2007). Assuming the validity of the Sauerbrey relation (Sauerbrey, 1959), the measured frequency change corresponds to the quantity of adsorbed material with a mass sensitivity 17.7 ng/(cm^2 Hz). If the adsorbed layer is soft, the adsorbed mass and the viscoelastic properties of the adsorbed material can be determined by using an equivalent circuit analysis (Bandey, 1999). The QCM measurements were conducted at room temperature, and viscoelastic modeling was performed using the QCM-Z500 data

analysis software suite, version 3.30, to extract mass areal density, viscosity, and elasticity of the liposome layers.

6.2.5 Preparation of sensor surfaces

The gold coated SPR and QCM sensor substrates were cleaned by boiling in a NH_4OH (30%)/H_2O_2 (30%)/H_2O (1:1:5, v/v) solution for 10 min, rinsed with water, and dried with nitrogen gas. A mixed EG_3/EG_3-biotin (5:1) self-assembled monolayer was prepared on the cleaned substrate surfaces by immersing in an EtOH solution containing 0.24 mM EG_3/EG_3-biotin. The self-assembly process was allowed to proceed overnight in a sealed vessel that was continuously flushed with nitrogen gas. The sensor surfaces were then removed and sonicated in EtOH for 5 s, followed by rinsing with EtOH three times to remove excess and weakly bound thiols and finally dried under a stream of nitrogen.

6.2.6 Preparation of biotinylated liposomes

Liposomes were prepared by traditional extrusion technique. Lipids dissolved in chloroform were pipetted with glass pipettes to form a lipid mixture, of total volume 1 ml, with the lipid molar ratios of 64.38% HSPC: 32.41% CHOL: 2.577% DSPE-PEG_{2000}: 0.635% DSPE-PEG_{2000}-Biot. Lipid films were prepared by vacuum rotatory evaporation of the mixed lipid solution in a water bath at 65 °C. The dried lipid films were hydrated in 1 ml 20 mM HEPES/150 mM NaCl pH 7.4 (HEPES) buffer by vortexing to obtain a suspension of multilamellar vesicles followed by incubation for 30 min in a water bath at 65 °C. The liposomes were extruded (LIPEXTM Extruder) at 65 °C through 100 nm polycarbonate filters (Nucleopore) 10 times. The size of the liposomes was determined by dynamic light scattering (Malvern Zetasizer 3000) to be 130 nm.

6.2.7 Experimental procedure

For the case of the biotin–streptavidin interaction studies, the sensor substrates were mounted in flow channels in separate SPR and QCM instruments. The flow channel was filled with a 20 mM HEPES/150 mM NaCl buffer with a pH of 7.4 (HEPES buffer), and a continuous flow of buffer at a predetermined volumetric flow rate was used throughout the experiments. After a stable baseline was obtained for the measured signal, a BSA solution of 0.5 mg/ml in HEPES buffer was injected as a plug into the continuously flowing buffer stream in order to block nonspecific interaction sites on the EG_3/EG_3-biotin surface. After rinsing the flow channel with HEPES buffer to remove excess BSA, streptavidin solutions of 1.25, 2.5, 5, 10, or 20 nM were injected with a constant flow rate to measure the specific interaction between streptavidin and biotin immobilized on the sensor surface. A constant interaction time of 10 min was allowed for each concentration and volumetric flow rate. In SPR experiments, a new sensor surface was used for each streptavidin

concentration, while for QCM measurements, the same sensor surface was used and the streptavidin solutions were consecutively injected into the QCM flow channel to monitor the interaction between streptavidin and biotin. The use of separate sensor surfaces in SPR measurements and the same sensor surface in QCM measurements is not believed to influence the overall results. The affinity of streptavidin for biotin is very high; practically, no dissociation is taking place. The dissociation constant (K_D) of the streptavidin–biotin complex is of the order of $\sim 10^{-14}$ M (Green, 1975). Trutnau has demonstrated that practically identical kinetic constants are obtained by analyzing sequential binding and binding to regenerated surfaces for a system with rather high affinity, that is, $\sim 10^{-9}$ M (Trutnau, 2006). Therefore, it is anticipated that the difference in the amount of bound streptavidin when different concentrations are either injected consecutively on the same sensor surface or as single doses on separate sensor surfaces would be negligible. The measurements with SPR were performed at the flow rates of 10 and 100 μl/min, whereas QCM measurements were performed at the flow rates of 10, 73, 100, and 733 μl/min.

For the biotinylated liposome–streptavidin functionalized surface interactions, the measurements followed largely the same procedure as described above for biotin–streptavidin with the following exceptions: (1) The sensor substrates were functionalized with streptavidin *ex situ* by immersing the biotinylated substrate into 50 μg/ml streptavidin in HEPES buffer overnight followed by overnight immersion in 0.5 mg/ml BSA in HEPES buffer, (2) the streptavidin functionalized sensor substrates were mounted in flow channels in separate SPR and QCM instruments, and biotinylated liposome solutions with lipid concentrations of 14.7, 28.3, 56.7, 113.3, and 226.7 μM were injected with a constant flow rate to measure the specific interaction between biotinylated liposomes and streptavidin immobilized on the sensor surface, and (3) SPR measurements were performed by consecutive injection of liposomes with increasing concentration at flow rates of 10 and 100 μl/min, and QCM measurements were performed at volumetric flow rates of 73 and 733 μl/min.

6.3 Results and discussion

6.3.1 Computational fluid dynamics modeling

Our goal is to synchronize the flow conditions in the SPR and QCM apparatuses in order to provide the means for quantitative interpretation of surface specific interactions when information from both of these complementary techniques are used. The flow channels of the SPR instrumentation are commonly designed to have a rectangular footprint, whereas QCM flow channels need to be circular in order not to interfere with the active area of the cylindrical QCM sensor. Fig. 1 shows the geometries of the SPR and QCM flow channels used in this study. The flow behaviour in each device as a function of flow channel height will differ as a result of their different footprints. Since the footprint of the devices is specified by their function, it cannot be altered but its effect needs to be

calibrated in order to take into account the different flow pattern. The flow dynamics in the SPR and QCM flow channels can be varied either by changing either the height of the flow channels or the flow rate of the liquid.

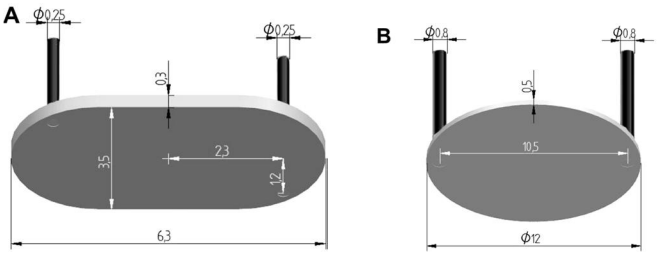

Fig. 1. *Schematics of the dimensions of the flow channels for (A) SPR and (B) QCM apparatuses. Light and dark gray areas comprise the volume of the flow channels. Measures in mm.*

The well-known approximate expressions for mass transfer coefficient (Sjölander & Urbaniczky, 1991) or diffusion layer thickness (Glaser, 1993) are not suitable as such for calibration since they are merely derived for the rectangular shaped flow channels used in SPR, while the footprint of the flow channels in QCM is circular. The different geometries influence directly the diffusion layer thickness over different parts of the sensing area which is an inherent parameter in the mass transfer expressions, and its variation due to the shape of the flow channel cannot easily be cancelled out. Our approach for calibrating flow channels with different footprints is based on taking the shear stress at the measurement surface as the relevant variable with respect to the flow conditions. This provides a calibration approach that is completely insensitive to the dependency of the diffusion layer thickness (i.e., mass transfer) over the sensing surface. Our calibration approach is thus more independent of the studied system than mass transfer expressions, because there is no need to know the diffusion properties of the materials or diffusion layer thickness for the system. We used CFD to calculate the value of this as a function of the flow channel height and volumetric flow rate.

In order to verify the consistency of flow hydrodynamics in the SPR and QCM flow channels with varying heights, we simulated the relationship between the flow channel height and the shear stress in the region of the sensing area. We used fixed flow rates of 10 and 100 µl/min for each case. The flow rates for the SPR experiments were chosen so that they would resemble typical flow rates used for SPR kinetics measurements. The detailed procedure and results of the fluid dynamics modeling are given in Supporting Material SI.

In brief, we extracted the flow profile (flow velocity as a function of position in the flow channel normalized to the volumetric flow rate) in the center of both the SPR and QCM channels, for all heights, both flow rates, and both grid resolutions. We see that in all cases: (1) A near perfect agreement exists between the low and high grid resolution results, thus the grid resolution is not an issue; (2) The flow profile in both cases is parabolic and can thus be fitted perfectly to a quadratic expression, approaching the limit of Poiseuille flow in the center of the flow channel; and (3) The flow velocity is perfectly proportional to the volumetric flow rate. As a representative example, this is shown in Fig.

2a for a QCM flow channel with a height of 0.5 mm, where the height has been defined as the distance from the bottom of the channel.

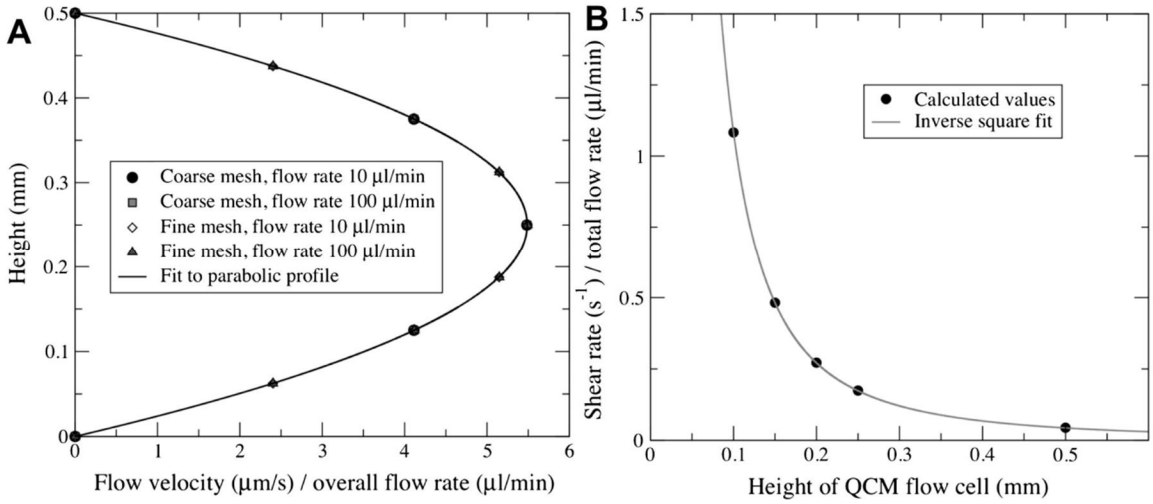

Fig. 2. *(a) Flow velocity profile normalized to the flow velocity at the center of the QCM flow channel with a height of 0.5 mm, showing an extremely small deviation between the low and high resolution grid sizes, a completely linear scaling with flow rate, and a nearly perfect parabolic shape. Fit constant A (see text) 87.8 ± 0.1 for QCM. The corresponding fit constant A for SPR is (8.52 ± 0.1) × 10^3 (graph not shown). (b) Shear rate (SR) in the center of the bottom surface vs. flow channel height from parabolic fit to the flow velocity profile for QCM. We see the hypothesized inverse square relationship and have thus determined the shear stress in the center of the measurement surface to be 1.0834 × $10^{-2}fh^{-2}\mu$, where f is the flow rate in µl/min, h is the QCM flow channel height in mm, and µ is the viscosity of liquid in the flow cell. Corresponding shear stress at the center of the measurement surface for the SPR flow channel was determined to be 2.86 × $10^{-2}fh^{-2}\mu$.*

6.3.2 Synchronizing SPR and QCM flow channels

The combination of parabolic flow profile and linear scaling with flow rate indicates that at the center of both devices, the flow behaviour has converged to the limit of Poiseuille flow (Stokes flow between two infinite parallel plates). In this limit, it can be shown that the relationship between flow channel height h, volumetric flow rate f, and shear stress on the bottom surface *SS*, is $SS \propto fh^{-2}$ (Nakayama & Boucher, 1999). Since the flow profile is parabolic, if we assume no-slip conditions, the flow velocity as a function of height relative to the center of both devices will fit the following equation:

(1) $$v_f(x) = A\left[\left(\frac{h}{2}\right)^2 - x^2\right]f$$

where x is the vertical position in the flow channel (x=0 at the half-height of the channel and x = -h/2 at the bottom), h is the height of the flow channel, *f* is the volumetric flow rate through the device in units of µl/min, and A is a constant with respect to vertical position. Given a value for A, the shear rate (SR) in the center of the bottom surface is *SR*

$= Ahf$. Since for Poiseuille flow $SR \propto fh^{-2}$, if we express A as $A = Bh^{-3}$, B is a factor that is purely a function of the lateral dimensions (footprint) of the flow channel. Both the QCM and SPR flow channels will have their own constant factor B which can be used to calibrate the two devices to each other and all effects on the flow behavior resulting from the different footprints of the two devices are contained in this single number. For each device, all the flow velocity data in the center of the flow channel can now be fitted to the single function

$$v_f(x) = Bh^{-3}\left[(\frac{h}{2})^2 - x^2\right]f \tag{2}$$

and the shear stress at the bottom surface will be given by $SS = Bfh^{-2}\mu$ where μ is the viscosity of liquid in the flow cell. Fig. 2b shows a plot of SR/f vs. h to which the functional form of Eq. (2) has been fitted, to determine $B_{QCM} = 1.083 \times 10^{-2}$. Similarly, for the SPR, we found $B_{SPR} = 2.86 \times 10^{-2}$. By setting the shear stress equal for both flow channels, we thus have our scaling expression for relating the flow channel heights when using the same constant flow rate in both flow channels

$$h_{QCM} = (\frac{B_{QCM}}{B_{SPR}})^{1/2} h_{SPR} = 0.616 h_{SPR} \tag{3}$$

where $f_{QCM} = f_{SPR}$ and $S_{QCM} = S_{SPR}$, or alternatively our scaling expression for relating the flow rates for flow channels with fixed heights when $S_{QCM} = S_{SPR}$:

$$f_{QCM} = (\frac{B_{SPR}}{B_{QCM}})(\frac{h_{QCM}}{h_{SPR}})^2 f_{SPR} = 2.64(\frac{h_{QCM}}{h_{SPR}})^2 f_{SPR} \tag{4}$$

This method is generalizable to all SPR and QCM flow cell devices, which each will have a "B factor" that can be calculated in analogous fashion. As an example, we have also calculated the B factor of the BIAcore SPR flow cell (calculation not shown) using the same method and found the value for this to be 0.184.

Because of the difficulty at this stage to redesign the geometry of the flow channels of the commercial SPR and QCM devices used in this study, we chose, for the experimental verification of our synchronization approach, the two fixed flow rates for the SPR flow channel used in the modeling and scaled the shear stress in the QCM flow channel by changing the flow rates of the liquid. The reason being that the height of SPR flow channel is lower, and we have previously shown that it performs well in monitoring the biomolecular interaction between streptavidin and biotin (Liang, et al., 2010). Our scaling expression Eq. (4) suggests that using flow rates of 10 and 100 µl/min in the SPR device requires flow rates of 73.3 and 733 µl/min to be used in QCM to synchronize the hydrodynamic conditions. In some cases, additional flow rates of 10 and 100 µl/min were used in QCM experiments, in order to compare differences in the results if similar flow rates are used for the two different flow channels.

6.3.3 Flow rate effect on SPR and QCM signal

As a first model system for the demonstration of the success of our scaling approach for synchronizing the SPR and QCM flow channel hydrodynamic conditions, we have chosen the biotin–streptavidin pair, which is well-known and widely used to functionalize surfaces for biomolecular interaction studies because of its high affinity constant (Anderson, et al., 2007; Peh, et al., 2007; Reimhult, et al., 2004; Su, et al., 2006; Su, et al., 2005a; Wilczewski, et al., 2008). From the measurement of the signal for SPR with flow rates 10 and 100 µl/min and QCM with flow rates of 10, 73.3, 100, and 733 µl/min (full results shown in Supporting Material SII), we calculated the corresponding mass of adsorbed streptavidin, shown in Fig. 3. First, we note that for both flow devices, the adsorption of streptavidin is strongly mass transport controlled, which is indicated by the flow rate dependency of the signal responses (Nygren-Babol et al., 2005; Sigmundsson et al., 2002). Mass transport controlled adsorption is a consequence of the relatively large height of both flow channel devices and of the high density of biotin ligands immobilized on the SPR and QCM sensor surfaces. The small changes in dissipation and the fact that the measured overtones superimpose when normalized by the overtone number (not shown) suggests that the streptavidin film assembled on the biotinylated surface is highly rigid and compact, in a similar fashion to previously reported results (Reimhult, et al., 2004; Su, et al., 2006; Su, et al., 2005a; Su et al., 2005b).

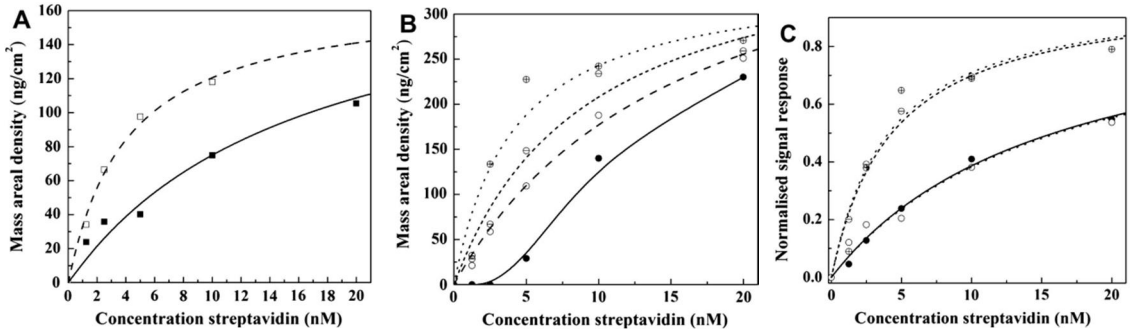

Fig. 3. *Signals after an interaction time of 10 min as a function of streptavidin concentration at different flow rates. (a) SPR with flow rates: 10 µl/min (solid square, solid line), 100 µl/min (open square, dashed line). (b) QCM with flow rates: 10 µl/min (solid dot, solid line), 73.3 µl/min (open dot, dashed line), 100 µl/min (open dot with horizontal line, dotted line), and 733 µl/min (open dot with cross, short dashed line). (c) Normalized result to demonstrate scaling. SPR, 10 µl/min (solid dot, solid line), QCM, 73.3 µl/min (open dot, dashed line), SPR, 100 µl/min (open dot with horizontal line, dotted line), QCM, 100 µl/min (gray triangle, gray dotted line), and QCM, 733 µl/min (open dot with cross, short dashed line). Dots are measured points and lines are Langmuir fits to the data points.*

We then proceeded to use liposomes containing biotin as a ligand binding to surface immobilized streptavidin as a targeted drug delivery model system, in order to further verify our scaling approach between SPR and QCM flow channel hydrodynamic conditions. The reason for this selection is that liposomes have been studied extensively in the context of their use as drug delivery systems. In addition, a number of liposome based

drug delivery systems have already been approved for clinical use (Farokhzad & Langer, 2009). The influence of blood hydrodynamic flow on the liposome behaviour at the target binding and consequently its impact on the therapeutic effect has not been systematically studied. A powerful platform that would provide further insight into the effect of hydrodynamic flow on the liposome binding characteristics is the combined quantitative analysis of SPR and QCM data, which requires a precise calibrated modulation of the flow conditions in the SPR and QCM flow channels.

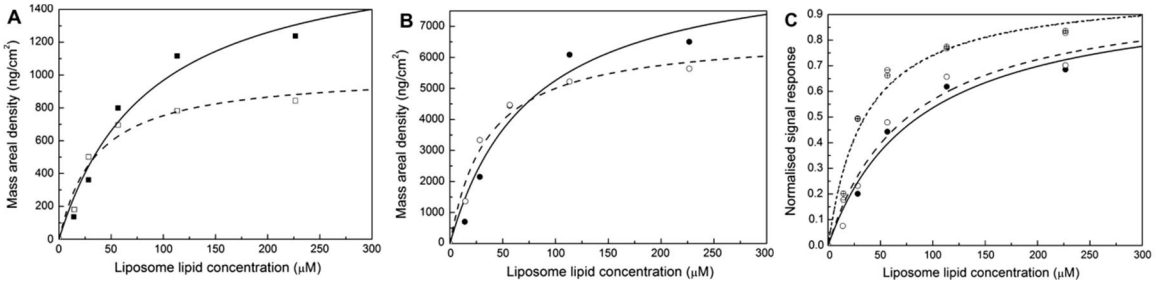

Fig. 4. *Signals after allowing liposome solutions with increasing concentration to interact with a streptavidin functionalized sensor surface for 10 min at different flow rates. (a) SPR with flow rates: 10 μl/min (solid square, solid line) and 100 μl/min (open square, dashed line). (b) QCM with flow rates: 73.3 μl/min (solid dot, solid line) and 733 μl/min (open dot, dashed line). (c) Normalized result to demonstrate scaling: SPR, 10 μl/min (solid dot, solid line), QCM, 73.3 μl/min (open dot, dashed line), SPR, 100 μl/min (open dot with horizontal line, dotted line), and QCM, 733 μl/min (open dot with cross, short dashed line). Dots are measured points, and lines are Langmuir fits to the data points.*

We have measured the time resolved signal for SPR with the flow rates of 10 and 100 μl/min and QCM with the flow rates of 73.3 and 733 μl/min for liposome binding to surface immobilized streptavidin (shown in Supporting Material SII). The signals after allowing a constant interaction time of 10 min for SPR with the flow rates of 10 and 100 μl/min and for QCM with the flow rates of 73.3 and 733 μl/min converted to mass of bound liposomes are shown in Fig. 4a and b. We find that the mass of bound liposomes is higher only for the 2 lowest concentrations in SPR and 3 lowest concentrations in QCM when comparing the high and low flow rates. Hereafter, the mass result for the high flow rate levels out to a lower value in comparison with that for the low flow rate. A possible explanation for the lower mass measured at higher liposome concentrations and high flow rate, in comparison with the low flow rate result, is that the concentration of liposomes on the surface has reached a critical density: the increased shear stress at high flow rate causes some of the adsorbed liposomes to rupture into bilayer patches. This is also indicated by the QCM measurement performed at the high flow rate (Supporting Material Figs. S2–2) where it can be seen that the normalized frequency response for the 3rd overtone has a sudden decrease at around 8000 s and two unexpected frequency increases on both sides of t = 10000 s. These time points coincide with a decrease in dissipation (not shown), which supports the fact that the increased shear stress at high flow rate induces rupturing of some of the liposomes when a critical quantity of liposomes has been bound to the surface. However, the mass area density at high liposome concentration and high

flow rate, shown in Fig. 4, indicates that only a small fraction of the liposomes have formed bilayer patches.

It is worth noting that under the conditions, and experimental setup used in this study, both of the studied systems may not have reached the equilibrium binding values in the limit of lower concentrations and low flow rate. This is, however, not critical with respect to the focus of this study, as the intention is to provide the means to calibrate the flow conditions of SPR and QCM flow channels against each other. Therefore, at this point, it is sufficient that the signals in SPR and QCM flow channel devices used in this study behave in the same manner at calibrated flow rates in order to verify the calibration of the flow conditions.

6.3.4 Verification of SPR and QCM flow channel synchronization

Table 1 lists the mass areal density after allowing 10 min of interaction between streptavidin and the biotinylated sensor surface ($\Delta M/A$), the apparent equilibrium constants (K), and correlation coefficients (R) obtained from the Langmuir fits to the SPR and QCM signals in Fig. 3a and b. The maximum adsorbed amount $(\Delta M/A)_{max}$ of streptavidin obtained from the Langmuir fits is clearly higher with the QCM measurements than with the SPR measurements. The difference in adsorbed amount between SPR and QCM responses is generally accepted to originate from the coupled water sensed by the mass sensitive QCM technique but not sensed by the optical SPR technique. This difference in mass between the two techniques is now commonly used to determine the amount of coupled water to, for example, adsorbed macromolecule layers (Peh, et al., 2007; Reimhult, et al., 2004). The SPR and QCM maximum adsorbed responses for streptavidin shown in Table 1 are slightly lower than values reported by others for streptavidin adsorbed to biotinylated self-assembled monolayers and solid supported lipid bilayers, that is, ~450-600 ng/cm^2 determined by QCM and ~210-370 ng/cm^2 determined by SPR (Reimhult, et al., 2004; Su, et al., 2005b). Our maximum adsorbed response values for streptavidin are in the same order of magnitude yet slightly lower compared to those literature values, which probably is due to the fact that the amount of biotin immobilized on the sensor surface is slightly lower in our measurements and that we have used a fixed interaction time of 10 min, which necessarily is not enough to reach complete saturation of the binding for the lower concentrations at the flow rates used in this study. Interestingly, the maximum adsorbed amounts obtained from the Langmuir fit in Table 1 for the lower flow rate are closer to the literature values than the values obtained for higher flow rates, which highlights the importance of the need to precisely control and synchronize the experimental flow conditions when comparing SPR and QCM measurements; however, this could also indicate that the overall structure of the streptavidin layer is depending on the flow rate.

Table 1. *Langmuir fit parameters and the amount of coupled water (ϕ) calculated from the $(\Delta M/A)_{max}$ values for streptavidin data.*

Flow channel	$(\Delta M/A)_{max}$ (±SD) (ng/cm^2)	Flow rate (µl/min)	K (±SD) (nM)	R^2	ϕ ($m_{QCM}/m_{SPR} - 1$)
SPR	196.5 (±11.8)	10	16.2 (±2.5)	0.988	1.33
QCM	458.4 (±50.5)	73.3	15.9 (±3.1)	0.994	
QCM	400.4 (±65.0)	100	9.25 (±3.2)	0.972	N.A.
SPR	169.8 (±13.6)	100	4.1 (±0.8)	0.993	1.07
QCM	350.2 (±53.9)	733	4.3 (±1.8)	0.942	

Table 1 shows that there is a noticeable difference between the maximum adsorbed responses from the Langmuir fit for the adsorbed amount even for the same flow channel device at different flow rates used in this study. The coupled water mass per streptavidin mass (ϕ) calculated from the SPR and QCM mass values in Table 1 is 1.07 and 1.3 for high and low flow rates, respectively. The amount of coupled water in the case of low flow rate in this study is in good agreement with the value of 1.3 for a high coverage of streptavidin adsorbed to a biotinylated solid supported lipid bilayer (Reimhult, et al., 2004). The difference in the coupled water values is believed to be a consequence of the different shear stress acting on the sensor surface at different flow rates, which consequently influences the adsorbed protein layer structure and amount. The lower value for coupled water of 1.07 indicates that the streptavidin layer under a higher flow rate and shear stress forms a more compact layer with less water being able to entrap between protein molecules compared to the streptavidin layer under a lower flow rate and shear stress. The apparent equilibrium constants shown in Table 1 for the synchronized flow rates between SPR and QCM devices coincide with each other confirming that our scaling approach based on hydrodynamic modeling is successful. This is also shown graphically in Fig. 3c, where the normalized responses for SPR and QCM at different flow rates are plotted. The normalization with the maximum adsorbed amount obtained from the Langmuir fits for each corresponding flow channel and flow rate enables unambiguous comparison of the responses between the SPR and QCM measurements, because normalization removes the contributions of coupled water from the QCM signal. Even though SPR measurements corresponding to the flow rate of 100 µl/min in the QCM were not measured, we have included the normalized response for QCM at 100 µl/min in Fig. 3c to further demonstrate that our rescaling approach is successful, which is confirmed by the fact that both the normalized response curve and the Langmuir fit parameters for QCM at 100 µl/min flow rate falls between the corresponding values for 73 and 733 µl/min flow rates.

The mass area density after allowing 10 min of interaction between biotinylated liposomes and the streptavidin functionalized sensor surface ($\Delta M/A$), the apparent equilibrium constants (K), and correlation coefficients (R) obtained from the Langmuir fits to the SPR and QCM signal responses in Fig. 4a and b are listed in Table 2. The maximum adsorbed amount $(\Delta M/A)_{max}$ induced by liposome adsorption obtained from the Langmuir fits is significantly higher for the QCM measurements in comparison with the SPR

measurements. This is mainly due to the fact that QCM also senses the encapsulated water in the liposomes, the entrapped water between the liposomes and coupled water to the liposomes, whereas the SPR does not.

Table 2. *Langmuir fit parameters for liposome data and viscoelastic properties of bound liposome layer for the highest liposome concentration.*

Flow channel	$(\Delta M/A)_{max}$ (±SD) (ng/cm^2)	Flow rate (µl/min)	K (±SD) (µM)	R^2	Liposome layer elasticity [a] (MPa)	Liposome layer viscosity [a] (mPa s)
SPR	1805 (±272)	10	87 (±30)	0.969	–	–
QCM	9266 (±1431)	73.3	76 (±28)	0.963	0.47	2.9
SPR	1019 (±107)	100	35 (±11)	0.962	–	–
QCM	6745 (±561)	733	35 (±9)	0.975	1.55	2.97

[a] Initial value of the fitted parameters: film elasticity = 0.1 MPa, film viscosity = 1 mPa s, film thickness = 10 nm.

The adsorbed mass of the liposomes (including entrapped water) can be estimated by a simplified model by assuming that they form an ideal monolayer of close-packed spheres with a density of 1 g/cm^3. With this simple assumption, the mass of adsorbed vesicles with a diameter of 130 nm becomes 7800 ng/cm^2, the same order of magnitude as the maximum mass of adsorbed liposomes predicted by the Langmuir fit for QCM measurements in Table 2. This simple calculation, however, does not take into account the water entrapped between the liposomes, which contributes to the total mass obtained by the QCM. Serro *et al*. estimated from simple geometrical considerations the percentage of mass of interstitial water to be ~20% (Serro et al., 2012). By subtracting this amount of water from the maximum adsorbed amount obtained from the Langmuir fit in Table 2 for the low flow rate liposome adsorption, the adsorbed mass of the liposomes becomes 7413 ng/cm^2. This value correlates well with the value calculated above for hexagonally packed liposomes with a diameter of 130 nm, which suggests that the liposomes adsorb as intact and non-deformed at low flow rate. This is further supported by the fact that the difference between QCM and SPR maximum adsorbed amount shown in Table 2 at low flow rate is 7461 ng/cm^2, very close to the mass of water spheres, that is, 7200 ng/cm^2, with a diameter of 120 nm (the bulk phase diameter of the liposome used in this work subtracted by the bilayer). We have also performed a theoretical optical modeling with Fresnel equations to predict the angular change in SPR that a hexagonally packed liposome layer would induce liposomes with a diameter of 130 nm. We found that that the mass areal density calculated from this angular change would correspond to ~1400 ng/cm^2, which is in very good agreement with the SPR results in Table 2.

Several studies have suggested that adsorption of liposomes under static conditions induces deformation/flattening of the liposomes, reducing the height to 80% of the bulk phase diameter (Jung et al., 2006; Reimhult et al., 2002; Reimhult et al., 2006). This is apparently not the case for the sterically stabilized liposomes used in this work that contain a large amount of cholesterol (>30%) and a few percent of PEGylated

distearoylphosphoethanolamine lipid. Cholesterol generally renders liposomes less deformable, and by adding a PEGylated phospholipid, the resistance against deformation of the liposomes would be expected to increase further. The studies suggesting liposome flattening upon adsorption under static conditions have mainly used liposomes based on purely unsaturated, egg-yolk or saturated lecithins, or mixtures of these.

For the case of high flow rate, the adsorbed mass of the liposomes obtained with QCM becomes 5396 ng/cm^2 by subtracting the percentage of mass of interstitial water of 20%. This corresponds to a diameter of ~90 nm for hexagonally packed liposomes, which is ~70% of the bulk phase diameter. The difference between QCM and SPR maximum adsorbed amount shown in Table 2 at high flow rate is 5726 ng/cm^2 further confirming that the shear stress at higher flow rate clearly deforms and flattens the adsorbed liposomes compared to the low flow rate, consequently inducing rupture of some of the liposomes as discussed in the previous section. The large differences between the maximum adsorbed amounts of liposomes obtained both from SPR and QCM measurements once more highlight how important the synchronization of flow conditions for SPR and QCM flow channels becomes when the objective is to use results from both techniques for quantitative interpretations of biomolecular, targeted drug delivery and other surface specific interactions that take place in a dynamic flow.

It is worth mentioning that the calculations and discussions above concerning the adsorbed liposome layer structure are based on a very simplistic model and should only be taken as a guide, but they serve the purpose of giving a qualitative picture of the adsorption behaviour of liposomes at different flow rates and shear stresses. A more in depth analysis of the adsorption behaviour of liposomes under varying flow conditions and shear stresses is out of the scope of this work and will be given elsewhere.

The elasticity and viscosity obtained from QCM modeling for the adsorbed liposome layers at different flow rates are shown in Table 2. The elasticity and viscosity values of liposome layers adsorbed at low flow rate are of the same order of magnitude as those reported for DMPC/DPPC based liposomes with 30% of added cholesterol (Reimhult, et al., 2006). However, the liposome layer adsorbed at high flow rate shows a significantly higher elasticity compared to the low flow rate still supporting the scenario of formation of bilayer patches due to the rupturing of some of the liposomes and a more compact liposome layer with less interstitial water between the flattened liposomes.

By using the same approach as in the case of streptavidin–biotin interaction, we have normalized the SPR and QCM signals for liposome adsorption with the maximum adsorbed amount obtained from the Langmuir fits for each corresponding flow channel and flow rate. Fig. 4c shows the SPR and QCM normalized responses for liposome adsorption at different flow rates, and the apparent equilibrium constants are shown in Table 2. The normalized responses and the apparent equilibrium constants for the synchronized flow rates between SPR and QCM devices coincide with each other further confirming that our scaling approach based on hydrodynamic modeling is not only successful for rigid protein–ligand interactions, but also for more complex interactions involving the formation of viscoelastic layers and especially including nanoparticles. The latter being of great interest in the field of targeted drug delivery research as the role of hydrodynamic flow effects on targeting has not yet been widely studied.

As the final comparison, we also made an attempt to use the approximate expressions for mass transfer coefficient (Sjölander & Urbaniczky, 1991) or diffusion layer thickness (Glaser, 1993) for synchronizing our SPR and QCM flow channels. The approximate mass transfer coefficient or diffusion layer thickness expressions for our flow channels give a scaling factor of 5.29 for the flow rate scaling. The scaling coefficient for the flow rate obtained from our approach from CFD modeling of shear stress is 7.33. The difference in these two scaling coefficients is rather large. For the case of the QCM flow channel, however, there is a large difference between the signals measured with flow rates of 73.3 and 100 µl/min suggesting that the influence of the geometrical differences has to be taken into account for proper synchronization of SPR and QCM flow channels, which is the case in the calibration approach we have presented in this study.

6.4 Conclusions

SPR and QCM are well established techniques for studying biomolecular interactions. Both techniques have their own strengths and weaknesses and complement each other. This has driven many researchers to use both SPR and QCM in their research to gain as much information as possible about their systems of interest. We foresee that the biomolecular interaction studies are constantly moving toward more dynamic systems where hydrodynamic flow plays a crucial role. The effect of bloodstream hydrodynamics on interaction kinetics can no longer be omitted. The combined use of SPR and QCM is a promising approach for building an understanding of the effect of bloodstream hydrodynamics on interaction kinetics, but so far the combined use of SPR and QCM with synchronized dynamic flow conditions has not been widely studied.

In this study, we have presented a new approach to how CFD can be used to calibrate the flow behaviour in flow channels of separate SPR and QCM devices. The extracted scaling expressions (Eqs. (3) and (4)) relate the volumetric flow rate and flow channel heights by simple expressions through a single scaling constant (B) that completely encapsulates all effects resulting from the footprint of the flow channel. The importance of the use of our new scaling method that involved the use of CFD to calculate the effects of flow channel geometry to calculate a new scaling constant B can be demonstrated through a comparison of the results we gained to the results obtained using the mass transfer coefficient or diffusion layer thickness expressions for scaling. Because the majority of SPR instruments uses (to a good approximation) rectangular shaped flow channels and most QCM instruments have a flow channel with a circular footprint, our approach should be generally applicable for calibrating SPR and QCM device flow channels against each other, as long as their precise height is known. Our approach also provides the means to easily redesign flow channels for SPR and QCM devices with synchronized flow conditions with a wide dynamic flow rate range and consequently also control the shear stress experienced by the sensor surface.

The success of the scaling procedure was demonstrated with a well know biomolecular interaction pair of biotin and streptavidin, as well as with a targeted drug delivery model system of biotinylated liposomes. We also got some indications of how shear stress might

influence the structure of adsorbed protein and liposome layers, which opens up new opportunities for building a better understanding of interaction kinetics of biomolecular interactions and targeted drug delivery systems under controlled flow conditions.

Acknowledgments

We thank Jussi-Pekka Tuppurainen from Bionavis Ltd., and Niko Granqvist for valuable discussions during this study. Dr. Lasse Murtomäki, Teemu Laurila, and Terhi Laurila are acknowledged for their help with Comsol modeling. TV and HL acknowledge Academy of Finland for financial support (Grant Nos. 137053 and 140980). AB acknowledges support from CIMO.

6.5 References

Anderson, H., Jönsson, M., Vestling, L., Lindberg, U., & Aastrup, T. (2007). Quartz crystal microbalance sensor design: I. Experimental study of sensor response and performance. *Sensors and Actuators B: Chemical, 123*(1), 27-34.

Ayela, C., Roquet, F., Valera, L., Granier, C., Nicu, L., & Pugnière, M. (2007). Antibody-antigenic peptide interactions monitored by SPR and QCM-D. A model for SPR detection of IA-2 autoantibodies in human serum. *Biosensors and Bioelectronics, 22*(12), 3113-3119.

Bandey, H. L. (1999). Modeling the responses of thickness-shear mode resonators under various loading conditions. *Analytical Chemistry, 71*(11), 2205-2214.

Becker, B., & Cooper, M. A. (2011). A survey of the 2006–2009 quartz crystal microbalance biosensor literature. *Journal of Molecular Recognition, 24*(5), 754-787.

Christensen, L. L. H. (1997). Theoretical analysis of protein concentration determination using biosensor technology under conditions of partial mass transport limitation. *Analytical Biochemistry, 249*(2), 153-164.

Farokhzad, O. C., & Langer, R. (2009). Impact of nanotechnology on drug delivery. *Acs Nano, 3*(1), 16-20.

Frazier, R. A., Kooyman, R. P. H., Corn, R. M., Schasfoort, R. B. M., & Tudos, A. J. (2008). *Handbook of Surface Plasmon Resonance*: Royal Society of Chemistry.

Geddes, N. J., Pachinger, E. M., Furlong, D. M., Ebara, Y., Okahata, Y., Than, K. A., et al. (1994). Piezoelectric crystal for the detection of immunoreactions in buffer solutions. *Sensors and Actuators: B. Chemical, 17*(2), 125-131.

Glaser, R. W. (1993). Antigen-Antibody Binding and Mass Transport by Convection and Diffusion to a Surface: A Two-Dimensional Computer Model of Binding and Dissociation Kinetics. *Analytical Biochemistry, 213*(1), 152-161.

Green, N. M. (1975). Avidin. *Advances in Protein Chemistry, 29*(C), 85-133.

Jönsson, M., Anderson, H., Lindberg, U., & Aastrup, T. (2007). Quartz crystal microbalance biosensor design: II. Simulation of sample transport. *Sensors and Actuators B: Chemical, 123*(1), 21-26.

Jung, H., Kim, J., Park, J., Lee, S., Lee, H., Kuboi, R., et al. (2006). Atomic force microscopy observation of highly arrayed phospholipid bilayer vesicle on a gold surface. *Journal of Bioscience and Bioengineering, 102*(1), 28-33.

Karlsson, R., Katsamba, P. S., Nordin, H., Pol, E., & Myszka, D. G. (2006). Analyzing a kinetic titration series using affinity biosensors. *Analytical Biochemistry, 349*(1), 136-147.

Kößlinger, C., Uttenthaler, E., Drost, S., Aberl, F., Wolf, H., Brink, G., et al. (1995). Comparison of the QCM and the SPR method for surface studies and immunological applications. *Sensors and Actuators: B. Chemical, 24*(1-3), 107-112.

Kujawa, P., Schmauch, G., Viitala, T., Badia, A., & Winnik, F. M. (2007). Construction of viscoelastic biocompatible films via the layer-by-layer assembly of hyaluronan and phosphorylcholine-modified chitosan. *Biomacromolecules, 8*(10), 3169-3176.

Liang, H., Miranto, H., Granqvist, N., Sadowski, J. W., Viitala, T., Wang, B., et al. (2010). Surface plasmon resonance instrument as a refractometer for liquids and ultrathin films. *Sensors and Actuators, B: Chemical, 149*(1), 212-220.

Muratsugu, M., Ohta, F., Miya, Y., Hosokawa, T., Kurosawa, S., Kamo, N., et al. (1993). Quartz crystal microbalance for the detection of microgram quantities of human serum albumin: Relationship between the frequency change and the mass of protein adsorbed. *Analytical Chemistry, 65*(20), 2933-2937.

Myszka, D. G., Morton, T. A., Doyle, M. L., & Chaiken, I. M. (1997). Kinetic analysis of a protein antigen-antibody interaction limited by mass transport on an optical biosensor. *Biophysical Chemistry, 64*(1-3), 127-137.

Nakayama, Y., & Boucher, R. F. (1999). *Introduction to fluid mechanics*. London, New York: Arnold ; J. Wiley & Sons.

Nygren-Babol, L., Sternesjö, Å., Jägerstad, M., & Björck, L. (2005). Affinity and rate constants for interactions of bovine folate-binding protein and folate derivatives determined by optical biosensor technology. Effect of stereoselectivity. *Journal of Agricultural and Food Chemistry, 53*(13), 5473-5478.

Ohlsson, G., Axelsson, P., Henry, J., Petronis, S., Svedhem, S., & Kasemo, B. (2010). A miniaturized flow reaction chamber for use in combination with QCM-D sensing. *Microfluidics and Nanofluidics, 9*(4-5), 705-716.

Peeters, S., Stakenborg, T., Reekmans, G., Laureyn, W., Lagae, L., Van Aerschot, A., et al. (2008). Impact of spacers on the hybridization efficiency of mixed self-assembled DNA/alkanethiol films. *Biosensors and Bioelectronics, 24*(1), 72-77.

Peh, W. Y. X., Reimhult, E., Huey, F. T., Thomsen, J. S., & Su, X. (2007). Understanding ligand binding effects on the conformation of estrogen receptor α-DNA complexes: A combinational quartz crystal microbalance with dissipation and surface plasmon resonance study. *Biophysical Journal, 92*(12), 4415-4423.

Reimhult, E., Höök, F., & Kasemo, B. (2002). Vesicle adsorption on SiO2 and TiO2: Dependence on vesicle size. *Journal of Chemical Physics, 117*(16), 7401-7404.

Reimhult, E., Larsson, C., Kasemo, B., & Höök, F. (2004). Simultaneous surface plasmon resonance and quartz crystal microbalance with dissipation monitoring measurements of biomolecular adsorption events involving structural transformations and variations in coupled water. *Analytical Chemistry, 76*(24), 7211-7220.

Reimhult, E., Zäch, M., Höök, F., & Kasemo, B. (2006). A multitechnique study of liposome adsorption on Au and lipid bilayer formation on SiO2. *Langmuir, 22*(7), 3313-3319.

Sauerbrey, G. (1959). Verwendung von schwingquarzen zur wägung dünner schichten und zur mikrowägung. *Z. Phys., 155*, 206-222.

Serro, A. P., Carapeto, A., Paiva, G., Farinha, J. P. S., Colaco, R., & Saramago, B. (2012). Formation of an intact liposome layer adsorbed on oxidized gold confirmed by three complementary techniques: QCM-D, AFM and confocal fluorescence microscopy. *Surface and Interface Analysis, 44*(4), 426-433.

Sigmundsson, K., Másson, G., Rice, R., Beauchemin, N., & Öbrink, B. (2002). Determination of active concentrations and association and dissociation rate constants of interacting biomolecules: An analytical solution to the theory for kinetic and mass transport limitations in biosensor technology and its experimental verification. *Biochemistry, 41*(26), 8263-8276.

Sjölander, S., & Urbaniczky, C. (1991). Integrated fluid handling system for biomolecular interaction analysis. *Analytical Chemistry, 63*(20), 2338-2345.

Su, X., Lin, C. Y., O'Shea, S. J., Teh, H. F., Peh, W. Y. X., & Thomsen, J. S. (2006). Combinational application of surface plasmon resonance spectroscopy and quartz crystal microbalance for studying nuclear hormone receptor-response element interactions. *Analytical Chemistry, 78*(15), 5552-5558.

Su, X., Wu, Y. J., & Knoll, W. (2005a). Comparison of surface plasmon resonance spectroscopy and quartz crystal microbalance techniques for studying DNA assembly and hybridization. *Biosensors and Bioelectronics, 21*(5), 719-726.

Su, X., Wu, Y. J., Robelek, R., & Knoll, W. (2005b). Surface plasmon resonance spectroscopy and quartz crystal microbalance study of streptavidin film structure effects on biotinylated DNA assembly and target DNA hybridization. *Langmuir, 21*(1), 348-353.

Trutnau, H. H. (2006). New multi-step kinetics using common affinity biosensors saves time and sample at full access to kinetics and concentration. *Journal of Biotechnology, 124*(1), 191-195.

Viitala, T., Hautala, J. T., Vuorinen, J., & Wiedmer, S. K. (2007). Structure of anionic phospholipid coatings on silica by dissipative quartz crystal microbalance. *Langmuir, 23*(2), 609-618.

Vikholm, I., Viitala, T., Albers, W. M., & Peltonen, J. (1999). Highly efficient immobilisation of antibody fragments to functionalised lipid monolayers. *Biochimica et Biophysica Acta - Biomembranes, 1421*(1), 39-52.

Wilczewski, M., Van Der Heyden, A., Renaudet, O., Dumy, P., Coche-Guérente, L., & Labbé, P. (2008). Promotion of sugar-lectin recognition through the multiple sugar presentation offered by regioselectively addressable functionalized templates (RAFT): A QCM-D and SPR study. *Organic and Biomolecular Chemistry, 6*(6), 1114-1122.

Appendix: Supporting material

SI. Detailed procedure of fluid dynamics modeling of SPR and QCM flow channels

As stated in the materials and methods section, the flow behavior inside the flow channels was modeled as an incompressible fluid flow governed by the Navier-Stokes equations, using an open-source, multiphysics software package Elmer (http://www.csc.fi/elmer) which utilizes the Finite Element method. The solution was obtained using the iterative method of Generalized Conjugate Residual (GCR). Non-linearity caused by the acceleration term of the momentum equations was linearized using a Piccard linearization in the first 5 iteration steps and a Newton iteration scheme thereafter. Before the iteration, an incomplete lower/upper triangular matrix decomposition (ILU) method with a fill-in degree of 0 was used as a pre-conditioner of the system matrix. (Saad, 1996) For the coarser grid we also used a direct solver to validate the performance of the iterative Krylov subspace method. The final step of the simulation was the use of a separate solver module of Elmer to calculate the derivative of the velocity field in order to derive the shear in the bulk as well as on the walls of the device.

The geometries of the SPR and the QCM flow channels were constructed and meshed using the commercial pre-processing software Gambit. Two different resolutions were used in order to verify the consistency of our results. For the QCM, the coarser mesh consists of about 17000 nodes arranged in 3500 second order elements, with 4 element rows in the vertical direction of the flow channel. The higher resolution mesh contains about 11700 second order elements and 53000 nodes, with a vertical resolution of the flow channel consisting of 8 element layers. In a very similar manner, the geometry of the SPR was discretized using a coarse mesh of about 18000 nodes arranged into 3700 second order elements with, again, 4 vertical element layers inside the device. The higher resolution mesh of the SPR contained about 49000 nodes, 10700 second order elements, and 8 vertical element layers. The choice of using second order instead of linear element types is motivated by the fact that second order polynomials are the perfect choice for representing parabolic shaped velocity profiles that occur in the entry/exit pipes as well as in the narrow flow channel itself.

The numerical analysis implements the solution of the Navier-Stokes equation for an incompressible fluid,

(S Eq 1) $$\nabla \cdot \vec{u} = 0,$$

$$\rho\left(\frac{\partial \vec{u}}{\partial \tau} + \vec{u} \cdot \nabla \vec{u}\right) = -\nabla p + \rho g + \mu \nabla^2 \vec{u}$$

where u is the velocity vector, ρ is the density, p is the pressure, g is the body force per unit mass, which could be the gravitational acceleration, and μ is the viscosity of the fluid, respectively. The stress tensor τ is linked with the strain rate tensor in the form of a linear (Newtonian) rheology, with a constant viscosity μ. We use the material parameters as

given for water at room temperature, i.e., $\rho = 10^3$ kg m^{-3} and $\mu = 10^{-3}$ kg m^{-1}s^{-1}. All walls are subject to a no slip condition i.e. $\vec{u}|_{wall} = 0$.

At the inlet of the pipe, for the normal component of the inlet velocity (with respect to an outward pointing normal *n*), a parabolic velocity profile reflecting a developed Hagen-Poiseuille profile

(S Eq 2) $$\vec{u} \cdot \vec{n} = \mathrm{v}_n|_{inlet} = -\frac{2q_{inlet}}{\pi R_{inlet}^4}(R_{inlet}^2 - r^2),$$

is prescribed. The numerical values for the inlet radius R_{inlet} as well as the inlet volumetric flux q_{inlet} are presented later.

The relative importance of the different terms in equation (S Eq. 1) can be evaluated by introducing characteristic values of the velocity, *U*, the channel/device height, *H*, as well as the device length, *L*. We express the variables of velocity and stress (utilizing the Newtonian flow law) as well as the derivatives with respect to space and time in order to non-dimensionalize equation (S Eq. 1),

(S Eq 3) $$Re\left(\frac{\partial \vec{u}^*}{\partial t^*} + \vec{u}^* \cdot \nabla \vec{u}^*\right) = -\nabla^* \cdot \rho^* + \nabla^* \cdot \tau^*,$$

where non-dimensional variables and operators are marked with a superscribed asterisk (*). The non-dimensional group, the Reynolds number,

(S Eq 4) $$Re = \frac{\rho UH}{\mu}$$

occurring in front of the acceleration term on the left-hand side of equation (S Eq. 3) is a measure of the relative influence of inertia with respect to friction forces. Reynolds numbers well below unity indicate a viscous friction dominated (i.e., Stokes) flow. In the opposite case, Reynolds numbers exceeding a critical value of about $Re_{crit.} \approx 2000$ would be a clear indication of turbulence to occur. We basically have two distinctive flow regions in our model. The flow in the narrow pipes, with $H \approx 10^{-4}$ m and *U* in the range of 10^{-1} to 10^{-2} ms^{-1}, leading to Reynolds numbers in the range of unity. This is an indication that it is necessary to account for the acceleration terms on the left-hand side of equation (S Eq. 4), but also is a proof for the laminar nature of the flow, as $Re << Re_{crit.}$. This is important as otherwise the assumption of a parabolic inflow profile, as given in the form of equation (S Eq. 2) would not be possible.

Inserting the measures of the wider body of the devices with typical heights of $H \approx 10^{-4}$ m and typical velocities in the order of $U \approx 10^{-3}$ ms^{-1} (due to the increased cross-section), one obtains Reynolds numbers in the range of $Re = 10^{-1}$, which is a clear indication of Stokes (viscous friction dominated) flow – especially in the region of interest at the device center, where even lower velocities occur.

In order to derive the shear stress from the obtained solution of velocity field in the bulk as well as the walls of the device we evaluated the expression

(S Eq 5) $$\tau_{horiz.} = (\tau_{yz}^2 + \tau_{xz}^2)^{1/2},$$

as a measure of the exerted wall shear stress, $\tau_{horiz.}$, at the bottom of the devices. A characteristic wall shear rate,

(S Eq 6) $$\dot{\gamma}_{horiz.} = \frac{\tau_{horiz.}}{\upsilon} = \frac{(\tau_{yz}^2+\tau_{xz}^2)^{1/2}}{\mu},$$

was obtained by dividing the wall shear stress by the (constant) value of the viscosity, μ.

Representative examples of the results for the flow velocity, and shear rate over the bottom surface for the QCM and SPR flow channels at a height of 0.15 mm are shown in Figures S1-1 and S1-2. We see no qualitative difference in the flow behaviour at low and high grid resolution for either devices, and at either extreme height for the flow channels (not shown). We can thus be confident that our grid resolution is sufficient.

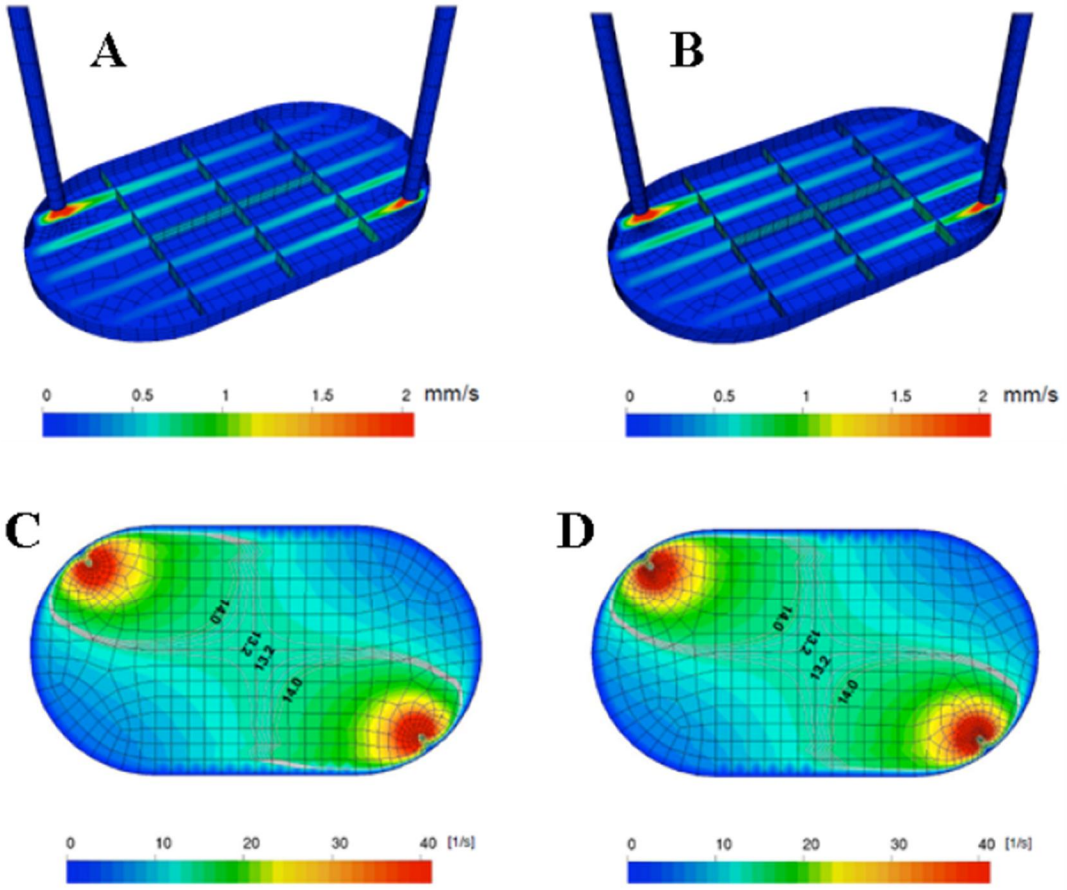

Figure S1-1. *Flow behaviour inside (A and B) and contour plot of the shear rate on the bottom surface of (C and D) an SPR flow cell with a height of 0.15 mm. Data is shown for A) and C) 10 µl/min low grid resolution, and B) and D) 10 µl/min high grid resolution. No change in behaviour with change in grid resolution can be seen over the relevant range of flow rates.*

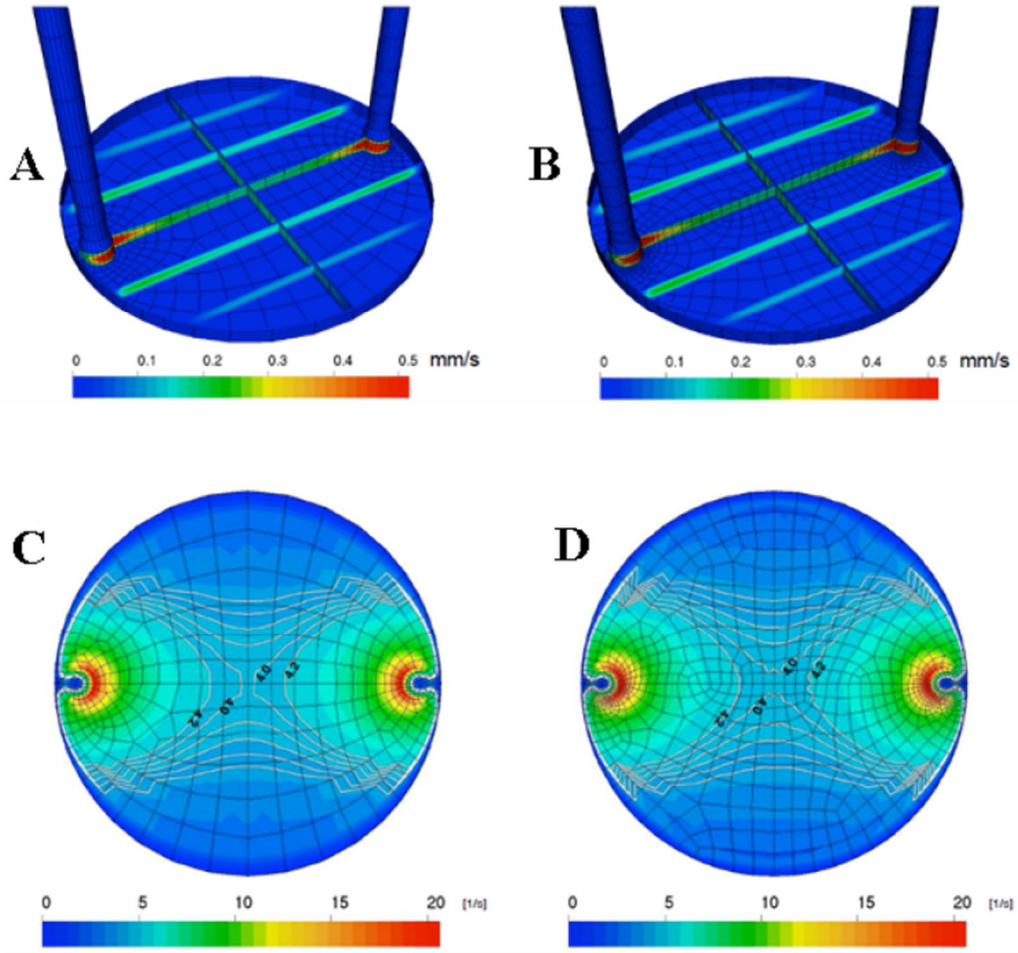

Figure S1-2. *Flow behaviour inside (A and B) and contour plot of the shear rate on the bottom surface of (C and D) a QCM flow cell with a height of 0.15 mm. Data is shown for A) and C) 10 µl/min low grid resolution, and B) and D) 10 µl/min high grid resolution. No change in behaviour with change in grid resolution can be seen over the relevant range of flow rates. Note the considerably lower flow rate (A and B) and shear rate (C and D) than for the case of the SPR due to the greater diameter/width of the QCM flow cell than the SPR flow cell.*

SII. Signal response for SPR and QCM flow channels

Fig. S2-1 shows the signal responses versus time for SPR with flow rates of 10 and 100 µl/min and QCM with flow rates of 73.3 and 733 µl/min for streptavidin binding to surface immobilized biotin. We did not notice any significant dissipation change during streptavidin adsorption in the QCM measurement when using a low flow rate and only a slight increase in dissipation to $\sim 0.5 \times 10^{-6}$ during the overshooting period seen in Fig. S2-1b for the higher flow rate. The overshooting effect seen in Fig. S2-1b and the slight increase in dissipation during this period for the higher flow rate in the QCM measurement is believed to originate from the higher transport rate of streptavidin to the surface leading to a second layer of loose unspecifically bound streptavidin on top of the

specifically bound streptavidin. The additional unspecifically bound streptavidin layer is kept in place by the pressure induced by the increased shear stress at high flow rates and then removed when flushing with buffer begins. This indicates that we approach a much shorter global (transport + kinetics) reaction time regime at such high flow rates.

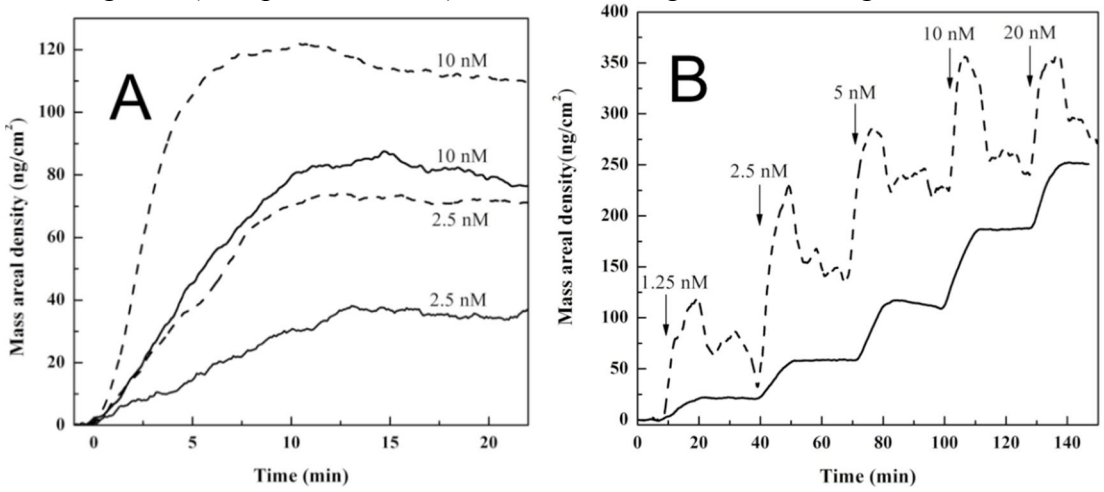

Figure S2-1. *Signal converted to mass areal density versus time for a) SPR and b) QCM during the interaction of surface immobilized biotin and different concentrations of injected streptavidin at different flow rates: a) 10 µl/min (solid line), 100 µl/min (dashed line), and b) 73.3 µl/min (solid line), 733 µl/min (dashed line). A constant interaction time of 10 minutes was allowed for the streptavidin-biotin interaction.*

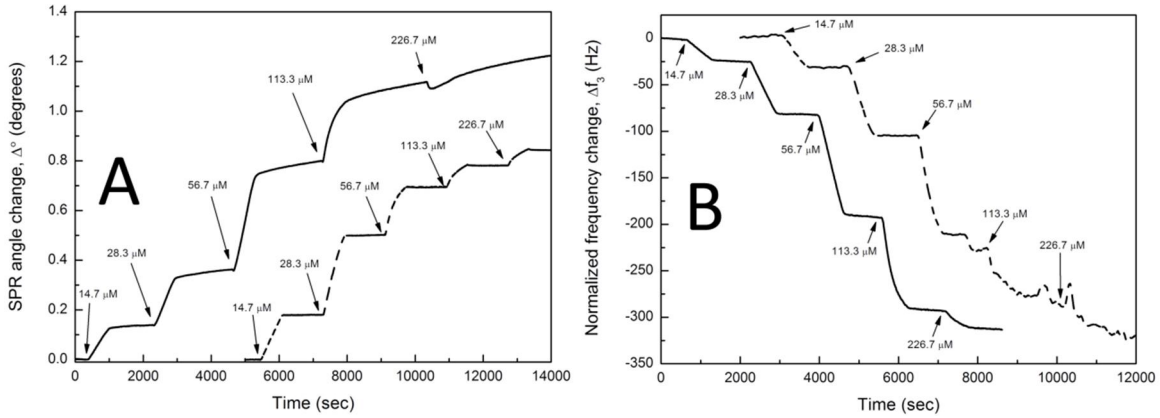

Figure S2-2. *Signal versus time for a) SPR and b) QCM during the interaction of a streptavidin functionalized sensor surface and different concentrations of injected liposome solutions at different flow rates: a) 10 µl/min (solid line), 100 µl/min (dashed line), and b) 73.3 µl/min (solid line), 733 µl/min (dashed line). A constant interaction time of 10 minutes was allowed for the streptavidin-liposome interaction. The high flow rate curves (dashed lines) have been shifted in time for clarity.*

The results in Fig. S2-2 show that the binding of liposomes is strongly mass transport controlled, due to the above discussed reasons, for the streptavidin-biotin interaction. The fact that the normalized overtones from QCM measurements do not superimpose and deviates much from each other (not shown) combined with a large dissipation change

(not shown) clearly proves that the liposomes bind to the streptavidin surface mainly as intact liposomes. This is in agreement with other studies where intact liposome layers are formed on oxidized gold surfaces (Reimhult et al., 1006; Serro et al., 2011).

SIII. Definition of shear stress and shear rate

Shear stress (SS)

Shear stress, τ, is a stress state in which deformation of a material is induced by a stress parallel to the surface of the material. In fluid mechanics, shear stress is generated from the motion of fluids. The SI unit of shear stress is pascal (Pa).

Shear rate (SR)

Shear rate, $\dot{\gamma} = \frac{du}{dy}$, is the rate at which a shear is applied. The unit of shear rate is the inverse of time, e.g. s^{-1}.

The relation between shear stress and shear rate is described as the following equation:

(S Eq 7) $\tau = \mu \frac{du}{dy}$

where μ is the viscosity of the fluid.

References

Reimhult, E., M. Zäch, F. Höök, and B. Kasemo. (2006). A multitechnique study of liposome adsorption on Au and lipid bilayer formation on SiO_2. *Langmuir*, 22, 3313-3319.

Serro, A.P., A. Carapeto, G. Paiva, J.P.S. Farinha, R. Colaço, and B. Saramago. (2012). Formation of an intact liposome layer adsorbed on oxidized gold confirmed by three complementary techniques: QCM-D, AFM and confocal fluorescence microscopy. *Surface and Interface Analysis*, 44 (4), 426-433.

Saad, Y. (1996) *Iterative methods for sparse linear systems (1st ed.)*; PWS: Boston, Section 10.3 and further.

8 CONCLUSIONS

The aims of this thesis were to utilize and integrate the non-labelled surface sensitive techniques, SPR and QCM, into platforms for pharmaceutical nanotechnology research by improving and optimizing the instruments, as well as developing the related methodologies. The main conclusions of the thesis are summarized:

1. The multi-Parametric SPR (MP-SPR) protype was successfully improved and optimized into a custom modified device which is featured with a real-time wide angular scan (40 to 78˚) covering both the air and the liquid phases. Two or more wavelengths are available when needed. A small dead volume (microliter level), a dual flow channel design and flexible (*in-situ* or pre-) functionalization approaches enabling user specific sensor chip coatings were utilized. These features enable the optimized MP-SPR device to be used both for studying the small molecular and biomacromolecular interactions, as well as for the characterization of ultrathin film. This was verified by carefully choosing measurement examples for the studies, including a series of small molecules (i.e. sucrose, ethylene glycol and ethanol), a model biomolecular interaction pair (streptavidin-biotin), and by characterizing ultrathin films (stearic acid LB films) in air or liquid. Especially, the methods developed in this work for simultaneous determination of both the refractive index and the thickness of the ultrathin films by using only an SPR instrument with two wavelengths and two media (air and liquid) enable the characterization of ultrathin films whenever needed. This makes the MP-SPR instrument a promising tool for building different kinds of platforms for pharmaceutical nanotechnology studies.

2. The one-instrument approach for accurately extracting multiple parameters of organic layers with a wide range of thickness (a few nm to hundreds of nm) was successfully developed. The ability to perform SPR measurements at multiple wavelengths allows both for the accurate characterization of ultrathin films, and the characterization of relatively thick organic layers in the micrometer range. A multiple wavelength SPR based analysis is shown to be an efficient approach for determining the ultrathin film properties in the range which is difficult to access by other methods. The applicability of the MP-SPR for measuring the film thickness and the optical properties using waveguide modes is also demonstrated. These results can be utilized in characterizing and building different detection platforms for sensor development, life sciences, drug development, as well as for obtaining fundamental information about the optical properties of different biological and organic systems.

3. The SPR and QCM flow channels were synchronized by hydrodynamic modeling to achieve consistent fluid flow conditions for the combined use of SPR and QCM. A scaling expression was acquired by computational fluid dynamics modeling (CFD). The synchronization with the scaling was verified by studying the specific interactions between a biomolecule and a liposome nanoparticle. The normalized responses and the apparent equilibrium constants for the synchronized flow rates between SPR and QCM devices coincide with each other confirming that the scaling approach based on hydrodynamic modeling is not only successful for rigid protein-ligand interactions, but also for more complex interactions involving the formation of visco-elastic layers, such as

nanoparticles. Additional information on how shear stress might influence the structure of the adsorbed protein and the liposome layers opens up new opportunities for building a better understanding of the kinetics of biomolecular interactions and the targeted drug delivery systems under controlled flow conditions. The results also highlight the importance of taking the hydrodynamic conditions into account when comparing the results from two- or several measuring techniques.

4. The interaction of targeted liposome nanoparticles with surface immobilized receptors can quantitatively be characterized by SPR and QCM devices with synchronized hydrodynamic conditions. The difference in the normalized SPR and QCM signals due to changes in the flow rate and shear stress further highlight the significance of the combined use of SPR and QCM for obtaining complementary information. The entrapped water/buffer in the bound liposome layer, which can be sensed by the QCM device, significantly influences the measured QCM signals and affinities. In contrast, the SPR is only sensitive to the bound liposomes and the measured SPR signals, as well as the affinities are independent of the entrapped water. SPR is, therefore, more suitable for kinetics and affinity characterization of specific targeted nanoparticle interactions, whereas QCM is not good for determining the kinetics and affinity, but for extracting additional information, such as the structural properties of the bound liposomes. The results obtained show that the binding of targeted liposomes is the flow rate and shear stress regulated. At high flow rate, more liposomes can be bound to the surface. However, the bound liposomes can encounter deformation and even rupture into lipid bilayers, which make the liposome layers more rigid. The combined use of the synchronized SPR and QCM devices form an effective platform with a high potential for the *in vitro* optimization of targeted liposome based formulations.

9 FUTURE PERSPECTIVES

Integration of non-labelled technique based systems and automation and high throughput screening (HTS). Several non-labelled detection techniques, e.g. SRU BIND, based on the waveguide-guide mode resonant filter and the CellKey based on the impedance, have utilized the automated analysis for HTS in drug discovery (Cunningham et al., 2004; Leung et al., 2005). SPR imaging also enables HTS with automatic analysis with SPR based systems, e.g. Biacore 4000. In this thesis, the combined use of the SPR and the QCM systems has been achieved by synchronizing the two separate SPR and QCM devices. The results obtained indicate the significance of the combined use of the devices for enabling an in-depth understanding of the behaviour of nanoparticle binding and interactions at the interfaces. However, an apparent disadvantage is that the efficiency of the data analysis is not high enough for HTS of drugs and targeted NP interactions. The same sample has to be measured by the two separate devices, and the monitored signals have to be manually analyzed to calculate the parameters. In the future, it would be beneficial to integrate both the SPR and the QCM devices into the same instrument for comprehensive analysis. Automation (both autosampler and autoanalysis) is desired to enable the immediate acquisition of the interaction parameters without additional manual analysis after a measurement. Such an integrated system would allow HTS and massive analysis of drug candidates and targeted NPs. Additionally, the HTS and the automated analysis based on the SPR for the characterization of thin films should be considered in order to achieve immediate extraction of the properties of the thin films.

Biomimetic model membranes. Simplified model membranes allow the studies of individual receptor interactions and functions. The molecular mechanisms behind the biological interactions can be obtained by simplified model membranes, which are primary suitable for optimization and screening drugs or drug targets. However, in this thesis, SAMs were used for nanoparticle interaction analysis. The structure and the properties of the SAMs are different from those of the cell membrane (lipid bilayer). In the future, biomimetic model membranes such as polymer cushioned lipid bilayers could be fabricated to prepare surfaces that closely resemble the cell membranes *in vivo*.

Cell based detection. Several non-labelled detection techniques have been developed and utilized for drug discovery, e.g. GPCR screening with HTS, by using cell monolayer based sensing (Fang, 2006; Fang et al., 2008; Scott & Peters, 2010). The response of the compounds or the targeted formulation *in vivo* could in the future be predicted with well-designed cell based non-labelled techniques. Furthermore, the relevant biochemical and the pharmacological mechanisms, which might not be clarified in an animal study, should be possible to be investigated at the cellular level by using a label-free automatic HTS analysis system. The real-time monitoring and the well-controlled physicochemical conditions in the cell based label-free techniques are foreseen to provide more accurate and quantitative results of cellular interactions of drugs and nanoparticles compared with traditional cell culture assays in well-plates. For example, the effect of the hydrodynamic conditions can already be studied with SPR and QCM, which is not possible with static cell cultures in well-plates.

Correlation to biological assays. The results from the label-free techniques should be compared and correlated with *in vitro* cell culture studies and *in vivo* animal tests in order to correctly predict the effects *in vivo*. The model membranes should be well-defined and standardized in the future to make this correlation reliable. At the same time, the effect of the components of blood *in vivo*, e.g. human serum albumin, should also be studied in depth.

References

Cunningham, B. T., Li, P., Schulz, S., Lin, B., Baird, C., Gerstenmaier, J., et al. (2004). Label-free assays on the BIND system. *J Biomol Screen, 9*(6), 481-490.

Fang, Y. (2006). Label-free cell-based assays with optical biosensors in drug discovery. *Assay Drug Dev Technol, 4*(5), 583-595.

Fang, Y., Frutos, A. G., & Verklereen, R. (2008). Label-free cell-based assays for GPCR screening. *Combinatorial chemistry & high throughput screening, 11*(5), 357-369.

Leung, G., Tang, H. R., McGuinness, R., Verdonk, E., Michelotti, J. M., & Liu, V. F. (2005). Cellular dielectric spectroscopy: a label-free technology for drug discovery. *Journal of the Association for Laboratory Automation, 10*(4), 258-269.

Scott, C. W., & Peters, M. F. (2010). Label-free whole-cell assays: expanding the scope of GPCR screening. *Drug Discovery Today, 15*(17-18), 704-716.